La investigación reportada en esta tesis es parte de los programas de investigación del CICESE (Centro de Investigación Científica y de Educación Superior de Ensenada, Baja California).

La investigación fue financiada por el SECIHTI (Secretaría de Ciencia, Humanidades, Tecnología e Innovación).

Centro de Investigación Científica y de Educación Superior de Ensenada, Baja California

Doctor of Science
in Nanosciences

Development and evaluation of hydrogels for the delivery of compounds with the potential to promote bone remodeling

A dissertation
submitted in partial satisfaction of the requirements for the degree
Doctor in Science

By:

Tonatzin Zertuche Arias

Ensenada, Baja California, México
2025

A Dissertation Presented by

Tonatzin Zertuche Arias

And approved by the following Committee

Dra. Ana Bertha Castro Ceseña
Thesis codirector

Dra. Patricia Juárez Camacho
Thesis codirector

Dra. Ana Guadalupe Rodríguez Hernández

Dra. Carolina Álvarez Delgado

Dr. Christopher John Hernandez

Dr. Néstor Emmanuel Díaz Martínez

Dr. Alejandro Huerta Saquero
Coordinator of Postgraduate in Nanosciences

Dra. Ana Denise Re Araujo
Director of Studies of Postgraduate

Resumen de la tesis que presenta **Tonatzin Zertuche Arias** como requisito parcial para la obtención del grado de Doctor en Ciencias en Nanociencias.

Desarrollo y evaluación de hidrogeles para la entrega de compuestos con el potencial de promover la remodelación ósea

Resumen aprobado por:

Dra. Ana Bertha Castro Ceseña
Codirectora de tesis

Dra. Patricia Juárez Camacho
Codirectora de tesis

La regeneración ósea es un proceso complejo que coordina la regulación de la inflamación, la angiogénesis y la remodelación de la matriz extracelular. Aunque los autoinjertos siguen siendo el estándar de oro en la reparación ósea por su compatibilidad biológica y potencial osteogénico, presentan limitaciones como la morbilidad del sitio donador, disponibilidad restringida e integración variable. Alternativas como los aloinjertos y los dispositivos de fijación también conllevan desafíos clínicos, entre ellos el riesgo de rechazo inmunológico, fibrosis y reabsorción ósea. Para abordar estas limitaciones, los hidrogeles inyectables basados en polímeros naturales han emergido como alternativas mínimamente invasivas capaces de adaptarse a defectos irregulares y funcionar simultáneamente como andamios estructurales y sistemas de liberación. En esta tesis se diseñaron hidrogeles compuestos por gelatina y quitosano metacrilados, entrecruzados mediante fotopolimerización, para la entrega de N-acetilcisteína (NAC) y del péptido pro-adrenomedulina (PAMP). Se formularon cuatro variantes: una sin compuestos bioactivos (GC), y otras funcionalizadas con NAC (GCN), PAMP (GCP) o ambos (GCNP). Los materiales se caracterizaron mediante FTIR, SEM, ensayos mecánicos, de hinchamiento, degradación enzimática y celular, y perfil de liberación. Además, se evaluó su efecto sobre la viabilidad y mineralización de células preosteoblásticas MC3T3-E1, así como su comportamiento en cultivo *ex vivo* de calvaria. Mediante FTIR se confirmó la metacrilación de los polímeros y su interacción con NAC, lo que se demostró al observar por SEM el aumento significativo en el tamaño de poro al incorporar NAC, de 24.49 ± 14.19 µm (GC) a 200.49 ± 80.42 µm (GCN). GCNP presentó mayor hinchamiento y degradación acelerada: en presencia de lisozima, la pérdida de masa a 14 días fue de 97.53 ± 4.23 %, y en cocultivo con macrófagos RAW 264.7 durante 7 días alcanzó el 87.14 ± 4.29 %. El perfil de liberación mostró un comportamiento bifásico en GCNP, con un 86.60 ± 6.00 % liberado a los 7 días. En cuanto a propiedades mecánicas, GCN alcanzó la mayor resistencia a la compresión (151.79 ± 44.81 kPa), mientras que GCNP exhibió el módulo de Young más alto (55.26 ± 5.79 kPa). A nivel biológico, la viabilidad celular se evaluó mediante MTT (*in vitro*) y Live/Dead Kit (*ex vivo*), observándose que GCNP promovió un efecto sinérgico al incrementar la actividad metabólica de células MC3T3-E1 a los 1,3 y 7 días, así como la proliferación celular en el tejido circundante del modelo *ex vivo* de defecto crítico de calvaria a los 14 días. La mineralización, determinada por tinción con rojo de Alizarin S, se duplicó *in vitro* respecto al control, y también fue evidente *ex vivo* mediante fluorescencia. Estos hallazgos demuestran que la incorporación combinada de NAC y PAMP no solo mejora la bioactividad del material, sino que también modula favorablemente su arquitectura, degradación y respuesta celular. En conjunto, los resultados confieren a los hidrogeles GCNP una funcionalidad dual como soporte temporal y como vehículo de liberación, favoreciendo la mineralización en las primeras etapas de la regeneración ósea, lo que sugiere su potencial aplicación biomédica en el tratamiento de defectos óseos complejos.

Palabras clave: Hidrogeles, regeneración ósea, N-acetilcisteína, péptido pro-adrenomedulina

Abstract of the thesis presented **by Tonatzin Zertuche Arias** as a partial requirement to obtain the Doctor of Science degree in Nanosciences.

Development and evaluation of hydrogels for the delivery of compounds with the potential to promote bone remodeling

Abstract approved by:

Dra. Ana Bertha Castro Ceseña
Thesis codirector

Dra. Patricia Juárez Camacho
Thesis codirector

Bone regeneration in non-load-bearing defects involves highly coordinated processes, including Bone regeneration is a complex process that coordinates inflammation regulation, angiogenesis, and extracellular matrix remodeling. Although autografts remain the gold standard in bone repair due to their biological compatibility and osteogenic potential, they present limitations such as donor site morbidity, restricted availability, and variable integration. Alternatives such as allografts and fixation devices also pose clinical challenges, including risks of immune rejection, fibrosis, and bone resorption. To address these limitations, injectable hydrogels based on natural polymers have emerged as minimally invasive alternatives capable of adapting to irregular defects and functioning simultaneously as structural scaffolds and delivery systems. In this thesis, hydrogels composed of methacrylated gelatin and methacrylated chitosan were developed and crosslinked via photopolymerization to deliver N-acetylcysteine (NAC) and the pro-adrenomedullin peptide (PAMP). Four formulations were prepared: one without bioactive compounds (GC) and three functionalized with NAC (GCN), PAMP (GCP), or both (GCNP). The materials were characterized by FTIR, SEM, mechanical testing, swelling behavior, enzymatic and cellular degradation, and release profiles. Their effect on the viability and mineralization of MC3T3-E1 preosteoblastic cells was also evaluated, along with their behavior in an *ex vivo* calvarial culture model. FTIR confirmed the methacrylation of the polymers and their interaction with NAC, which was supported by SEM analysis showing a significant increase in pore size upon NAC incorporation, from 24.49 ± 14.19 µm (GC) to 200.49 ± 80.42 µm (GCN). GCNP exhibited enhanced swelling and accelerated degradation: in the presence of lysozyme, mass loss after 14 days reached 97.53 ± 4.23 %, and in coculture with RAW 264.7 macrophages for 7 days it reached 87.14 ± 4.29 %. The release profile of GCNP showed biphasic behavior, with 86.60 ± 6.00 % released by day 7. Regarding mechanical properties, GCN exhibited the highest compressive strength (151.79 ± 44.81 kPa), whereas GCNP had the highest Young's modulus (55.26 ± 5.79 kPa). Biologically, cell viability was assessed using MTT (*in vitro*) and Live/Dead Kit (*ex vivo*). GCNP demonstrated a synergistic effect by enhancing the metabolic activity of MC3T3-E1 cells on days 1, 3, and 7, and by promoting cell proliferation in the surrounding tissue of the *ex vivo* critical-sized calvarial defect at day 14. Mineralization, determined by Alizarin Red S staining, doubled *in vitro* compared to the control and was also evident *ex vivo* by fluorescence. These findings demonstrate that the combined incorporation of NAC and PAMP not only improves the material's bioactivity but also favorably modulates its architecture, degradation, and cellular response. Altogether, the results confer GCNP hydrogels a dual functionality as temporary structural support and delivery vehicle, promoting mineralization in the early stages of bone regeneration, and suggesting their potential for biomedical application in the treatment of complex bone defects.

Keywords: Hydrogels, bone remodeling, N-acetylcystein, pro-adrenomedullin peptide

Dedication

Dedico este trabajo a las mujeres que me han acompañado a lo largo de la vida y a aquellas que han llegado para inspirarme y darme fuerza para seguir luchando cada día.

Mis abuelas no tuvieron la oportunidad de estudiar. Mi abuela materna, Bertha Rodríguez, creció en el rancho Tomás Urbina, Durango, donde solo existía escuela hasta tercer grado. Asistió tantas veces como le fue permitido, hasta que su edad la hizo "demasiado grande" para el salón. Terminó trabajando para mantener sola a mi mamá y a mis tíos, enfrentando un contexto de opresión para las mujeres y violencia laboral. Crecí escuchándola decir cuánto le gustaba la escuela y que, de haber tenido la oportunidad, le habría gustado ser política o abogada, porque disfrutaba debatir, hablar en público y defender sus ideas. Mi abuela paterna, Mercedes Gontes, vivió entre Cuernavaca y la Ciudad de México. A pesar de recibir una beca para estudiar danza en Bellas Artes, tuvo que dejar la escuela para cuidar a su familia y atender a sus hermanos, quienes sí pudieron estudiar y convertirse en ingenieros. Ella fue relegada al rol de ama de casa en un entorno de violencia. Hoy, siendo adulta, reconozco el privilegio de haber podido abrirme camino académico, gracias al ejemplo de estas mujeres fuertes y su acompañamiento, que me enseñaron que los derechos no se piden como favores, sino que se luchan.

A mi tía Vero la vi ir a la universidad y luego empezar como pasante en el CICESE. Tenía cinco años cuando soñé por primera vez con trabajar ahí. Durante mucho tiempo quise estudiar ciencias computacionales porque ella lo hizo. Cuando supe que ella haría una maestría, yo también quise hacerla, sin saber siquiera lo que significaba. A mis tías Meche, Paty y Ange que me enseñaron con su ejemplo de toda la vida, a valerme por mí misma y defender las injusticias de un sistema patriarcal. Ellas me motivaron e impulsaron siempre a ser la científica que ya era desde niña.

A la maestra Yólotl, que me ha enseñado a ser gentil con mi autismo y me ha acompañado de cerca en estos cuatro años, en medio de crisis, incertidumbre y sanación. Gracias por abrirme los ojos a la necesidad de una investigación científica interseccional, descolonizadora y con perspectiva de género.

A mis amigas del posgrado: Claudia, Miryam, Brenda, Salma y Selene. Gracias por demostrarme que, aun en una sociedad que hoy presume inclusión, pero sin una práctica real, podemos abrirnos paso como mujeres neurodivergentes. Somos sistemáticamente oprimidas para ser y actuar conforme a la norma, sin exagerar ni llamar la atención, y seguir el ritmo apresurado que no se detiene si aprendemos

diferente. En medio de una lucha diaria por integrarnos y ser comprendidas siendo nosotras mismas hemos llegado hasta aquí. Gracias a ustedes he tenido el valor de alzar la voz, a nombrar las violencias del sistema y a pelear por un espacio digno. A veces quisiera andar por el mundo con la seguridad de un hombre blanco, privilegiado, y colonizador, de esos que aún se atreven a decir que las mujeres deberíamos dejar de "jugar al doctorado" y volver a la cocina mientras ocupan cargos de poder sin mayor esfuerzo. Pero entonces pienso en mis amigas racializadas, con discapacidades invisibles, y reafirmo que es histórico ser una mujer "histérica".

A las amigas que hacemos en el camino y se volvieron familia, siempre han creído en mí aun cuando yo no lo hacía, impulsándome a seguir mi sueño y mi camino ninja. A Diana, Magaly, Michelle y Nadllely. Gracias por nunca dejarme sola. Hoy después de tantos años y distancia, me siento acompañada desde sus espacios y me enseñan a resistir con ternura.

A mi mamá Mónica, que no tengo palabras para la mezcla indescriptible de emociones desbordadas de años de aprendizaje, resiliencia, y amor.

A mi mamá Angélica, por quererme, cuidarme y creer en mí.

A mi mentora la Dra. Ana Bertha que siempre sentí su apoyo, aunque yo ya no tuviera fuerzas para seguir, fue la motivación que encontraba en los momentos más oscuros para continuar un día a la vez.

A Maité que dijo que quería ser bióloga molecular y a la niña en el centro de salud y dijo que quería ser genetista. Pensar en que más niñas en camino a la ciencia me dan la fuerza para mantener estos espacios seguros, así como hubo grandes mujeres científicas que lucharon porque hoy pudiéramos estar aquí.

Este trabajo es para mis abuelas, mis tías, mis madres, mis hermanas y mis amigas que han sido mis maestras. Reafirmo que no daré un paso atrás, deseo que encuentren un camino un poco mejor que el que hoy nosotras enfrentamos.

A la Chiquis que hace salir cada día el sol y me ayuda a sobrevivir en este mundo hostil.

Acknowledgements

This work was supported by CICESE (Grant No. 685105) to Dr. Patricia Juárez-Camacho and CICESE (Grant No. 685112) to Dr. Ana Bertha Castro-Ceseña. Additional support was provided by SECIHTI through a scholarship granted to Tonatzin Zertuche-Arias (Grant No. 746304).

I would like to express my deepest gratitude to my advisors. I thank Dr. Ana Bertha Castro-Ceseña for her constant guidance and support throughout my doctoral journey, and Dr. Patricia Juárez-Camacho for enabling my participation in scientific conferences and research stays, always securing the necessary funding to support these opportunities.

I also acknowledge the valuable contributions of my thesis committee, whose feedback has been essential at every stage of this project.

My sincere thanks go to Dr. Manuel Alatorre-Meda for his invaluable assistance with mechanical testing, for sharing his time and expertise in data analysis, and for his continuous support throughout the publication process.

I am also grateful to Dr. Ignacio Rivero for his assistance with scanning electron microscopy.

I extend my sincere appreciation to Dr. Alfredo Martínez for hosting me at CIBIR in La Rioja during the angiogenesis training and for the *in vivo* experiment performed under his guidance. His contribution to this work, particularly through the introduction of PAMP, has been invaluable.

I also thank Dr. Ricardo Pérez Pastén for welcoming me into his lab at IPN, generously sharing his knowledge, and helping me strengthen techniques not acquired during my time at CICESE. As he once said, I was able to use his lab as “a springboard for my academic future.”

Special thanks to Lucía Michelle Chávez-López, Daniel Reyes-López, and Vanessa Rodríguez-Magaña from Universidad Xochicalco for their support in the experimental procedures, and to Marco A. Uriostegui for his help in fine-tuning the images used in the paper and this thesis.

Table of contents

Page

Abstract (Spanish)....ii

Abstract (English)....iii

Dedication....iv

Acknowledgements....vi

List of figures....ix

List of tables....xv

Chapter 1. Introduction....1

1.1 Background....3

1.1.1 Bone Remodeling and Regeneration....3

1.1.2 Challenges in Bone Tissue Engineering....7

1.1.3 Hydrogels for Non-Load-Bearing Bone Defects....10

1.1.4 Biological Rationale for NAC and PAMP....16

1.2 Justification....20

1.3 Hypothesis....21

1.4 Objectives....22

1.4.1 Main objective....22

1.4.2 Specific objectives....22

Chapter 2. Methodology....23

2.1 Synthesis of hydrogels....23

2.2 Physicochemical characterization of hydrogels....24

2.2.1 Fourier-Transform Infrared Spectroscopy (FTIR)....24

2.2.2 Swelling Behavior....24

2.2.3 Degradation Kinetics....25

2.2.4 Release profile....26

2.3 Morphological Characterization 27
2.3.1 Pore Size Analysis 27
2.4 Mechanical Properties 27
2.5 Biocompatibility 28
2.5.1 *In Vitro* Viability 28
2.5.2 *Ex vivo* Viability 28
2.6 Bioactivity 29
2.6.1 *In Vitro* Mineralization 29
2.6.2 *Ex Vivo* Calvaria Mineralization 29
2.7 Statistical Analysis 30
Chapter 3. Results and Discussion 31
3.1 Physicochemical Characterization of Hydrogels 31
3.1.1 Chemical Composition Characterization of the Hydrogels 31
3.1.2 Swelling Capacity of the Hydrogels 32
3.1.3 Degradation Profile of the Hydrogels 34
3.1.4 Cumulative Release of NAC and PAMP 36
3.2 Morphological Characterization of the Hydrogels 38
3.3 Mechanical Properties of the Hydrogels 41
3.4 Biocompatibility of Hydrogels 43
3.5 Osteogenic Potential: *In Vitro* and *Ex Vivo* Mineralization 46
3.6 Integrated Discussion of Findings 49
Chapter 4. Conclusions 53
Bibliography 55
Appendix 64

List of figures

Figure Page

1. Age-standardized incidence (A) and prevalence (B) of fractures per anatomical site, by GBD region and sex, 2019. GBD=Global Burden of Diseases, Injuries, and Risk Factors Study. Modified from (A.-M. Wu et al., 2021) 2

2. Hierarchical structure and bone formation mechanisms. (a) Bone exhibits a hierarchical structure from the nanoscale (collagen molecules and hydroxyapatite nanocrystals) to the macroscale (osteons and compact/spongy bone). (b) Intramembranous ossification involves direct differentiation of mesenchymal stem cells (MSCs) into osteoblasts under the influence of transcription factors such as Runx2 and osterix, followed by osteoid formation, matrix mineralization, and trabecular bone development. (c) Endochondral ossification begins with MSC condensation and differentiation into chondrocytes via Sox9 signaling, followed by chondrocyte hypertrophy, matrix degradation, and vascular invasion leading to the formation of primary and secondary ossification centers. From (Jasmine and Krishnamoorthy, 2022).....4

3. Schematic representation of the fracture healing process. Temporal and cellular progression of bone regeneration following a fracture, including hematoma formation (days 0–5), soft callus development (days 5–10), fibrous tissue formation (days 10–16), hard callus formation (days 16–21), and bone remodeling (days 21–35). The diagram highlights the dynamic interplay between immune cells (monocytes, macrophages, T and B cells), progenitor cells, chondrocytes, osteoblasts, osteoclasts, and osteocytes. The phases are classified into anabolic and catabolic processes, overlapping with inflammatory, endochondral, and remodeling stages. From (Einhorn and Gerstenfeld, 2015), ...5

4. Illustration of the essential components for bone tissue regeneration. Osteogenesis is initiated by mesenchymal stem cells capable of differentiating into bone-forming cells. Osteoconduction refers to the use of a porous, vascularized scaffold that guides and supports new tissue growth. Osteoinduction involves bioactive signaling molecules, such as BMPs, that stimulate stem cells to commit to the osteoblastic lineage. The coordinated action of these three elements is required to successfully regenerate bone tissue. From (Sordi et al., 2021). .7

5. Overview of commonly used biomaterials for bone tissue engineering. Metallic materials such as titanium and magnesium alloys offer mechanical strength, while their functionalization with ions or nanoparticles can enhance bioactivity. Ceramic materials, including hydroxyapatite and β-tricalcium phosphate, mimic the mineral phase of bone and promote osteointegration. Polymers are classified as non-biodegradable (e.g., polyethylene, PEEK) or biodegradable (e.g., PLA, PCL, chitosan) and are selected based on the required degradation rate and mechanical behavior. From (Riester et al., 2021). 8

6. Biomedical applications of hydrogels in skeletal tissue repair. Hydrogels have emerged as versatile materials for treating a variety of bone-related conditions, including bone defects, fractures, cartilage damage, and osteosarcoma (OS). Their tunable physical and biological properties allow for targeted delivery, tissue support, and integration in musculoskeletal environments. From (X. Liu et al., 2022). 13

7. Schematic representation of in situ photopolymerization of an injectable hydrogel for bone tissue repair. The image illustrates the injection of a viscous precursor solution into a bone defect site, followed by in situ light irradiation (e.g., with a dental curing lamp) to induce hydrogel crosslinking. This approach enables minimally invasive application and conformal adaptation to irregular bone geometries. From (Chichiricco et al., 2023). 14

8. Antioxidant role of NAC in bone homeostasis and periodontitis-associated oxidative stress. In healthy conditions, the Nrf2/Keap1 pathway maintains bone remodeling balance by regulating antioxidant responses. Under periodontitis, elevated reactive oxygen species (ROS) trigger chronic inflammation, suppress osteoblast function, and enhance osteoclast activity, disrupting bone homeostasis. N-acetylcysteine (NAC) and NAC-derived carbonized polymer dots (NAC-CPDs) activate Nrf2 signaling and mitigate oxidative damage, restoring the osteoblast–osteoclast balance. From (X. Liu et al., 2023). 15

9. Schematic representation of the cellular and vascular mechanisms involved in bone regeneration. At the bone defect site, type H vessels—characterized by the expression of Endomucin and CD31—modulate osteogenesis by promoting the recruitment and differentiation of osteoprogenitor cells into osteoblasts and eventually osteocytes. Mesenchymal stem cells (MSCs) and endothelial cells secrete VEGF, a key pro-angiogenic factor, which stimulates angiogenesis and enhances bone tissue regeneration. From (Jang and Yoon, 2024). 16

10. Biological effects and regulatory pathways of N-acetylcysteine (NAC) in bone tissue engineering. (A) NAC enhances glutathione synthesis and reduces disulfide bonds, contributing to oxidative stress mitigation. (B) In seeding cells, including stem and precursor cells, NAC exerts concentration-dependent effects: physiological antioxidation improves proliferation and osteogenesis via PI3K/AKT, WNT/β-catenin, KEAP1/NRF2, and HIF1α/p53 pathways; in contrast, excessive antioxidant levels can induce reductive stress. (C) In innate immune cells, NAC modulates macrophage polarization (favoring M2 over M1) and inhibits osteoclast differentiation by suppressing NF-κB and MAPK signaling pathways. From (Zheng et al., 2024). 17

11. Schematic representation of the processing of preproadrenomedullin (prepro-AM) and the resulting mature peptides PAMP and adrenomedullin. The prepro-AM precursor contains a signal peptide (residues 1–20), followed by the sequences encoding PAMP (residues 21–41) and adrenomedullin (residues 94–146). Upon proteolytic cleavage and amidation, two biologically active peptides are generated: PAMP (20 amino acids) and AM (52 amino acids). From (Kita et al., 2022)..... 18

12. Mechanism of action of ADM2 in bone regeneration through osteogenic–angiogenic coupling. ADM2 promotes bone regeneration in distraction osteogenesis by enhancing osteogenesis and angiogenesis. The signaling cascade involves activation of p65, AKT, and β-catenin pathways in bone marrow-derived mesenchymal stem cells (BMSCs), leading to upregulation of both osteogenic and pro-angiogenic genes. ADM2 also stimulates endothelial cells (ECs) to secrete angiogenic factors, contributing to a feedback loop that couples vascular and bone tissue regeneration. From (F. Wang et al., 2021). 19

13. FTIR spectra of individual components and GC hydrogel formulations containing NAC and/or PAMP. Fourier-transform infrared (FTIR) spectra of the base biopolymers—gelatin (Gel), methacrylated gelatin (GelMA), chitosan (Ch), and methacrylated chitosan (ChMA)—as well as

the base hydrogel (GC), and the formulations loaded with N-acetylcysteine (GCN), pro-adrenomedullin peptide (GCP), or both bioactive compounds (GCNP). Characteristic absorption bands corresponding to functional group vibrations were identified, including hydroxyl and amine stretching (ν(-OH)/ν(-NH)), alkyl groups (ν(-CH)), thiol groups (ν(-SH)), carbonyl (ν(C=O)), amide bending (δ(N-H)), and C–N stretching (ν(C–N)). 32

14. Swelling kinetics of GC hydrogels functionalized with NAC and/or PAMP. Swelling ratio (Wt/W0) of gelatin methacrylate and chitosan methacrylate (GC) hydrogels, either unloaded (GC) or functionalized with N-acetylcysteine (GCN), pro-adrenomedullin (GCP), or both compounds (GCNP), over 24 hours of incubation in PBS 1X at 37 °C. The inset graph highlights an extended analysis of the first 3 hours, where a significant difference in initial water absorption is observed in the GCNP and GCP formulations compared to GC and GCN. The GCNP group exhibited the highest swelling capacity, remaining significantly above the other formulations throughout the period. Data are presented as mean ± SEM (n = 3). Statistical differences were analyzed using two-way ANOVA followed by Dunett's post hoc test. At 1 h, GCNP was significantly higher than GC (***, $p < 0.001$) and GCN (***, $p < 0.001$). At 3 h, GCP was significantly higher than GC (*, $p = 0.01$), and GCNP remained higher than GC (***, $p < 0.001$) until equilibrium was reached after 24 h. 33

15. Evaluation of degradation of GC hydrogels functionalized with NAC and/or PAMP *in vitro*. (A) Remaining mass percentage of methacrylated gelatin and chitosan (GC) hydrogels, unloaded (GC) or functionalized with NAC (GCN) and both compounds (GCNP), after *in vitro* incubation in PBS 1X with type II collagenase at 37 °C for 21 days. (B) Degradation in the presence of RAW 264.7 cells cultured in indirect contact with the hydrogels under physiological conditions. GCNP hydrogels degraded significantly faster than GC, with both GCN and GCNP nearly fully degraded by day 14, while the GC group retained over 50% of its original mass. Data are presented as mean ± SEM (n = 3). Statistical differences were analyzed using two-way ANOVA followed by Tukey's post hoc test. Significant differences were found at day 7 between GC and GCNP (*, $p = 0.04$), at day 14 GC vs. GCNP (**, $p = 0.001$), and at day 21 GC vs. GCN (*, $p = 0.02$). 35

16. Representative images of *in vivo* degradation following subcutaneous implantation of hydrogels in C57BL/6 mice, retrieved after 11 days. H&E-stained histological images show increased cellular infiltration and hydrogel disintegration in GCN and especially GCNP, compared to GC, which retained its structure. GCP induced the formation of a fibrotic capsule encapsulating the hydrogel. Scale bar: 200 µm. 36

17. Cumulative release of bioactive compounds from GC hydrogels. Release profiles of N-acetylcysteine (GCN), pro-adrenomedullin (GCP), and their combination (GCNP) from methacrylated gelatin and chitosan (GC) hydrogels over 14 days in PBS 1X at 37 °C. The inset graph highlights the initial 12 hours, showing that GCN and GCNP exhibit significantly higher early release compared to GCP. GCNP achieved a balanced release profile, combining an initial burst with sustained delivery. Data are presented as mean ± SEM (n = 3). Statistical differences were analyzed using two-way ANOVA followed by Tukey's post hoc test. At 6 h, NAC hydrogels released significantly more than GCP (*, $p = 0.03$), which increased at 9 h (**, $p = 0.002$). By 12 h, GCN remained significantly higher than GCP (***, $p < 0.001$). 37

18. Schematic and morphological characterization of dual-crosslinked hydrogels with different bioactive treatments. Representative diagrams (top), SEM micrographs (middle), and pore size distribution (bottom) of methacrylated gelatin and chitosan (GC) hydrogels, with or without

N-acetylcysteine (GCN), pro-adrenomedullin (GCP), or both (GCNP). SEM images show morphological differences associated with compound incorporation, with more porous structure observed in NAC-containing hydrogels. Pore size quantification revealed a higher frequency of large pores in GCN and GCNP compared to GC and GCP. Scale bar: 100 µm. ... 39

19. Pore size comparison in GC hydrogels functionalized with NAC and/or PAMP. Pore size measured in GC, GCN, GCP, and GCNP hydrogels from SEM images. A significant increase in pore size was observed in NAC-containing groups (GCN and GCNP) compared to GC, suggesting a NAC-induced effect on hydrogel porous architecture. Data are presented as mean ± SD, with *n* corresponding to the number of pores measured per group (GC: 30 pores, GCN: 42 pores, GCP: 34 pores, GCNP: 32 pores). Statistical differences were analyzed using one-way ANOVA followed by Tukey's post hoc test. Results showed that GCN and GCNP were significantly higher than GC (***, $p < 0.001$), and GCN also significantly higher than GCP (***, $p < 0.001$)..... 40

20. Mechanical properties of GC hydrogels functionalized with NAC and/or PAMP. (A) Representative stress–strain curves obtained from uniaxial compression of methacrylated gelatin and chitosan (GC) hydrogels, either unloaded (GC), or functionalized with N-acetylcysteine (GCN), pro-adrenomedullin (GCP), or both (GCNP). (B) Young's modulus (E) from the initial linear region. (C) Compressive strength at failure (σF). (D) Toughness (U_T), measured as energy absorbed before mechanical failure. GCN exhibited the highest σF and U_T, while GCNP showed the highest E value, suggesting distinct mechanical advantages depending on the formulation. Data are presented as mean ± SEM (n = 3). Statistical differences were analyzed using one-way ANOVA followed by Tukey's post hoc test. No significant differences were detected among groups in E ($p > 0.05$). In σF, GCN was significantly higher than GC, *GCP*, and GCNP (***, $p < 0.001$). GCNP was also significantly higher than GC and GCP (***, $p < 0.001$). In U_T, GCN was significantly higher than GC (**, $p = 0.002$), GCP (**, $p = 0.001$), and GCNP (**, $p = 0.009$). 41

21. Viability of MC3T3-E1 cells in indirect culture with functionalized GC hydrogels. MTT assay results for preosteoblastic MC3T3-E1 cells cultured on the bottom of transwell systems exposed to unloaded (GC), NAC-loaded (GCN), PAMP-loaded (GCP), or dual-loaded (GCNP) methacrylated gelatin and chitosan hydrogels for 1, 3, and 5 days. The GCNP group showed significantly higher cell viability at all time points, exceeding the monolayer control group without hydrogel. In contrast, GC and GCN exhibited variable responses, while GCP showed a more stable but moderate effect. Data are presented as mean ± SD (n = 3). Statistical analysis was performed using two-way ANOVA with Dunnett's post hoc test, comparing all hydrogel conditions to the control at each time point. GCNP showed the most pronounced enhancement in viability, particularly in days 3 and 5. Exact *p* values are shown above bars and correspond to the following significance levels: $p < 0.05$ (*), $p < 0.01$ (**), and $p < 0.001$ (***). 43

22. Evaluation of cell viability in *ex vivo* calvarial cultures with GC hydrogels. Fluorescence images after 14 days of *ex vivo* culture of mouse calvariae with unloaded (GC), NAC-loaded (GCN), PAMP-loaded (GCP), or dual-loaded (GCNP) hydrogels using the Live/Dead® assay. Calcein AM (green) indicates live cells, EthD-1 (red) marks membrane-compromised cells, and natural bone autofluorescence appears in blue. The GCNP condition showed higher densities of viable cells at the periphery of the defect compared to other groups, suggesting a more favorable environment for cell survival. Scale bar: 100 µm..... 45

23. Osteogenic activity induced by GC hydrogels. Representative images of extracellular matrix mineralization by bone marrow-derived cells indirectly cultured with unloaded (GC), NAC-loaded (GCN), PAMP-loaded (GCP), or dual-loaded (GCNP) hydrogels. ARS staining (top row) marks calcium deposits (red), and ALP staining (bottom row) indicates enzymatic activity (purple). A positive osteogenic control and a negative control (growth medium only) were included. GCNP hydrogels showed staining intensity comparable to the positive control, suggesting a synergistic effect of NAC and PAMP in promoting osteoblastic differentiation. Scale bar: 400 µm. 46

24. Quantification of mineralized area induced by GC hydrogels. ARS quantification of bone marrow-derived cells cultured with unloaded (GC), NAC-loaded (GCN), PAMP-loaded (GCP), or dual-loaded (GCNP) hydrogels, compared to positive and negative controls. GCNP induced the largest mineralized area, with statistically significant differences compared to all other groups (***, $p < 0.001$), highlighting the synergistic action of NAC and PAMP on osteogenic differentiation. In addition, GC also differed significantly from the positive control and GCP (**, $p = 0.003$). Data are presented as mean ± SD ($n = 3$). Statistical differences were analyzed using one-way ANOVA followed by Tukey's post hoc test. 47

25. *Ex vivo* mineralization in a critical-sized calvarial defect model. Brightfield (top) and fluorescence (bottom) images of mouse calvariae cultured *ex vivo* for 14 days in osteogenic medium with GC, GCN, or GCNP hydrogels placed within the defect. Alizarin Red S staining reveals red fluorescent signal indicating calcium deposition. GCNP showed the most intense and widespread signal, indicating superior mineralized matrix formation. Osteogenic control also showed strong mineralization, while the negative control and GC displayed minimal signals. Scale bar: 100 µm. 48

26. Alkaline phosphatase (ALP) activity in *ex vivo* calvarial cultures. Representative images of mouse calvariae after 14 days of *ex vivo* culture in direct contact with unloaded (GC), NAC-loaded (GCN), PAMP-loaded (GCP), or dual-loaded (GCNP) hydrogels. Tissues were stained to detect ALP, an early marker of osteoblastic differentiation. Controls included growth medium (negative) and osteogenic medium (positive). GCNP displayed the most intense ALP staining, similar to the positive control, indicating strong osteogenic activation in the bone tissue in contact with this hydrogel. Scale bar: 200 µm. 49

27. Antioxidant activity of ALA and NAC evaluated using the DPPH method. The percentage of antioxidant activity of α-lipoic acid (ALA) in both its emulsified and ethanol-dissolved forms, and soluble NAC, was assessed at concentrations ranging from 0.1 to 20 mM using the DPPH radical scavenging assay. NAC demonstrated significantly higher antioxidant activity at all concentrations tested, reaching up to 75% inhibition. In contrast, ALA showed very limited activity in both formulations, remaining below 10% in all cases, which would hinder its detection in release studies. 64

28. Viability of L929 fibroblasts exposed to soluble NAC. MTT assay results after 24 hours of treatment with soluble NAC at concentrations ranging from 0.1 to 20 mM. Cell viability was measured by absorbance at 570 nm. A significant increase in viability was observed at 0.1 mM NAC, while no cytotoxic effect was detected at higher concentrations. 65

29. Antioxidant activity released from GC hydrogels with different NAC concentrations. Antioxidant release profiles were assessed using the DPPH assay for hydrogels composed of 4% or 7% gelatin methacrylate (GelMA) and 1% or 3% chitosan methacrylate (ChMA),

incubated in 1X PBS at 37 °C for up to 240 minutes. Control formulations without NAC (G7C1 and G4C3) were compared to those loaded with either 2 mM or 20 mM NAC. A rapid release was observed during the first 60 minutes, especially for the G7C1 20 mM and G4C3 20 mM groups, followed by a gradual decrease in antioxidant activity. Formulations without NAC showed minimal activity throughout the test..... 67

30. NAC release quantification. (A) NAC standard curve used to quantify NAC release. (B) NAC release profile from GelMA 4%–ChMA 3% hydrogels over 48 hours. (C) Glycine standard curve used to determine the cumulative release of NAC and PAMP from the hydrogels. Data are presented as mean ± standard deviation (n = 3). 68

31. Mechanical characterization of GC hydrogels loaded with 20 mM NAC. (A) Stress–strain curves from uniaxial compression tests for hydrogels composed of 4% or 7% gelatin methacrylate (GelMA) and 3% or 1% chitosan methacrylate (ChMA), corresponding to G4C3 and G7C1, respectively, both loaded with 20 mM N-acetylcysteine (NAC). (B) Young's modulus (E), calculated from the linear region of the stress–strain curves. (C) Toughness (UT), determined as the area under the curve up to the point of failure. G4C3 hydrogels displayed greater mechanical strength and stiffness than G7C1, likely due to a higher crosslinking density resulting from the increased ChMA content. 69

32. . Mechanical characterization of GC hydrogels. Compression stress-strain curves obtained from texture analysis (n=3). Each dataset corresponds to (A, E, I) GC, (B, F, J) GCN, (C, G, K) GCP, and (D, H, L) GCNP..... 70

33. Hemolysis percentages of G4C3 and G7C1 hydrogels at 0, 2, and 20 mM NAC concentrations. All values are below 5%, demonstrating hemocompatibility (n=3). 71

34. Blood clotting assay of G4C3 and G7C1 hydrogels. Lower absorbance indicates higher clotting efficiency (n=3)..... 72

35. Cell viability of RAW 264.7 cells after 24 h exposure to GC hydrogels loaded with 20 mM NAC (G4C3 and G7C1) assessed by Live/dead assay. Data are shown as mean ± SD, normalized to monolayer control..... 73

36. Live/dead assay of RAW 264.7 cells exposed to GC hydrogels loaded with 20 mM NAC (G4C3 and G7C1). Images show phase contrast (left), calcein-AM (middle), and ethidium homodimer-1 (right) fluorescence. Scale bar = 100 µm. 74

37. Viability of HMEC cultured for 24 and 48 h in the presence of hydrogel formulations placed in Transwell inserts. Viability was measured by MTT assay and normalized to the untreated monolayer control. Data are presented as mean ± SD (n=3). Asterisks indicate statistical significance between groups (*p<0.05, **p<0.01, ***p<0.001).* 75

38. Viability of aortic rings cultured within hydrogel matrices after 11 days. Bright-field (top row) and calcein-AM fluorescence (bottom row) images show the interaction between the aortic tissue and the hydrogel. GCNP hydrogels exhibited more diffuse green fluorescence, suggesting enhanced viability and potential tissue integration compared to other groups. Scale bars: 100 µm. 76

List of tables

Table Page

1. Comparative characteristics of biopolymers, metals, and bioceramics used in bone tissue engineering.....9

2. Summary of gelatin and chistosan hydrogel systems for bone applications..... 11

3. Comparative performance of GCNP versus reported hydrogel systems for bone regeneration 52

4. GelMA and ChMA combinations evaluated for the preparation of injectable hydrogels. 66

Chapter 1. Introduction

Bone tissue possesses an inherent ability to regenerate after injury. However, in large or complex defects—such as those caused by trauma, tumor resection, congenital malformations, or chronic inflammation—this regenerative capacity is often insufficient (Marsell and Einhorn, 2011). These situations present a major clinical challenge, particularly in anatomically demanding regions like the craniofacial skeleton, where structural, functional, and aesthetic outcomes are critical (Figure 1). According to the Lancet Commission on Global Surgery, an estimated 5 billion people worldwide lack access to safe surgical care, and the burden of musculoskeletal trauma remains a leading contributor to disability-adjusted life years (DALYs) globally, especially in low- and middle-income countries (Wu, 2021).

Traditional bone repair techniques include the use of autografts and allografts. While autografts remain the gold standard due to their biological compatibility and osteogenic potential, they are limited by donor site morbidity, limited availability, and variable integration (Fillingham and Jacobs, 2016). Allografts, on the other hand, may lead to immune rejection or incomplete remodeling. Moreover, fixation devices such as metal plates and screws—common in maxillofacial surgeries—can provoke complications, including stress shielding, infection, and implant failure due to poor vascularization or fibrotic encapsulation (Wang and Yeung, 2017).

Current clinical challenges are compounded by demographic and epidemiological trends. With the global population aging and the prevalence of chronic conditions increasing, bone repair is becoming even more complex. In older adults, bone healing is slower and more susceptible to complications such as delayed union or non-union (Wu, 2021). Additionally, patients with comorbidities like diabetes or osteoporosis often exhibit impaired osteogenesis and vascularization, which limit the effectiveness of conventional interventions (Saul and Khosla, 2022).

In addition to surgical limitations, certain patient conditions complicate treatment. Elderly patients, those with chronic illnesses, or individuals with multiple fractures often cannot undergo invasive procedures. Non-operable fractures, such as costal fractures, may also require alternative strategies due to anatomical constraints or patient fragility (Saul and Khosla, 2022; Wu et al., 2021).

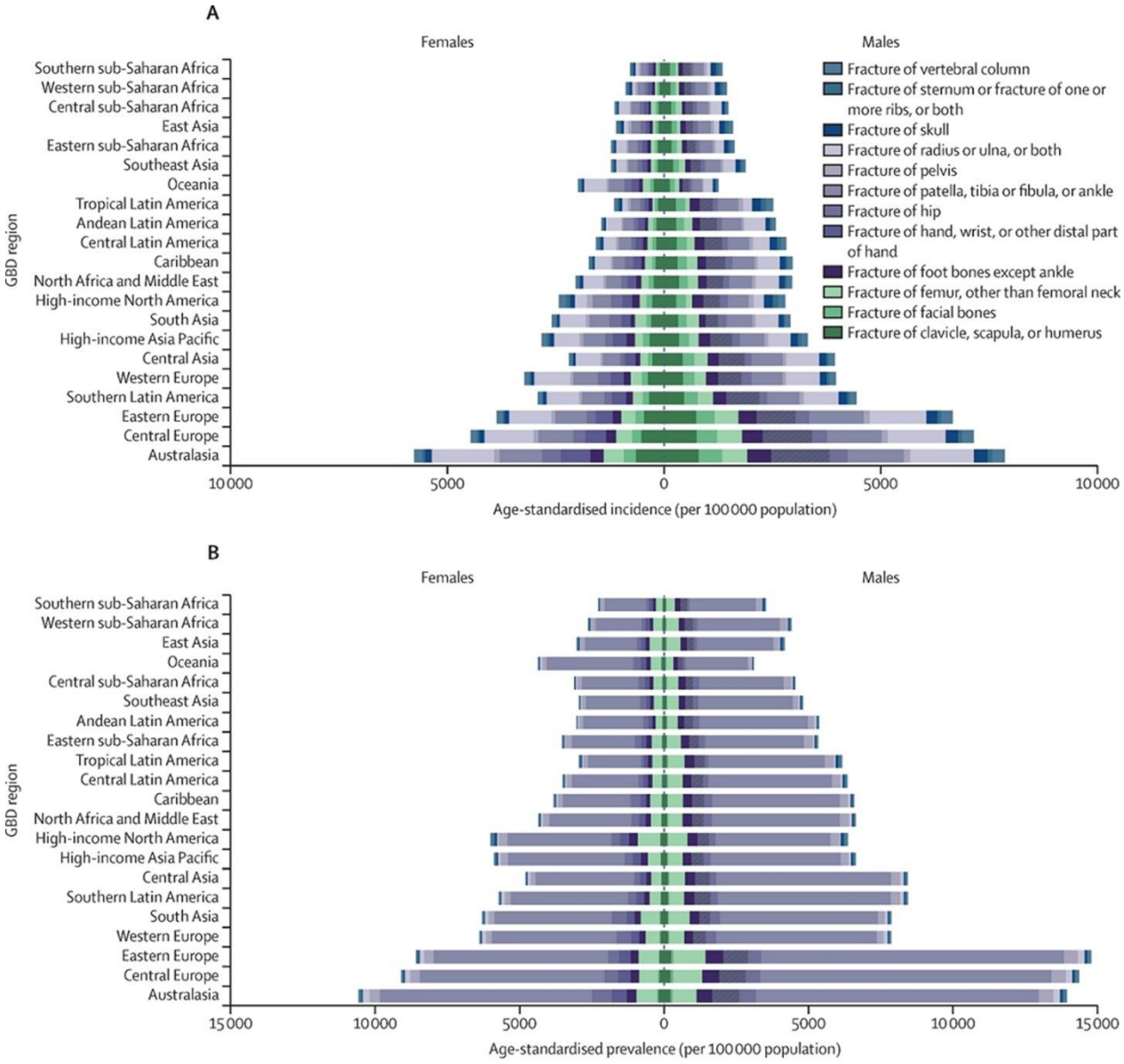

Figure 1. Age-standardized incidence (A) and prevalence (B) of fractures per anatomical site, by GBD region and sex, 2019. GBD=Global Burden of Diseases, Injuries, and Risk Factors Study. Modified from (A.-M. Wu et al., 2021)

In this context, biomaterials—especially injectable hydrogels—have emerged as promising tools for bone tissue regeneration. These materials offer several advantages: they can be administered through minimally invasive techniques, conform to irregular defect geometries, and serve as carriers for bioactive compounds (Mathew et al., 2018; Tu et al., 2019). Among natural polymers, gelatin and chitosan are widely studied for their biocompatibility, biodegradability, and functional similarity to native extracellular matrix. When chemically modified (e.g., methacrylation), they can form photo-crosslinkable hydrogels with tunable mechanical and degradation properties.

Despite these advances, most current injectable hydrogels lack the biological signals and structural support required for full bone regeneration. Poor vascularization, oxidative stress, and limited cell recruitment remain unresolved issues that hinder successful outcomes. For this reason, incorporating functional molecules that address these biological limitations is a growing area of interest (Jabbari, 2019; Riester et al., 2021; Sordi et al., 2021).

The present study explores the use of injectable methacrylated gelatin-chitosan hydrogels loaded with N-acetylcysteine (NAC), an antioxidant known to improve osteoblast survival and matrix mineralization, and pro-adrenomedullin peptide (PAMP), a novel peptide with potential pro-angiogenic and cytoprotective properties. These compounds aim to enhance both the osteogenic and vascular response within the damaged tissue. The purpose of this work was to evaluate whether injectable GC-based hydrogels containing NAC and PAMP can support bone regeneration by promoting biocompatibility, controlled degradation, and osteoinductive potential in both *in vitro* and *ex vivo* models.

1.1 Background

1.1.1 Bone Remodeling and Regeneration

Bone is a metabolically active tissue that undergoes continuous remodeling throughout life to preserve structural integrity and calcium-phosphate homeostasis. At the core of this process lies the ability of bone to mineralize its extracellular matrix, a fundamental step that grants the tissue its mechanical strength. Mineralization begins with the deposition of type I collagen and non-collagenous proteins such as osteocalcin and osteopontin by osteoblasts, which together provide a scaffold for hydroxyapatite (HA) crystal nucleation. These crystals are composed primarily of calcium and phosphate ions, and their organized deposition within collagen fibrils gives rise to the stiffness and durability of bone. The enzyme alkaline phosphatase (ALP), secreted by active osteoblasts, increases local phosphate concentrations by hydrolyzing phosphate-containing compounds, thereby promoting the formation and growth of HA crystals (Lin et al., 2020; Saul et al., 2022). In this context, calcium is not only a major component of the mineral phase but also a key indicator of matrix mineralization, and its accumulation is commonly used to quantify osteogenic differentiation and biomaterial performance *in vitro*.

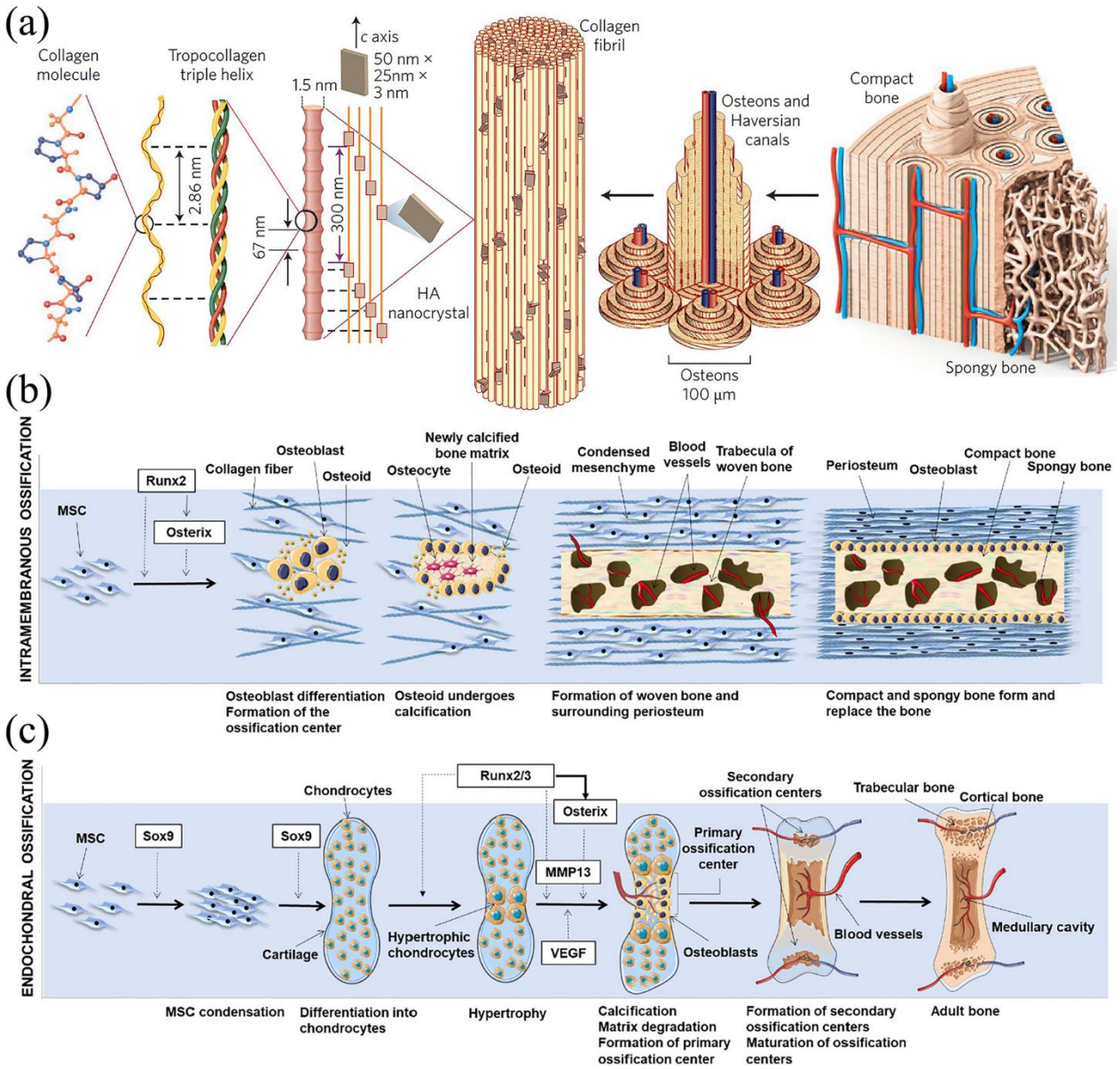

Figure 2. Hierarchical structure and bone formation mechanisms. (a) Bone exhibits a hierarchical structure from the nanoscale (collagen molecules and hydroxyapatite nanocrystals) to the macroscale (osteons and compact/spongy bone). (b) Intramembranous ossification involves direct differentiation of mesenchymal stem cells (MSCs) into osteoblasts under the influence of transcription factors such as Runx2 and osterix, followed by osteoid formation, matrix mineralization, and trabecular bone development. (c) Endochondral ossification begins with MSC condensation and differentiation into chondrocytes via Sox9 signaling, followed by chondrocyte hypertrophy, matrix degradation, and vascular invasion leading to the formation of primary and secondary ossification centers. From (Jasmine and Krishnamoorthy, 2022).

This hierarchical organization of mineralized bone is reflected in its structure—from the molecular arrangement of collagen and HA nanocrystals to the formation of osteons in compact bone and trabeculae in spongy bone. During development, this complexity arises through two distinct but complementary pathways: intramembranous and endochondral ossification. In the former, mesenchymal stem cells

(MSCs) differentiate directly into osteoblasts under the regulation of transcription factors such as Runx2 and Osterix, initiating bone formation without a cartilage intermediate. In contrast, endochondral ossification involves a cartilage template that is gradually replaced by mineralized bone, through a tightly regulated sequence that includes chondrocyte hypertrophy, matrix degradation, vascular invasion, and osteoblast recruitment. Together, these pathways give rise to the structurally and functionally integrated architecture of adult bone (Figure 2).

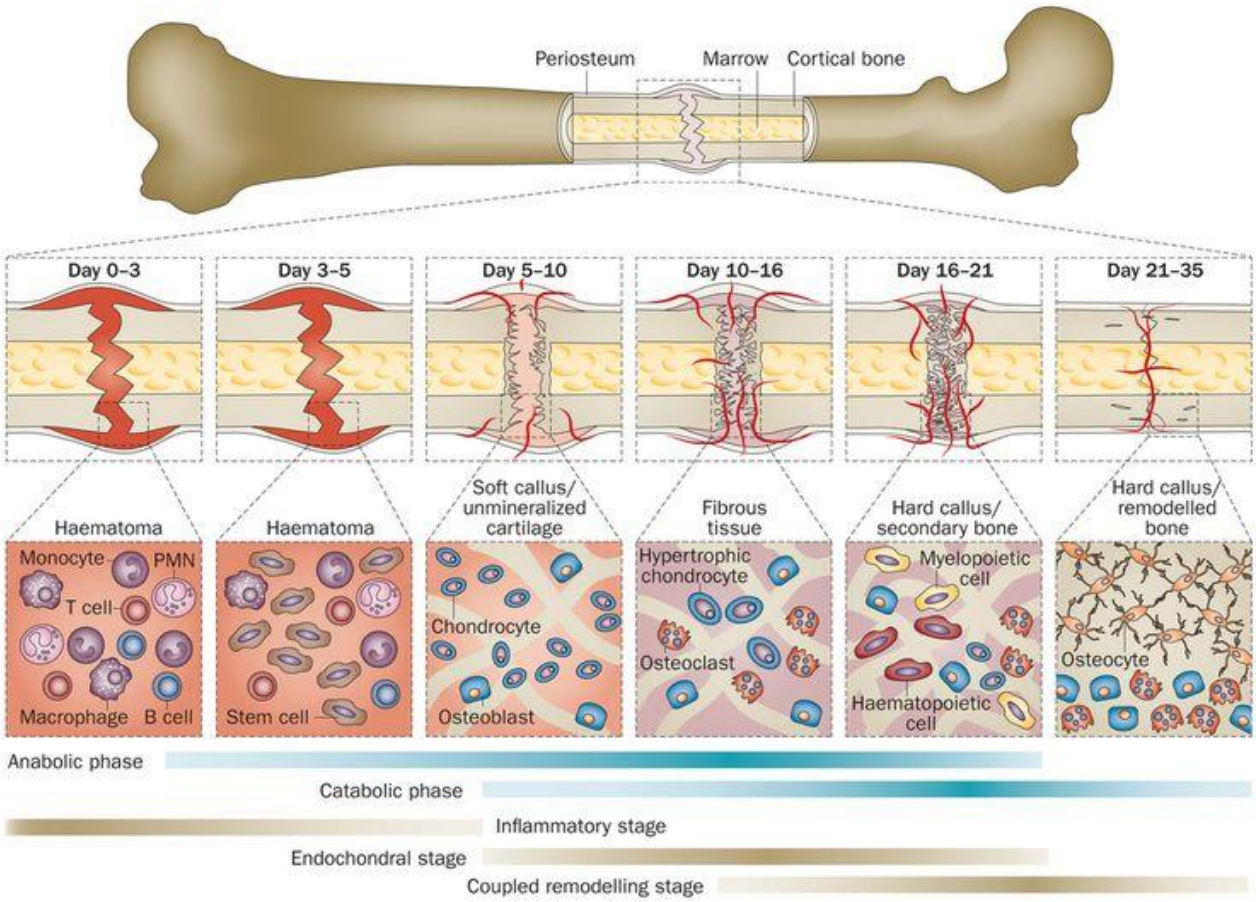

Figure 3. Schematic representation of the fracture healing process. Temporal and cellular progression of bone regeneration following a fracture, including hematoma formation (days 0–5), soft callus development (days 5–10), fibrous tissue formation (days 10–16), hard callus formation (days 16–21), and bone remodeling (days 21–35). The diagram highlights the dynamic interplay between immune cells (monocytes, macrophages, T and B cells), progenitor cells, chondrocytes, osteoblasts, osteoclasts, and osteocytes. The phases are classified into anabolic and catabolic processes, overlapping with inflammatory, endochondral, and remodeling stages. From (Einhorn and Gerstenfeld, 2015),

Once bone has formed, remodeling is continuously activated in response to various physiological and mechanical stimuli. These include signals from aged or microdamaged bone, altered mechanical loading,

hormonal regulation, and fluctuations in systemic calcium and phosphate levels. The process begins with the activation of osteoclast precursors and their differentiation into multinucleated osteoclasts, which degrade mineralized tissue through acidification and the release of proteolytic enzymes. A reversal phase follows, during which mononuclear cells—often macrophage-like—prepare the resorbed surface for new matrix deposition by osteoblasts derived from MSCs (Florencio-Silva et al., 2015; Ruggieri et al., 2021). Once embedded in the mineralized matrix, osteoblasts become osteocytes, which function as mechanosensory cells and modulate remodeling via signaling pathways such as Wnt/β-catenin and the regulation of sclerostin (Bonewald, 2011; Robling et al., 2006).

Bone regeneration recapitulates aspects of the remodeling cycle but occurs in response to injury or pathological conditions. It follows a temporally orchestrated process: (i) inflammation, (ii) soft callus formation, (iii) hard callus formation (mineralization), and (iv) remodeling (Figure 3). This process depends on coordinated angiogenesis, MSC recruitment, and the release of pro-regenerative cytokines and growth factors, including VEGF, BMPs, and TGF-β (Einhorn & Gerstenfeld, 2014; Majidinia et al., 2018). Vascular invasion is critical during the transition from soft to hard callus, as blood vessels supply oxygen, nutrients, and systemic progenitor cells necessary for osteogenesis (Ruggieri et al., 2021). Moreover, endochondral ossification during fracture healing illustrates how cartilage templates are replaced by mineralized bone, guided by tightly regulated gene expression and ECM remodeling (Hutchings et al., 2020).

The extracellular matrix itself plays an active role in bone biology, not only by providing structural support, but also by modulating signaling pathways and influencing cellular behavior. Its composition evolves throughout regeneration, transitioning from a collagen-rich provisional matrix to a mineralized scaffold laden with hydroxyapatite (X. Lin et al., 2020). The dynamic remodeling of the ECM allows for mechanotransduction, which is essential for adapting bone architecture to mechanical loads and ensuring long-term functionality (Fuchs et al., 2009).

Nonetheless, the regenerative capacity of bone can be impaired under conditions such as osteoporosis, diabetes, advanced age, or large critical-size defects, where angiogenesis, progenitor recruitment, and matrix deposition are insufficient (Saul and Khosla, 2022). In these cases, biomaterials have been developed to restore bone homeostasis by supporting osteoconduction, osteoinduction, and osteogenesis (Figure 4). Osteoconductive materials provide a 3D scaffold that facilitates cell adhesion and migration. Osteoinductive biomaterials actively promote the recruitment and differentiation of progenitor cells into osteoblasts, often by incorporating signaling molecules. Osteogenesis, on the other hand, refers to the intrinsic capacity of cells within the scaffold to generate new bone (Lin et al., 2020).

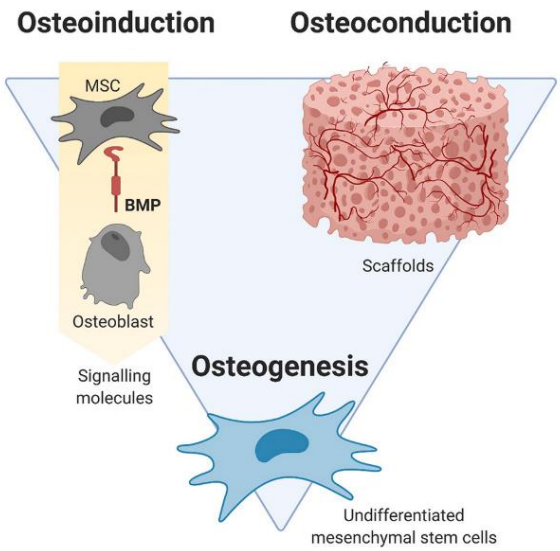

Figure 4. Illustration of the essential components for bone tissue regeneration. Osteogenesis is initiated by mesenchymal stem cells capable of differentiating into bone-forming cells. Osteoconduction refers to the use of a porous, vascularized scaffold that guides and supports new tissue growth. Osteoinduction involves bioactive signaling molecules, such as BMPs, that stimulate stem cells to commit to the osteoblastic lineage. The coordinated action of these three elements is required to successfully regenerate bone tissue. From (Sordi et al., 2021).

These three biological processes must be integrated into the design of biomaterials for bone tissue engineering. Materials must not only support structural regeneration but also recreate a microenvironment conducive to vascularization, matrix synthesis, and mineralization (Ruggieri et al., 2021).

1.1.2 Challenges in Bone Tissue Engineering

Although a wide range of biomaterials has been developed for bone tissue engineering (Figure 5)—including biopolymers, metals, and bioceramics—each class presents distinct trade-offs that must be carefully considered depending on the clinical application (Table 1) (Dec et al., 2023). Metals provide excellent mechanical strength and durability but are susceptible to corrosion and lack biodegradability (Shayesteh Moghaddam et al., 2016). Bioceramics, meanwhile, offer excellent chemical stability and bioactivity and closely resemble the mineral phase of bone, yet they tend to be brittle and dense, limiting their use in load-bearing applications (Barry Carter and Grant Norton, 2007). Biopolymers are generally biocompatible and easy to process but are often thermally unstable and mechanically weak (Kashirina et al., 2019).

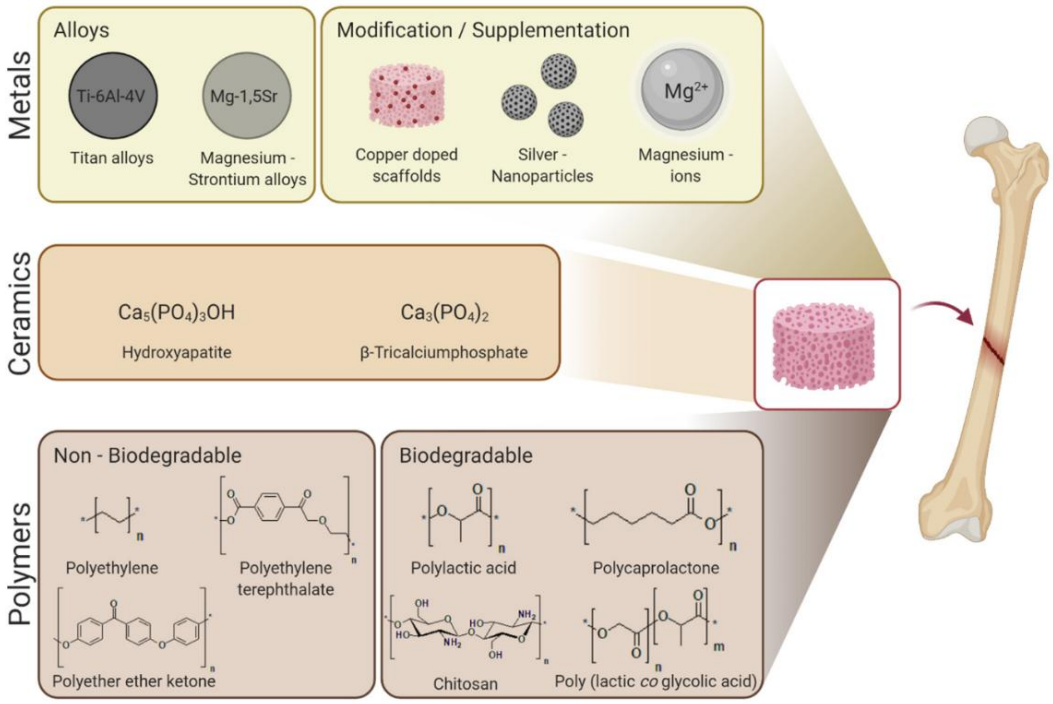

Figure 5. Overview of commonly used biomaterials for bone tissue engineering. Metallic materials such as titanium and magnesium alloys offer mechanical strength, while their functionalization with ions or nanoparticles can enhance bioactivity. Ceramic materials, including hydroxyapatite and β-tricalcium phosphate, mimic the mineral phase of bone and promote osteointegration. Polymers are classified as non-biodegradable (e.g., polyethylene, PEEK) or biodegradable (e.g., PLA, PCL, chitosan) and are selected based on the required degradation rate and mechanical behavior. From (Riester et al., 2021).

Despite significant advances, several critical challenges remain in the design and clinical translation of biomaterials for bone regeneration:

1. Poor vascularization: One of the main limitations in bone healing, especially in large or critical-sized defects, is insufficient blood vessel formation. Inadequate vascularization leads to hypoxia, nutrient deprivation, and impaired cellular activity, delaying or preventing proper regeneration. Biomaterials must promote angiogenesis to sustain cell viability and integration (Anada et al., 2019; Jang and Yoon, 2024).

2. Oxidative stress: Reactive oxygen species (ROS), which are elevated after trauma or during chronic inflammation, can damage proteins, lipids, and nucleic acids, leading to osteoblast dysfunction and impaired matrix mineralization. Incorporating antioxidant functionality into biomaterials may mitigate oxidative damage and improve healing outcomes (X. Li et al., 2021; Meng et al., 2022; Sun et al., 2023; Tao et al., 2020).

3. Chronic inflammation: While an initial inflammatory response is necessary for healing, prolonged or dysregulated inflammation can be detrimental, leading to fibrosis, delayed bone formation, or implant failure. Biomaterials must exhibit immunomodulatory properties to favor a pro-regenerative environment (Mountziaris and Mikos, 2008; Zeugolis et al., 2019).

4. Limited integration with host tissue: Poor cellular recruitment and lack of osteoconductive or osteoinductive signals can limit the integration and stability of implanted materials. Designing scaffolds with surface cues or bioactive agents can enhance cell attachment, proliferation, and differentiation (Barros et al., 2019; Cota Quintero et al., 2025; W. Wang and Yeung, 2017).

5. Mechanical mismatch and inadequate degradation rates: Hydrogels and other scaffolds must provide sufficient mechanical support during healing while degrading in synchrony with tissue formation. Mismatched degradation can either impede regeneration or result in premature scaffold failure (Chaudhuri et al., 2015; Mndlovu et al., 2024; Vert, 2009).

6. Irregular defect geometries: In clinical scenarios such as craniofacial or non-load-bearing defects, irregular geometries demand materials that are moldable or injectable. Injectable systems offer minimally invasive delivery and defect-conforming properties, which facilitate clinical application (Ghandforoushan et al., 2023; Lavanya et al., 2020; M. Liu et al., 2017).

Table 1. Comparative characteristics of biopolymers, metals, and bioceramics used in bone tissue engineering

	Biopolymers	**Metals**	**Bioceramics**
Type of connections	Covalent or van der Walls	Metallic	Ionic/covalent
Chemical stability	Weak	Good	Very good
Electrical conductivity	Very low	High	Very low
Thermal conductivity	Very low	High	Low
Characteristics and advantages	Degradable, similar density to soft tissue, and easy to process	High hardness and strength	Non-conductive and biologically inert; optimally imitate the properties of bone
Mechanical strength	Very high strength and plasticity (easy to shape and process)	Resistance to stretching	Brittle and fragile
Main disadvantages	Thermally unstable and low strength	Wear and corrosion	High density and brittleness
Biomedical applications	Soft tissue implants, drug delivery systems, and tissue engineering	Orthopaedic and dental implants	Tissue engineering

7. Material limitations and trade-offs: As summarized by Riester et al. (2021), different classes of biomaterials—such as biopolymers, metals, and bioceramics—exhibit distinct advantages and limitations. Biopolymers are biocompatible and processable but often thermally unstable; metals provide high mechanical strength but suffer from corrosion; and bioceramics offer excellent bioactivity but tend to be brittle. The choice of material must therefore be guided by the specific application and site of implantation.

These challenges define the functional requirements for next-generation biomaterials in bone tissue engineering. An ideal scaffold should support angiogenesis, counteract oxidative and inflammatory stress, promote cellular recruitment and differentiation, and adapt to the physical and mechanical demands of the defect site.

1.1.3 Hydrogels for Non-Load-Bearing Bone Defects

Hydrogels based on natural polymers have emerged as promising scaffolds for bone tissue engineering, particularly for non-load-bearing defects—such as craniofacial injuries, rib fractures, or critical-sized defects—where mechanical demands are lower and the scaffold is expected to degrade as new tissue forms (Figure 6). Injectable hydrogels have gained considerable attention as promising biomaterials for treating non-load-bearing bone defects. These systems offer several advantages: they can conform to irregular geometries and limited accessibility, be administered through minimally invasive techniques, and serve as carriers for bioactive agents that may support tissue repair (Chichiricco et al., 2023; Cota Quintero et al., 2025).

Among the most studied biomaterials for such applications are gelatin and chitosan (Table 2), both of which are derived from natural sources and exhibit desirable properties including biocompatibility, biodegradability, and structural similarity to the native extracellular matrix (L. Zhao et al., 2023). Gelatin methacrylate (GelMA) provides a matrix-like environment enriched with cell adhesion RGD motifs, while chitosan contributes antimicrobial and osteoconductive properties, particularly when chemically modified (Saraiva et al., 2015; L. Zhao et al., 2023). Methacrylation of both polymers enables photo-crosslinking, allowing precise control over the network's physical and degradative behavior (Yue et al., 2016; Zanon et al., 2022). A wide variety of gelatin–chitosan-based hydrogels have been explored for bone repair, many incorporating additional materials or compounds to enhance mechanical strength, biological activity, or controlled degradation. For example, some studies have introduced inorganic fillers such as nanoclays (Andrade et al., 2023) or hydroxyapatite (Osi et al., 2021), while others combine gelatin-chitosan matrices

with synthetic polymers such as PEGDA (Y. Wang et al., 2020). Photocrosslinking remains a common strategy to stabilize the structure, and several systems have demonstrated injectability, bioadhesion, or compatibility with 3D printing (Céspedes-Valenzuela et al., 2021; Osi et al., 2021).

Table 2. Summary of gelatin and chistosan hydrogel systems for bone applications

Hydrogel Composition	Application	Results	Comparable Features	Reference
Chitosan + oxidized dextran + Abaloparatide	Bone regeneration in rat calvarial defect	Precise release kinetics, enhanced bone volume and mineral density	Injectable, dual-functional (osteogenic peptide delivery), tunable delivery	(Ning et al., 2019)
1% GelMA + 6% laponite (nanoclay)	*In vitro* osteogenic induction	Injectable rheological behavior, >80% cell viability, promoted osteogenic differentiation	Injectable, osteoinductive, improved mechanical/thermal stability	(Andrade et al., 2023)
GelMA + octacalcium phosphate (OCP)	3D bioprinted vascularized bone-mimetic constructs	Promoted osteogenesis and formation of capillary-like structures	Injectable, osteoinductive, supports vascular network formation	(Anada et al., 2019)
Chitosan-GelMA with thermo/photo dual-crosslinking	Contraction fabrication with controlled shrinking	Thermo- and light-triggered gelation; precise shape control during contraction	Dual-responsive, hybrid crosslinking, shape-controlled injectable	(Luo et al., 2020)
2% ChMA + 20% GelMA + I-2959 photoinitiator	Tissue regeneration	Pore size average 30 μm, suitable degradation and swelling properties, cytocompatible	Photocrosslinkable, natural polymers, injectable potential, biocompatible	(Saraiva et al., 2015)
Methacrylated chitosan–gelatin hydrogel	3D printable scaffold for tissue engineering	Good printability, dual thermo/photo crosslinking, strong mechanical properties, cytocompatible	Injectable potential, dual crosslinking, 3D-printable	(Osi et al., 2021)
GelMA hydrogel loaded with adrenomedullin	Dental pulp regeneration (*in vitro* and *in vivo*)	Promoted cell viability, angiogenesis, and pulp-like tissue regeneration	Injectable, angiogenic peptide delivery, natural polymer matrix	(Y. Zhao et al., 2025)

Continuation of Table 2. Summary of gelatin and chistosan hydrogel systems for bone applications

Hydrogel Composition	Application	Results	Comparable Features	Reference
Cyclodextrin-functionalized gelatin	Injectable MSC and drug delivery for bone regeneration	Injectable, self-healing, supports MSC viability and sustained icaritin delivery	Injectable, drug and cell carrier, dynamic crosslinking network	(Feng et al., 2016)
ChMA + Graphene oxide	Bone tissue adhesion and repair	Injectable, strong adhesion to wet bone, reinforced and biocompatible	Photocrosslinkable, injectable, bioadhesive, mechanically enhanced	(Céspedes-Valenzuela et al., 2021)
Graded layered GelMA–ChMA, UV-crosslinked	Osteochondral defect repair (*in vitro* and *in vivo*)	Zone-specific chondrogenic and osteogenic support, structural integration	Photocrosslinkable, layered natural polymers, zonal regeneration	(Han et al., 2015)
GelMA + PEGDA + nano-hydroxyapatite	Bone tissue engineering	Enhanced osteogenic differentiation and mechanical strength	Composite matrix, osteoconductive, not purely natural, injectable potential	(Y. Wang et al., 2020)
GelMA–HAMA hydrogel loaded with osteogenic growth peptide (OGP)	Bone regeneration (*in vitro* and *in vivo*)	Sustained OGP release, enhanced osteogenic differentiation and mineralization	Injectable, photocrosslinkable, peptide-functionalized hydrogel	(B. Liu et al., 2023)
GelMA + ChMA (UV-crosslinked) coating on PPENK	*In vitro* osteoblastic differentiation and apatite formation	Induced apatite nucleation and improved MC3T3-E1 cell differentiation	Photocrosslinkable, mineralizing, bioactive natural polymers	(Y. Li et al., 2021)
GelMA + ChMA, chemically crosslinked	*In vitro* cytocompatibility and swelling/degradation tests	Tunable degradation, biocompatible with fibroblasts, stable mechanical behavior	Natural polymers, chemically crosslinked, degradable, biocompatible	(Joshi et al., 2021)

Some hydrogels aim to promote osteogenesis via the delivery of osteogenic peptides like abaloparatide or OGP, while others have incorporated growth factors or ceramic additives to stimulate mineralization (Alizadeh-Osgouei et al., 2019; B. Liu et al., 2023; Ning et al., 2019). A smaller subset has targeted angiogenesis through growth factors like adrenomedullin or the design of layered or vascularized

constructs (Anada et al., 2019; Y. Zhao et al., 2025). There are also innovative approaches that use host–guest chemistry to achieve dynamic and cell-infiltratable networks (Feng et al., 2016, 2019a). These functionalized designs represent major advances in the field. However, many still focus on a single biological mechanism, and challenges remain in engineering injectable materials that can address multiple regenerative barriers simultaneously—such as oxidative stress, poor vascularization, and synchronization of degradation with new tissue formation (Gilarska et al., 2021; Shi et al., 2023; Xue et al., 2025). Consequently, there is growing interest in dual-functional hydrogel systems that combine structural support with complementary bioactive cues.

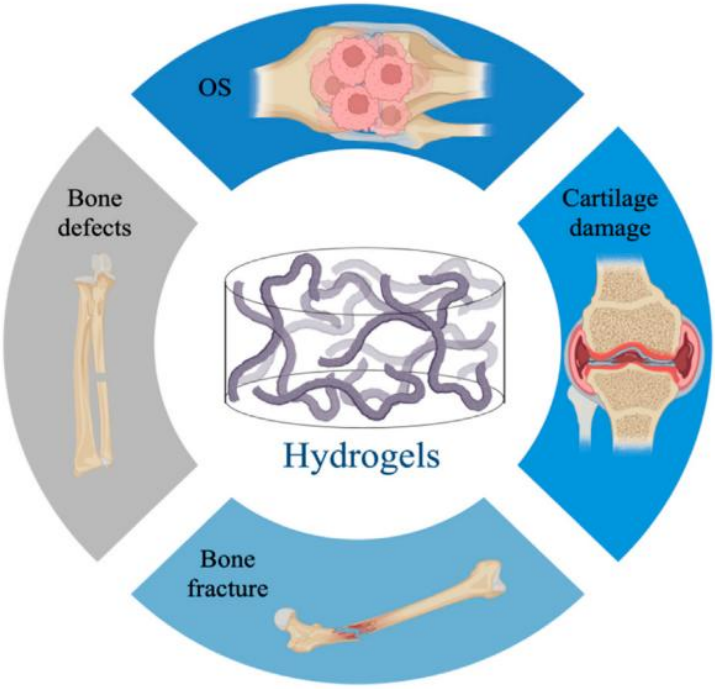

Figure 6. Biomedical applications of hydrogels in skeletal tissue repair. Hydrogels have emerged as versatile materials for treating a variety of bone-related conditions, including bone defects, fractures, cartilage damage, and osteosarcoma (OS). Their tunable physical and biological properties allow for targeted delivery, tissue support, and integration in musculoskeletal environments. From (X. Liu et al., 2022).

Hydrogel systems have been evaluated for their ability to support cranial defect repair. For example, a photo-crosslinkable interpenetrating network (IPN) hydrogel composed of silanized hydroxypropyl methylcellulose and dextran methacrylate showed comparable bone regeneration (~33% new bone) to a commercial collagen membrane in a rabbit calvarial model after eight weeks, without inducing adverse inflammation (M. H. Kim et al., 2018). Other studies have explored the addition of graphene oxide to enhance osteogenic capacity in calvarial defects in rats, promoting increased mineralization and bone formation (Yan et al., 2024).

Injectable hydrogels based on natural polymers such as gelatin and chitosan have been combined with nanoparticles or bioactive agents to enhance mechanical properties and biological response (Luo et al., 2020; Osi et al., 2021).

Injectable biomaterials offer a minimally invasive strategy for addressing bone defects in maxilofacial surgery, anatomically challenging or non-operable sites and reduce surgical morbidity in these anatomically constrained sites (Figure 7) (Mandal et al., 2020; Sun et al., 2023). These findings highlight the relevance of developing injectable hydrogel systems for bone defects where conventional grafts are unsuitable.

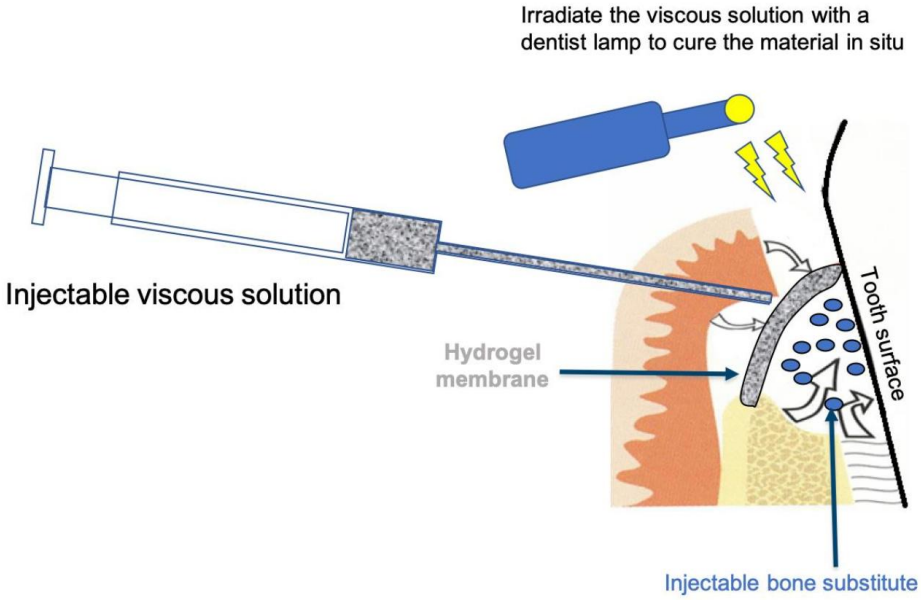

Figure 7. Schematic representation of in situ photopolymerization of an injectable hydrogel for bone tissue repair. The image illustrates the injection of a viscous precursor solution into a bone defect site, followed by in situ light irradiation (e.g., with a dental curing lamp) to induce hydrogel crosslinking. This approach enables minimally invasive application and conformal adaptation to irregular bone geometries. From (Chichiricco et al., 2023).

1.1.3.1 Functionalization Strategies in Hydrogels

Injectable hydrogels can be functionalized with various biological agents to enhance their regenerative performance. These strategies typically target one or more aspects of the healing process, such as inflammation control, oxidative stress reduction, angiogenesis, and osteoinduction.

1. Antioxidants. Oxidative stress is a major contributor to impaired bone healing. Reactive oxygen species (ROS) generated during inflammation can damage cells and the extracellular matrix. Antioxidants such as N-acetylcysteine (NAC) have been incorporated into hydrogels to scavenge ROS and improve cell viability and promote osteogenesis (Figure 8) (C. H. Lin et al., 2016; X. Liu et al., 2023; Vidović et al., 2016). NAC has also been shown to modulate the crosslinking environment of hydrogels, leading to increased porosity and water content (Gomez-Aparicio et al., 2020).

2. Angiogenic Agents. Vascularization is essential for nutrient delivery and waste removal in bone regeneration (Figure 9). Functionalizing hydrogels with angiogenic factors such as VEGF or peptides with pro-angiogenic activity has shown promise in enhancing neovascularization and osteogenesis within the defect site (Anada et al., 2019; Kocak et al., 2020; Priya et al., 2016).

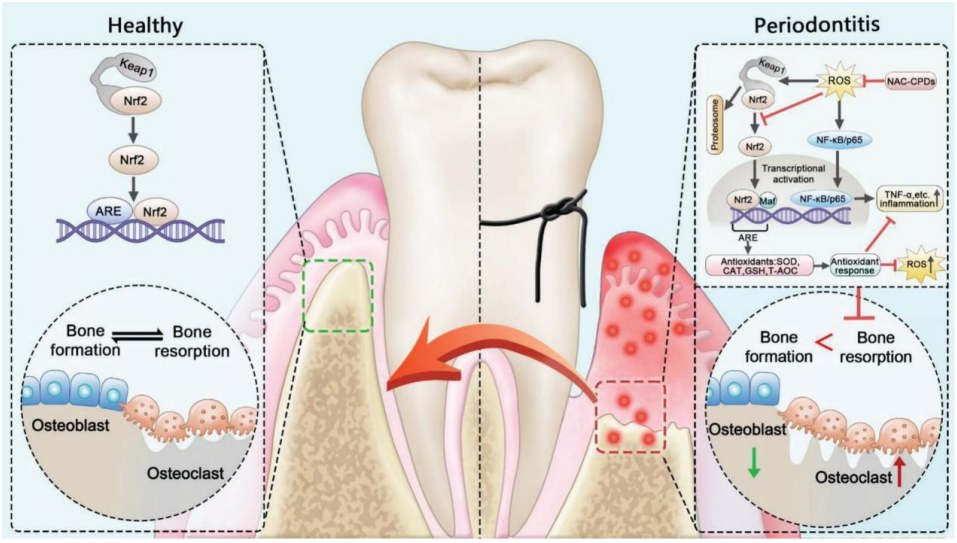

Figure 8. Antioxidant role of NAC in bone homeostasis and periodontitis-associated oxidative stress. In healthy conditions, the Nrf2/Keap1 pathway maintains bone remodeling balance by regulating antioxidant responses. Under periodontitis, elevated reactive oxygen species (ROS) trigger chronic inflammation, suppress osteoblast function, and enhance osteoclast activity, disrupting bone homeostasis. N-acetylcysteine (NAC) and NAC-derived carbonized polymer dots (NAC-CPDs) activate Nrf2 signaling and mitigate oxidative damage, restoring the osteoblast–osteoclast balance. From (X. Liu et al., 2023).

3. Growth Factors. Incorporation of bone morphogenetic proteins (BMPs), fibroblast growth factors (FGFs), and transforming growth factor-beta (TGF-β) has been extensively studied (Sheppard et al., 2022). Although effective in inducing osteogenesis, clinical translation is limited by cost, dose sensitivity, and

short half-life. Controlled release systems within hydrogels can mitigate some of these drawbacks (Chai et al., 2022; García-García et al., 2019; Gothard et al., 2015; Yamamoto et al., 2001).

Few previous studies have combined both antioxidant and pro-angiogenic components in a single hydrogel system. Prior research has incorporated NAC into chitosan or gelatin-based matrices for oxidative stress modulation, while AM or its analogs have been used to promote vascularization and tissue regeneration in models of bone and dental pulp repair (Y. Zhao et al., 2025).

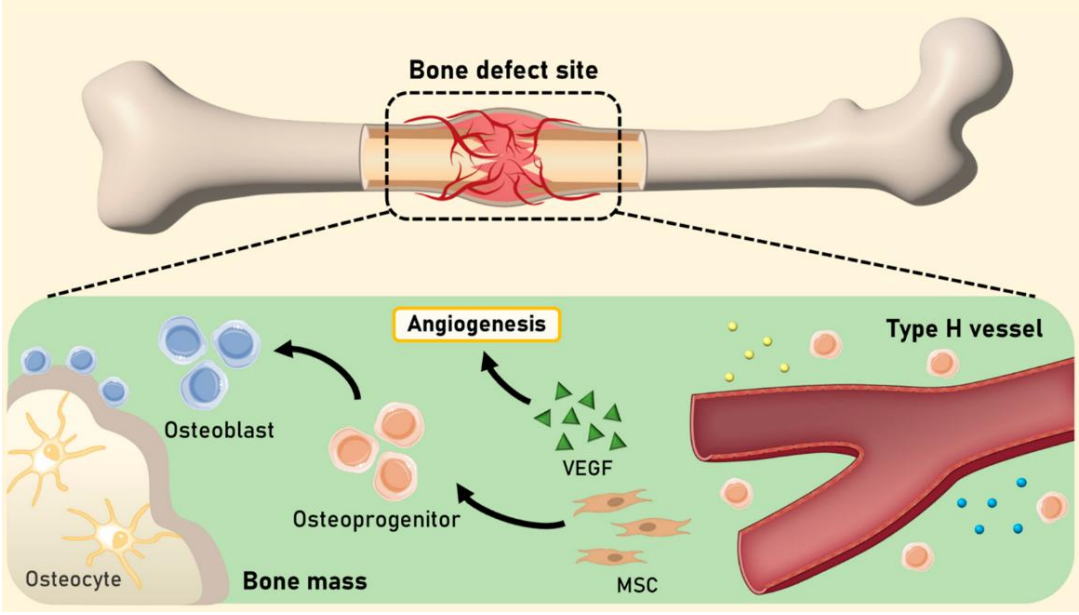

Figure 9. Schematic representation of the cellular and vascular mechanisms involved in bone regeneration. At the bone defect site, type H vessels—characterized by the expression of Endomucin and CD31—modulate osteogenesis by promoting the recruitment and differentiation of osteoprogenitor cells into osteoblasts and eventually osteocytes. Mesenchymal stem cells (MSCs) and endothelial cells secrete VEGF, a key pro-angiogenic factor, which stimulates angiogenesis and enhances bone tissue regeneration. From (Jang and Yoon, 2024).

1.1.4 Biological Rationale for NAC and PAMP

N-acetylcysteine (NAC) is a low molecular weight thiol compound widely recognized for its antioxidant activity. Its free –SH group enables direct scavenging of reactive oxygen species (ROS) and promotes the intracellular synthesis of glutathione (GSH), contributing to redox homeostasis (Zheng et al., 2024). In the context of bone tissue engineering, the oxidative stress generated after trauma, inflammation, or implantation of biomaterials can impair osteoblast function, delay mineralization, and exacerbate osteoclast-mediated resorption (Figure 10). Incorporation of NAC into regenerative strategies has been

proposed to mitigate these effects by restoring the oxidative balance and supporting bone formation (Fontani et al., 2015; H. Kim et al., 2019; X. Li et al., 2021).

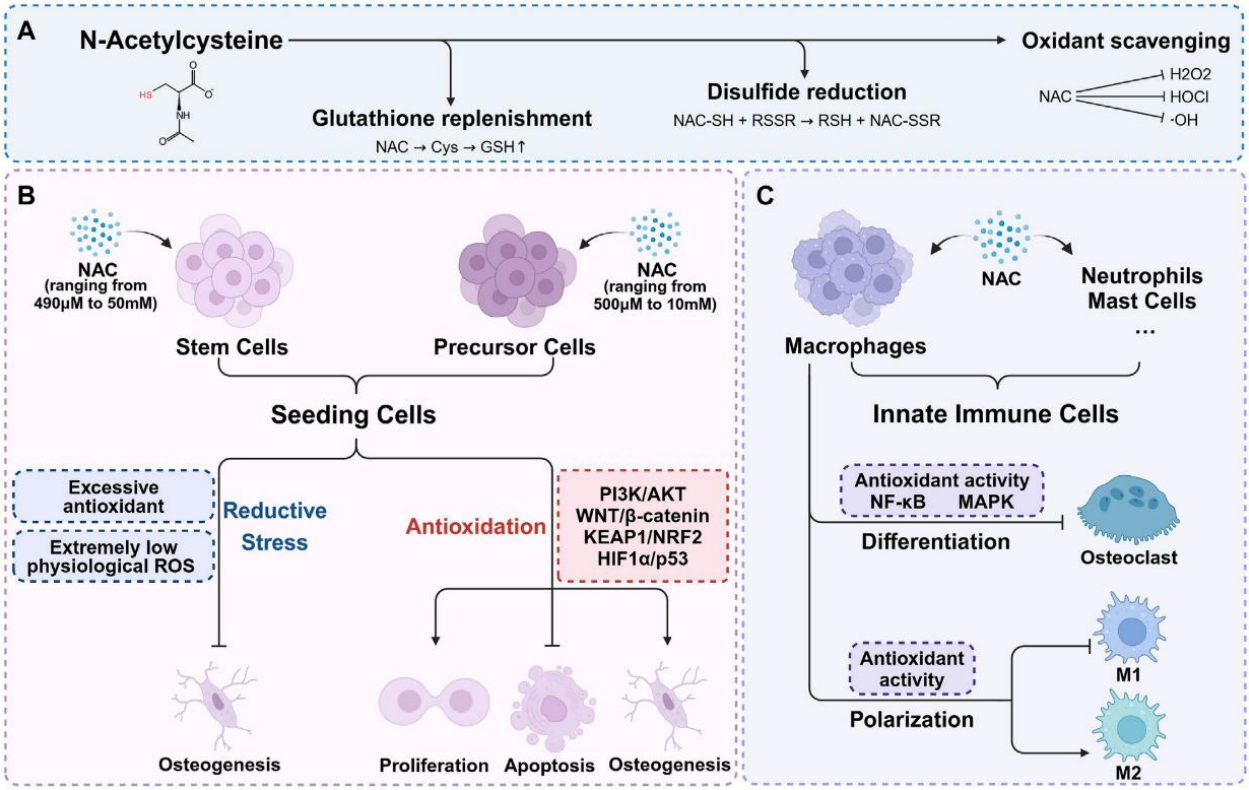

Figure 10. Biological effects and regulatory pathways of N-acetylcysteine (NAC) in bone tissue engineering. (A) NAC enhances glutathione synthesis and reduces disulfide bonds, contributing to oxidative stress mitigation. (B) In seeding cells, including stem and precursor cells, NAC exerts concentration-dependent effects: physiological antioxidation improves proliferation and osteogenesis via PI3K/AKT, WNT/β-catenin, KEAP1/NRF2, and HIF1α/p53 pathways; in contrast, excessive antioxidant levels can induce reductive stress. (C) In innate immune cells, NAC modulates macrophage polarization (favoring M2 over M1) and inhibits osteoclast differentiation by suppressing NF-κB and MAPK signaling pathways. From (Zheng et al., 2024).

In vitro studies have demonstrated that NAC enhances osteoblast viability and differentiation, increases alkaline phosphatase (ALP) activity, and promotes extracellular matrix mineralization. These effects are attributed not only to its antioxidant properties but also to its ability to modulate gene expression related to osteogenesis (Domazetovic et al., 2017). Similar protective outcomes have been observed in oxidative injury models, where NAC prevented H_2O_2-induced damage and preserved osteoblastic function (Meng et al., 2022).

Recent investigations have highlighted the immunomodulatory role of NAC in the osteogenic microenvironment. For example, NAC has been shown to favor the polarization of macrophages toward

the M2 phenotype, which is associated with tissue repair and resolution of inflammation. Additionally, it inhibits osteoclast differentiation and activity while promoting proliferation and osteogenic differentiation of mesenchymal stem cells (MSCs), collectively contributing to a pro-regenerative environment (Zheng et al., 2024).

Beyond its biological effects, NAC also interacts with hydrogel matrices during photo-crosslinking processes. Its thiol group can interfere with radical polymerization, altering the crosslinking density and resulting in hydrogels with increased porosity and faster degradation profiles (Gomez-Aparicio et al., 2020). These changes enhance water uptake, swelling behavior, and nutrient diffusion, all of which are beneficial for cellular infiltration and early-stage tissue regeneration (Fontani et al., 2015).

In preclinical models, such as alveolar bone defects, the use of NAC-loaded scaffolds in combination with dermal-derived stem cells has led to significantly improved outcomes in bone volume and structural organization, further supporting its therapeutic potential (Meng et al., 2022).

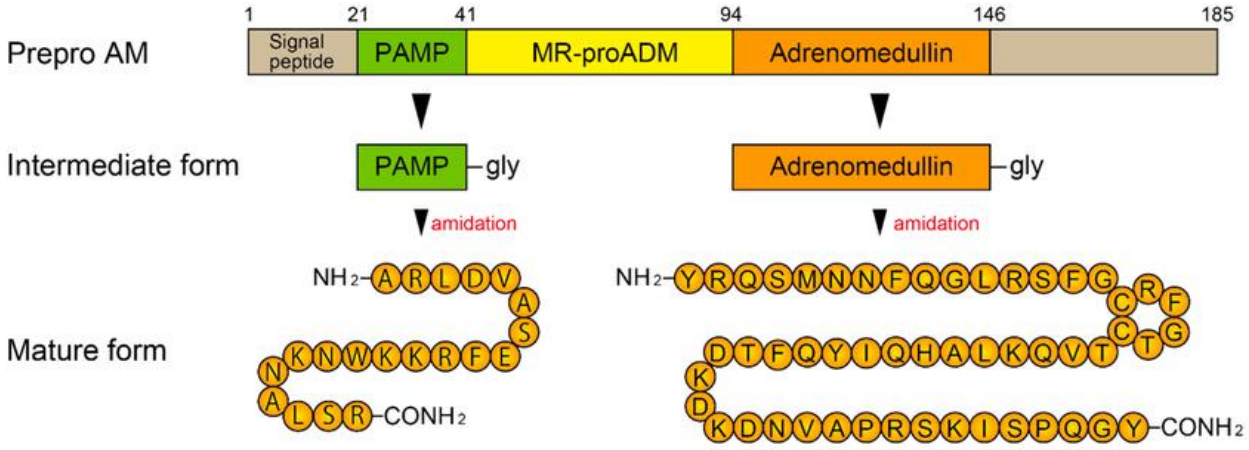

Figure 11. Schematic representation of the processing of preproadrenomedullin (prepro-AM) and the resulting mature peptides PAMP and adrenomedullin. The prepro-AM precursor contains a signal peptide (residues 1–20), followed by the sequences encoding PAMP (residues 21–41) and adrenomedullin (residues 94–146). Upon proteolytic cleavage and amidation, two biologically active peptides are generated: PAMP (20 amino acids) and AM (52 amino acids). From (Kita et al., 2022).

Meanwhile, proadrenomedullin N-terminal 20 peptide (PAMP) is a bioactive peptide derived from the same precursor as adrenomedullin (AM), yet it displays distinct structural and functional properties (Figure 11). Unlike AM and AM2, which contain a C-terminal amidation and a disulfide-bonded ring essential for binding to the calcitonin receptor-like receptor (CLR) in complex with receptor activity-modifying proteins

(RAMP2 or RAMP3), PAMP lacks both motifs. Instead, it exerts its biological effects primarily through atypical chemokine receptor 3 (ACKR3), also known as CXCR7, via β-arrestin–dependent pathways rather than canonical G-protein signaling (F. Wang et al., 2021).

In contrast to the well-documented role of AM in promoting angiogenesis and tissue regeneration, PAMP remains largely unexplored in the context of bone biology. However, PAMP has shown vasodilatory, anti-inflammatory, and cytoprotective effects in various tissues under oxidative or inflammatory stress. These features make it a potential candidate for supporting the vascular and immune environment required for effective bone healing (García-Honduvilla et al., 2013; Martínez et al., 2004a).

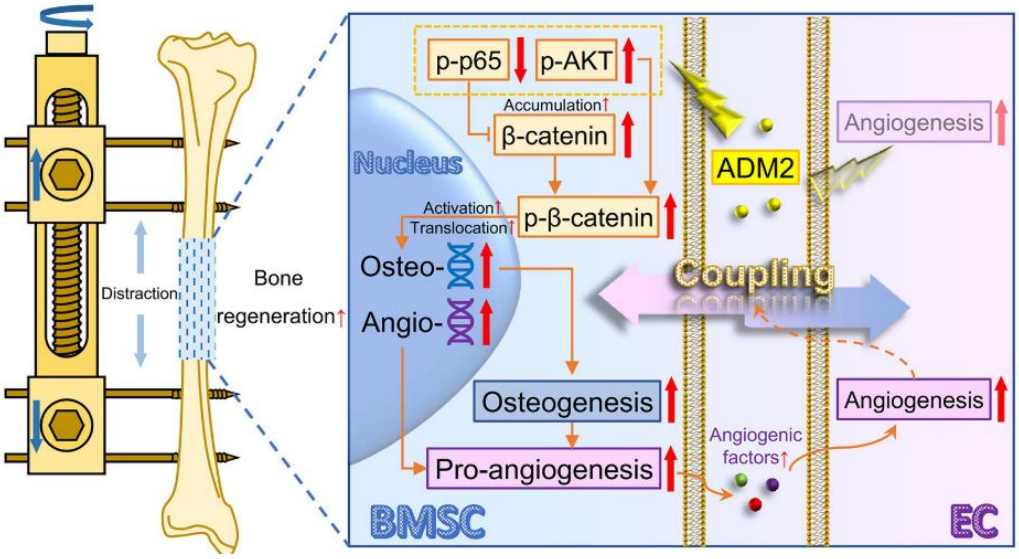

Figure 12. Mechanism of action of ADM2 in bone regeneration through osteogenic–angiogenic coupling. ADM2 promotes bone regeneration in distraction osteogenesis by enhancing osteogenesis and angiogenesis. The signaling cascade involves activation of p65, AKT, and β-catenin pathways in bone marrow-derived mesenchymal stem cells (BMSCs), leading to upregulation of both osteogenic and pro-angiogenic genes. ADM2 also stimulates endothelial cells (ECs) to secrete angiogenic factors, contributing to a feedback loop that couples vascular and bone tissue regeneration. From (F. Wang et al., 2021).

The role of AM in bone is increasingly recognized, particularly for its dual functions in promoting angiogenesis and regulating bone homeostasis (Figure 12). Studies have demonstrated that AM is expressed in osteoblasts and endothelial cells and contributes to bone formation by enhancing osteoblast survival and proliferation, while suppressing osteoclastogenesis (Cornish et al., 1997; Kukita et al., 2021; Naot et al., 2019). Additionally, AM supports vascular network formation within bone defects, which is critical for nutrient delivery and tissue remodeling (Jang and Yoon, 2024). For instance, in models of osteoporosis, AM administration was shown to prevent bone loss and improve trabecular architecture,

suggesting its therapeutic relevance for skeletal disorders (Martínez-Herrero et al., 2016; Y. Zhao et al., 2025).

Despite structural differences, PAMP may complement some of the regenerative roles of AM, particularly under conditions of hypoxia, oxidative stress, or vascular damage. Its smaller size and distinct receptor pathway allow for alternative or synergistic signaling mechanism (García-Honduvilla et al., 2013).

Based on these insights, this study proposes a photo-crosslinkable GelMA–ChMA hydrogel system co-loaded with NAC and PAMP. This design was conceived to explore a platform with potential to support bone tissue repair by addressing key regenerative needs such as oxidative stress modulation and vascular support. While these effects were not directly evaluated in the present work, the inclusion of NAC and PAMP was guided by their documented bioactivity and relevance to bone healing processes. This formulation represents a step toward developing injectable, bioactive hydrogels that combine favorable mechanical and degradation properties with biological potential suited to the repair of complex, non-load-bearing bone defects.

1.2 Justification

Repairing bone defects, particularly in complex anatomical sites such as the maxillofacial region or in cases of non-operable fractures, remains a major clinical challenge. The current gold standard for bone regeneration relies on autografts or allografts. While autografts provide osteoinductive and osteoconductive cues, their use is limited by donor site morbidity, availability, and increased surgical time. Allografts, although more accessible, require surgical implantation and may present challenges of integration, which are not always viable in patients with comorbidities, advanced age, or multiple injuries.

Rigid fixation systems such as plates and screws are often used to stabilize bone segments during healing. These devices involve invasive procedures and may not be feasible in certain anatomical regions, such as thin or highly curved bones.

Injectable hydrogels represent a minimally invasive alternative, capable of adapting to irregular defects while simultaneously serving as structural scaffolds and delivery systems. Many lack the mechanical integrity required to provide temporary support, and few incorporate bioactive signals to guide cell

recruitment, vascularization, and mineralization. Their poor osteointegration and limited angiogenic capacity often result in fibrous encapsulation and resorption of the newly formed tissue.

This is especially problematic in maxillofacial applications, where poor vascularization and complex loading environments demand biologically active and structurally adaptable scaffolds. Similarly, in non-operable fractures, patients may not qualify for surgery due to anatomical constraints or systemic health conditions. A local, biofunctional, injectable material that promotes bone regeneration without invasive fixation would be highly advantageous in these cases.

To address these limitations, this project proposes the development of an injectable hydrogel system composed of methacrylated gelatin and chitosan, photocrosslinked under mild conditions and functionalized with two bioactive agents: N-acetylcysteine (NAC) and pro-adrenomedullin peptide (PAMP). NAC offers antioxidant protection, supports cell viability, and modulates the microarchitecture of the hydrogel network, while PAMP provides emerging pro-angiogenic activity. Their combined delivery within a structurally stable and biodegradable hydrogel platform offers a strategy for sequential bioactivity—initial antioxidant and angiogenic support followed by osteogenic stimulation.

The proposed system aims to overcome biological and mechanical limitations by providing a minimally invasive, injectable, and multifunctional scaffold capable of supporting the complex phases of bone healing. Its relevance extends to a broad range of clinical scenarios, including maxillofacial reconstruction, non-operable fractures, and cases where standard grafts or fixation systems are contraindicated or insufficient.

1.3 Hypothesis

Injectable hydrogels composed of methacrylated gelatin and chitosan containing N-acetylcysteine and pro-adrenomedullin peptide promote bone mineralization.

1.4 Objectives

1.4.1 Main objective

To determine the osteogenic effects of injectable hydrogels composed of methacrylated chitosan and gelatin loaded with N-acetylcysteine and the pro-adrenomedullin peptide.

1.4.2 Specific objectives

1. To synthesize and characterize the physicochemical properties of injectable hydrogels.
2. To evaluate the *in vitro* and *ex vivo* biocompatibility of hydrogels.
3. To assess the *in vitro* and *ex vivo* osteogenic activity of hydrogels.

Chapter 2. Methodology

2.1 Synthesis of hydrogels

Chitosan methacrylate (ChMA) was synthesized by dissolving chitosan at 1.5% (w/v) (BioBasic, CB0660) in 2% (v/v) acetic acid (J.T. Baker, 9508-02), followed by continuous stirring at room temperature for 18 hours. Methacrylic anhydride (Sigma-Aldrich, 276685) was then added at a molar ratio of 1:6 (chitosan:anhydride methacrylate), and the reaction was allowed to proceed at 40 °C for an additional 24 hours (Zanon et al., 2022).

To methacrylate gelatin, a 10% (w/v) gelatin solution (Sigma-Aldrich, G1890) was prepared in 1X phosphate-buffered saline (PBS) and adjusted to pH 9 using 5 M NaOH. Methacrylic anhydride was added sequentially at a ratio of 0.1 mL per gram of gelatin, and stirred at 500 rpm for 3 hours at 40 °C, protected from light (Shirahama et al., 2016) The reaction was stopped by diluting the mixture with PBS (1:5 volume ratio), followed by homogenization for 5 minutes. Unreacted methacrylic anhydride was removed by dialysis (molecular weight cutoff 12–14 kDa) for four days with regular changes of distilled water. The final products were frozen and lyophilized for storage (Li et al., 2021; Luo et al., 2020).

Hydrogels were prepared from 4% GelMA and 3% ChMA in a 3:1 ratio (GC), selected following a series of preliminary tests aimed at ensuring room-temperature injectability (Appendix B, Table B1) and mechanical performance (Appendix D, Figure D1). The ratio was optimized by evaluating gelation at 1:1, 2:1, and 3:1 GelMA:ChMA. (Osi et al., 2021; Saraiva et al., 2015).

All three ratios formed gels upon UV irradiation, with the 3:1 ratio providing superior consistency. To crosslink the polymers, 0.2% (w/v) lithium phenyl-2,4,6-trimethylbenzoylphosphinate (LAP) (Sigma-Aldrich, 900889) was added, followed by exposure to UV light for 60 seconds. The GCN hydrogels were loaded with N- acetylcysteine (NAC) (Sigma-Aldrich, A7250) at 20 mM, which is consistent with concentrations used in hydrogels for wound healing (Gomez-Aparicio et al., 2020), after evaluating its DPPH radical scavenging capacity and cell viability (Appendix A, Figure A1, A2) and hemocompatibility (Appendix, Figure E1, E2). The concentration of pro-adrenomedullin peptide (PAMP) (TOCRIS, 6552) used in the GCP hydrogels (50 mg mL−1) was selected considering the high biological potency of PAMP compared to AM and prior studies on AM delivery. In a bone regeneration model, systemic administration

of over 160 mg of AM(27–52) over four weeks produced significant anabolic effects in bone.(Cornish et al., 2001; Naot et al., 2001) As PAMP exerts biological activity at significantly lower concentrations, (Martínez et al., 2004b) a lower PAMP dose 50 mg mL−1 was selected. GCNP hydrogels were prepared using a combination of NAC and PAMP.

2.2 Physicochemical characterization of hydrogels

2.2.1 Fourier-Transform Infrared Spectroscopy (FTIR)

Fourier-transform infrared spectroscopy (FTIR) was used to analyze the chemical structure of the methacrylate polymers and functionalized hydrogels. Lyophilized samples were analyzed using an Agilent Cary 630 FTIR spectrometer equipped with an attenuated total reflectance (ATR) cell. Spectra were recorded over the range of 600–4000 cm^{-1} to identify characteristic vibrational bands associated with functional groups resulting from the methacrylate process and the incorporation of bioactive compounds.

2.2.2 Swelling Behavior

The swelling capacity of the hydrogels was evaluated to determine their water uptake behavior under physiological conditions. Lyophilized hydrogel discs (approximately 100 µL per sample) were weighed to obtain their initial dry weight (W_0). Hydrogels were incubated in 1X phosphate-buffered saline (PBS) at 37 °C. After that, samples were removed at predefined time points (15, 30, 60, 120, 180, and 1440 minutes) and weighed to obtain swollen weight (W_t). The swelling ratio was calculated using the following equation (Xu et al., 2021):

$$\text{Swelling ratio} = \frac{W_t}{W_0} \quad (1)$$

All measurements were performed in triplicate, and results were expressed as mean ± standard deviation. Swelling kinetics were compared among the different hydrogel formulations (GC, GCN, GCP, GCNP).

2.2.3 Degradation Kinetics

The *in vitro* degradation kinetics of the hydrogels were evaluated under two different conditions:

2.2.3.1 Enzymatic degradation

For the enzymatic degradation assay, hydrogels were first incubated in 1X PBS at 37 °C with agitation at 120 rpm until reaching equilibrium swelling. The initial weight (W_0) of each sample was recorded, after which the hydrogels were transferred to fresh 1X PBS containing 10,000 U/L lysozyme (Sigma-Aldrich, 62970), simulating enzymatic degradation conditions like those found in circulating blood (Leena et al., 2017). Samples were incubated at 37 °C for 1, 3, 7, 14, and 21 days. The degradation medium was replaced every two days to maintain enzymatic activity. At each time point, hydrogels were rinsed with distilled water, freeze-dried, and weighed to determine the remaining dry mass (W_t).

2.2.3.2 Cell-mediated degradation

For the cell-mediated degradation assay, hydrogels were placed in transwell inserts and co-cultured with RAW264.7 macrophages in RPMI 1640 medium supplemented with 10% fetal bovine serum and 1% penicillin/streptomycin. Cells and hydrogels were maintained under standard culture conditions (37 °C, 5% CO_2) for up to 21 days. The medium was replaced every two days. At each time point (days 1, 3, 7, 14, and 21), hydrogels were collected, rinsed, freeze-dried, and weighed to determine residual mass (W_t). The degradation percentage was calculated using the following equation:

$$\text{Remaining mass } (\%) = \frac{W_0 - W_t}{W_0} x100 \quad (3)$$

All measurements were performed in triplicate, and results were expressed as mean ± standard deviation.

2.2.3.3 *In vivo* degradation

To evaluate the *in vivo* degradation of the hydrogels, 100 µL of each formulation (GC, GCN, GCP, and GCNP) were subcutaneously implanted in C57BL/6 mice (n = 4 per condition) under aseptic conditions. Each mice received two hydrogel implants, one in each thigh, by creating lateral subcutaneous pockets that were

sutured with a single stitch to secure the material in place. A total of two mice were used per formulation. All procedures were carried out at the Centro de Investigación Biomédica de La Rioja (CIBIR), Spain, CEEA-CIBIR 04/10 in compliance with institutional and national guidelines for animal care and experimentation and were approved by the CEEA-CIBIR ethics committee.

After 11 days, animals were euthanized, and the implantation sites, including surrounding tissue, were excised, fixed in 4% paraformaldehyde, embedded in paraffin, sectioned, and stained with hematoxylin and eosin (H&E). Histological analysis was performed to assess hydrogel degradation, cellular infiltration, and host tissue response. Pictures were taken with Leica DMI6000B microscope (Leica Biosystems, Nussloch, Germany) at 20 X magnification.

2.2.4 Release profile

The release kinetics of bioactive compounds from the hydrogels were evaluated over a 14-day period by quantifying the free amino groups present in the release medium. (Friedman, 2004) Hydrogels containing N-acetylcysteine (NAC), pro-adrenomedullin peptide (PAMP), or both, were incubated in 1X PBS at 37 °C. At predefined time points (15, 30, 60, 120, 180, and 1440 minutes, and days 3, 7, and 14), aliquots of the supernatant were collected and replaced with fresh PBS to maintain sink conditions.

The quantification of released compounds was performed using the ninhydrin assay (Sigma-Aldrich, N4876). A 2.5% ninhydrin solution was freshly prepared and mixed with each sample at a 2:1 ratio (ninhydrin:sample). The reaction mixtures were incubated at 95 °C for 10 minutes and allowed to cool to room temperature before measuring the absorbance at 570 nm. The concentrations of NAC and PAMP were determined by interpolation in a glycine standard curve (Appendix C, Figure C2). Cumulative release was calculated using the following equation (Ji et al., 2014):

$$\text{Cumulative release } (\%) = \frac{M_t}{M_\infty} x100 \quad (2)$$

Where M_t is the amount of compound released at time t, and $M\infty$ is the total amount released at saturation. All experiments were performed in triplicate, and results were expressed as mean ± standard deviation.

2.3 Morphological Characterization

The microstructure of the hydrogels was examined by scanning electron microscopy (SEM) to evaluate surface features and pore morphology. For imaging, hydrogels were first frozen and then lyophilized to preserve their structure. Prior to imaging, the samples were sputter-coated with a thin layer of gold to enhance conductivity. SEM imaging was performed using a JSM-IT500HR (JEOL Ltd., Japan) operating at an accelerating voltage of 1 kV under variable pressure mode. Representative images were captured from both the surface and cross-sectional areas of each hydrogel formulation.

2.3.1 Pore Size Analysis

Quantitative analysis of pore size was performed using scanning electron microscopy (SEM) images of the lyophilized hydrogels. Images at 100× magnification were analyzed using ImageJ software (National Institutes of Health, USA). For each formulation, three representative images from different regions of the sample were used. Pore diameters were measured manually using the built-in measurement tools, calibrating pixel-to-micrometer ratios based on the scale bars provided by the microscope. At least 50 pores were measured per formulation to ensure statistical relevance. The average pore size and standard deviation were calculated, and frequency distribution histograms were generated to assess pore size variability among the hydrogel groups.

2.4 Mechanical Properties

The mechanical performance of the hydrogels was evaluated under uniaxial compression by determining the Young's modulus (ε), compression strength (σF), and toughness. Compression tests were conducted using a texture analyzer (Brookfield CT3-10Kg, AMETEK Brookfield, Middleboro, MA, USA) equipped with a cylindrical stainless-steel probe (TA11/1000, 25.4 mm diameter, 35 mm height).

Hydrogel discs (6 mm diameter) were pre-hydrated in PBS and placed on a flat testing platform at room temperature. Samples were compressed at a constant speed of 0.5 mm/s until deformation or failure occurred, following a protocol adapted (Araiza-Verduzco et al., 2020).

Stress–strain curves were generated from the force-displacement data (Appendix D, Figure D2). The Young's modulus (ε) was calculated from the slope of the linear region of the curve. The compression strength (σF) was defined as the maximum stress value recorded before the first structural failure, and toughness was determined as the area under the curve, representing the energy absorbed by the material prior to failure.

2.5 Biocompatibility

The biocompatibility of the hydrogels was assessed through *in vitro* and *ex vivo* viability assays using pre-osteoblastic cells and calvarial bone tissue, respectively.

2.5.1 *In Vitro* Viability

Indirect cytotoxicity was evaluated using MC3T3-E1 pre-osteoblastic cells. Cells were seeded in 24-well plates at a density of 7,500 cells/well and allowed to adhere for 24 hours. Subsequently, hydrogel discs (100 µL) were placed in transwell inserts (0.4 µm pore size) and incubated in indirect contact with the cells for 1, 3, and 5 days. At each time point, cell viability was assessed using the MTT assay. A solution of MTT (0.5 mg/mL) was added to each well and incubated at 37 °C for 4 hours. The resulting formazan crystals were solubilized using a 10% SDS solution in 0.1 M HCl (Kumar et al., 2018). Absorbance was measured at 570 nm using a microplate reader (EPOCH, BioTek), and cell viability was calculated as:

$$\text{Viability (\%)} = \frac{Abs_{sample} - Abs_{blank}}{Abs_{control} - Abs_{blank}} x100 \quad (4)$$

2.5.2 *Ex vivo* Viability

Ex vivo viability was evaluated using a murine critical size calvarial defect model. Calvariae were extracted from four-day-old mice and sectioned to create 2 mm full-thickness circular defects at the center. Hydrogels were implanted within the defect site, and the samples were cultured concave side down in 48-well plates containing α-MEM supplemented with 0.1% bovine serum albumin (BSA), 1% penicillin/streptomycin, and insulin (Ji et al., 2014; X. Wu et al., 2014). The culture medium was replaced every two days and maintained for 14 days under standard conditions (37 °C, 5% CO_2).

At the end of the culture period, tissue viability was assessed using the Live/Dead Kit (Sigma-Aldrich, 04511), following the manufacturer's protocol. Viable cells and tissue were identified by calcein-AM (green fluorescence), and non-viable cells by ethidium homodimer-1 (red fluorescence). Autofluorescence of the calvarial tissue appeared in the blue channel.

2.6 Bioactivity

Bioactivity was assessed through mineralization assays in both 2D and *ex vivo* models.

2.6.1 *In Vitro* Mineralization

Bone marrow-derived cells were obtained from the femur and tibia of 8-week-old mice by flushing with 1X PBS (Amend et al., 2016). Cells were cultured in α-MEM supplemented with 10% fetal bovine serum (FBS) and 1% antibiotic-antimycotic for 48 hours. Adherent cells were then collected and seeded at a density of 45,000 cells/well in 24-well plates. After 24 hours, osteogenic differentiation medium (α-MEM + 25 µg/mL ascorbic acid + 5 mM β-glycerophosphate) was added, and hydrogel-loaded transwells were inserted into each well. The medium was replaced every 3 days for 21 days (B. Liu et al., 2023).

At the end of the incubation period, cells were fixed with 4% paraformaldehyde for 20 minutes. Mineralization was evaluated by Alizarin Red S (ARS) staining (2%, pH 4.2) for 3 minutes at room temperature, followed by multiple rinses with distilled water. Alkaline phosphatase (ALP) staining was also performed according to the manufacturer's instructions (Sigma-Aldrich, 86R-1KT).

2.6.2 *Ex Vivo* Calvaria Mineralization

Four-day-old BALB/c mice were euthanized according to ethical guidelines and calvariae were harvested aseptically. The bone was sectioned along sagittal and coronal sutures, and each quarter was placed in a 48-well plate with DMEM supplemented with 0.1% bovine serum albumin (BSA), 1% penicillin/streptomycin, and insulin as a positive control (Feher et al., 2021). After 24 hours of preincubation, a full-thickness circular defect (2 mm in diameter) was created in the center of each calvaria. Hydrogels were placed within the defect area, and the calvariae were cultured concave side down

for 14 days, with medium changes every 2 days. At the endpoint, calvariae were stained using a Live/Dead viability kit (Sigma-Aldrich, 04511), ARS, and ALP to assess cell viability and bone matrix mineralization.

2.7 Statistical Analysis

All data are presented as mean ± standard deviation (SD) or standard error of the mean (SEM), as specified in each figure legend. Statistical analyses were performed using GraphPad Prism v8.0.2 (GraphPad Software, San Diego, CA, USA). One-way ANOVA was used for comparisons of porosity, mechanical properties, viability, and mineralization assays. Two-way ANOVA was applied to swelling, degradation, and cumulative release data. Tukey's or Dunnett's post hoc tests were used for multiple comparisons, as indicated in each experiment. Statistical significance was considered at $p < 0.05$. In figures where asterisks are used, the following notation applies: $p < 0.05$ (*), $p < 0.01$ (**), and $p < 0.001$ (***). In the MTT viability figure, exact p values are shown above the bars, with corresponding asterisk levels noted in the figure legends. Non-significant comparisons are not shown unless explicitly stated.

Chapter 3. Results and Discussion

3.1 Physicochemical Characterization of Hydrogels

3.1.1 Chemical Composition Characterization of the Hydrogels

As a first step in the physicochemical characterization of the hydrogels, we performed Fourier-transform infrared spectroscopy (FTIR) on lyophilized samples to evaluate their chemical composition and structural modifications resulting from the methacrylation process (Figure 13).

The spectra confirmed the successful chemical modification of both gelatin and chitosan, as evidenced by the appearance of characteristic bands near 1635 cm^{-1} (C=C stretching) and in the 3100–3000 cm^{-1} region (weak C–H stretching). Additionally, characteristic peaks from the base polymers were preserved, including Amide I (~1650 cm^{-1}) and Amide II (~1550 cm^{-1}) bands (Fonseca et al., 2020; Saraiva et al., 2015). In ChMA-containing samples, a band appeared around 1730 cm^{-1}, which can be attributed to ester-type carbonyl groups introduced during the methacrylation reaction. After photopolymerization, the significant reduction or disappearance of the C=C stretching band indicated the successful consumption of double bonds, validating the crosslinking reaction (Kwon and Jeong, 2020). Notably, GC hydrogels exhibited a greater decrease in this signal, suggesting efficient network formation between GelMA and ChMA components (Osi et al., 2021).

The incorporation of NAC was associated with additional signals and changes in the 1700–1600 cm^{-1} region. Moreover, no distinct thiol (SH) stretching band was detected around 2550–2600 cm^{-1}, which is usually present in free NAC, suggesting that interactions may have occurred between NAC and functional groups in the polymer matrix through hydrogen bonding or potential covalent interactions with available functional groups, such as amides or hydroxyls. These interactions are consistent with previous reports indicating the reactivity of NAC with aldehydes or electrophilic moieties in biopolymeric systems (Gomez-Aparicio et al., 2020).

In contrast, hydrogels containing PAMP exhibited subtle variations in the 800–1200 cm^{-1} region, which may correspond to changes in C–O or C–N vibrations, potentially due to non-covalent interactions

between the peptide and the hydrogel network. The observed spectral changes suggested interactions that may alter the structural organization of the hydrogel network. Such interactions could influence the hydrogel's mechanical behavior, degradation profile, and release kinetics, as explored in subsequent sections.

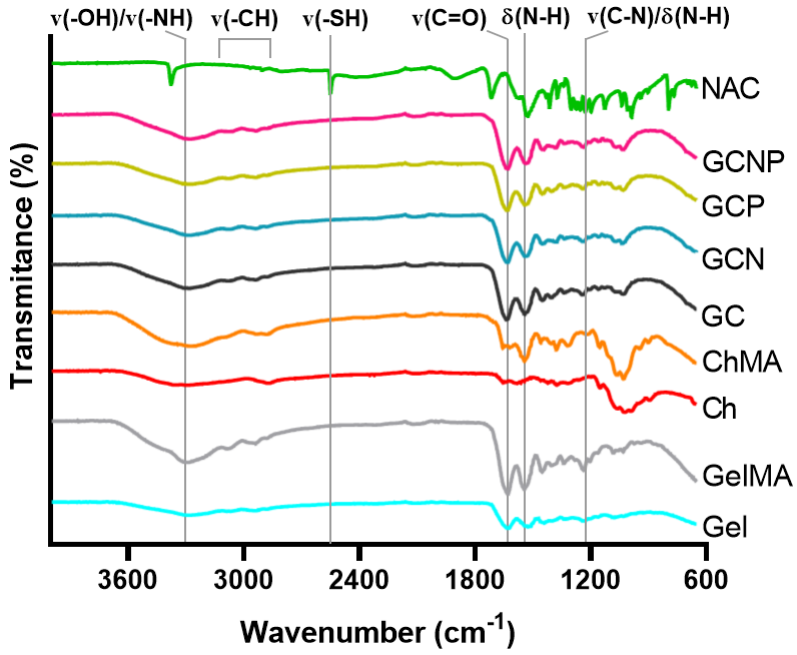

Figure 13. FTIR spectra of individual components and GC hydrogel formulations containing NAC and/or PAMP. Fourier-transform infrared (FTIR) spectra of the base biopolymers—gelatin (Gel), methacrylated gelatin (GelMA), chitosan (Ch), and methacrylated chitosan (ChMA)—as well as the base hydrogel (GC), and the formulations loaded with N-acetylcysteine (GCN), pro-adrenomedullin peptide (GCP), or both bioactive compounds (GCNP). Characteristic absorption bands corresponding to functional group vibrations were identified, including hydroxyl and amine stretching (ν(-OH)/ν(-NH)), alkyl groups (ν(-CH)), thiol groups (ν(-SH)), carbonyl (ν(C=O)), amide bending (δ(N-H)), and C–N stretching (ν(C–N)).

3.1.2 Swelling Capacity of the Hydrogels

To assess their water uptake capacity under physiological conditions, we evaluated the swelling behavior of the hydrogels (Figure 14). All formulations exhibited a gradual increase in weight during the initial hours of immersion in PBS, stabilizing around 24 hours.

The base formulation (GC) exhibited limited swelling, suggesting a compact and tightly crosslinked polymer network. GCN hydrogels showed a similar swelling profile to GC, with no significant differences observed at most points of time. This suggests that, under the tested conditions, the incorporation of NAC did not substantially alter the hydrogels water absorption capacity.

In contrast, GCP and GCNP hydrogels exhibited a significantly higher swelling ratio, particularly during the initial hours, and maintained this difference throughout 24 hours. The higher swelling in GCP and GCNP may be related to modifications in the network architecture induced by the presence of PAMP. Although the peptide does not directly introduce strongly hydrophilic groups, it may influence the polymer packing or crosslinking efficiency, facilitating greater water penetration. Notably, GCNP showed the highest swelling ratio overall, indicating a possible combined effect of both additives, and promotes a more hydrated and porous network, favorable for bioactive compound release and tissue integration. These results are essential in tissue engineering, where swelling capacity influences cellular infiltration and nutrient diffusion (Feng et al., 2019b).

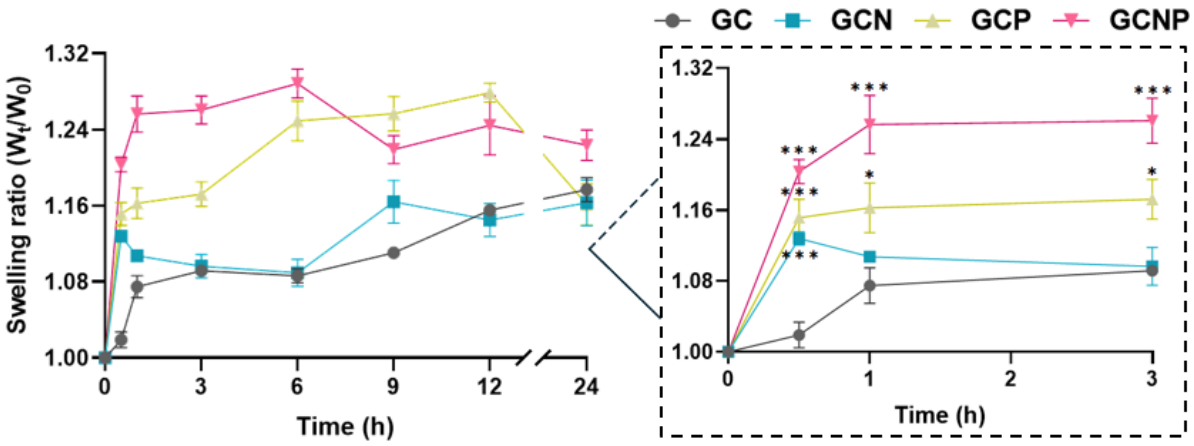

Figure 14. Swelling kinetics of GC hydrogels functionalized with NAC and/or PAMP. Swelling ratio (Wt/W0) of gelatin methacrylate and chitosan methacrylate (GC) hydrogels, either unloaded (GC) or functionalized with N-acetylcysteine (GCN), pro-adrenomedullin (GCP), or both compounds (GCNP), over 24 hours of incubation in PBS 1X at 37 °C. The inset graph highlights an extended analysis of the first 3 hours, where a significant difference in initial water absorption is observed in the GCNP and GCP formulations compared to GC and GCN. The GCNP group exhibited the highest swelling capacity, remaining significantly above the other formulations throughout the period. Data are presented as mean ± SEM (n = 3). Statistical differences were analyzed using two-way ANOVA followed by Dunett's post hoc test. At 1 h, GCNP was significantly higher than GC (***, $p < 0.001$) and GCN (***, $p < 0.001$). At 3 h, GCP was significantly higher than GC (*, $p = 0.01$), and GCNP remained higher than GC (***, $p < 0.001$) until equilibrium was reached after 24 h.

Comparable swelling ratios have been reported in thiol-modified hydrogels used for biomedical applications. Reported that hyaluronic acid-based hydrogels modified with disulfide linkages (HA-SS-HA) exhibited a volume swelling ratio of approximately 1.9 within three days of incubation, stabilizing thereafter. This degree of hydration was sufficient to enable drug release while preserving the structural integrity of the hydrogel matrix.(Xu et al.,2021).

Compared to synthetic or hybrid systems, such as GelMA–PEGDA or GelMA–laponite composites, which often exhibit lower swelling ratios due to increased stiffness and denser crosslinking, the GCNP formulation demonstrates a favorable balance between water absorption and structural integrity (Andrade et al., 2023).

3.1.3 Degradation Profile of the Hydrogels

To characterize the degradation profile of the hydrogels, we conducted *in vitro* enzymatic and cell-mediated assays, as well as *in vivo* subcutaneous implantation studies.

In the enzymatic degradation assay using lysozyme (Figure 15A), GC hydrogels retained over 75% of their initial mass after 21 days, indicating high structural stability. In contrast, GCN and GCNP hydrogels showed faster degradation. By day 14, both formulations had lost nearly all their mass, with GCNP degrading slightly faster than GCN. These results suggest that the incorporation of NAC promotes hydrogel susceptibility to enzymatic cleavage, possibly by altering the crosslinking density or introducing sites more accessible to enzymatic attack (Guindani et al., 2020).

The cell-mediated degradation assay with RAW264.7 macrophages (Figure 15B) showed a similar pattern. GC hydrogels remained structurally stable, while GCN and GCNP underwent significant mass loss. GCNP reached nearly complete degradation by day 14, slightly faster than GCN. These results reinforce the idea that NAC destabilizes the network structure, possibly by altering crosslinking or enhancing porosity, which could facilitate enzymatic access and macrophage-mediated degradation (Yahyouche et al., 2011).

The accelerated degradation observed in GCN and GCNP aligns with previous findings in GelMA–based systems incorporating thiolated molecules. NAC can disrupt polymer networks by interfering with crosslinking or by introducing labile bonds, enhancing degradation under enzymatic or cellular conditions (Gomez-Aparicio et al., 2020).

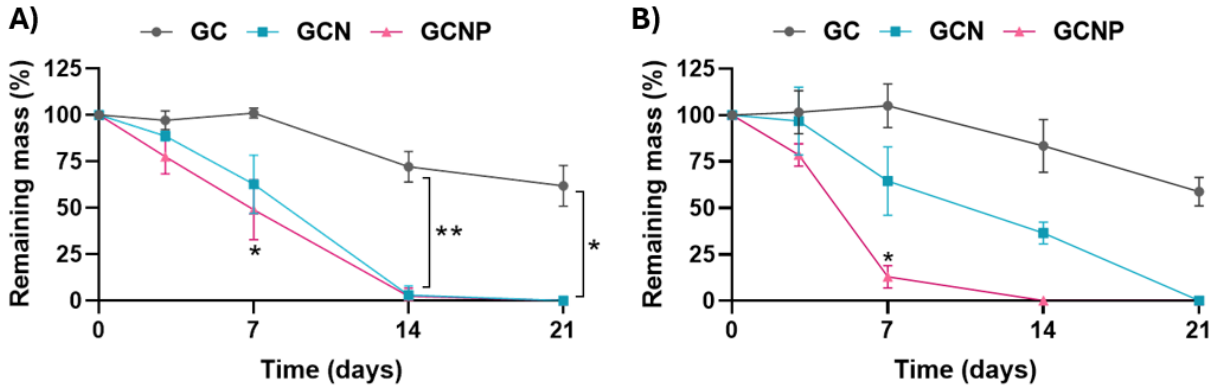

Figure 15. Evaluation of degradation of GC hydrogels functionalized with NAC and/or PAMP *in vitro*. (A) Remaining mass percentage of methacrylated gelatin and chitosan (GC) hydrogels, unloaded (GC) or functionalized with NAC (GCN) and both compounds (GCNP), after *in vitro* incubation in PBS 1X with type II collagenase at 37 °C for 21 days. (B) Degradation in the presence of RAW 264.7 cells cultured in indirect contact with the hydrogels under physiological conditions. GCNP hydrogels degraded significantly faster than GC, with both GCN and GCNP nearly fully degraded by day 14, while the GC group retained over 50% of its original mass. Data are presented as mean ± SEM (n = 3). Statistical differences were analyzed using two-way ANOVA followed by Tukey's post hoc test. Significant differences were found at day 7 between GC and GCNP (*, p = 0.04), at day 14 GC vs. GCNP (**, p = 0.001), and at day 21 GC vs. GCN (*, p = 0.02).

In vivo degradation was assessed by subcutaneous implantation in C57BL/6 mice and evaluated by histological staining after 11 days (Figure 16). GC hydrogels remained intact with minimal cellular infiltration. In contrast, GCN and GCNP showed advanced material disintegration and were more extensively infiltrated by host cells, supporting the *in vitro* findings. GCNP exhibited the most pronounced tissue interaction. Interestingly, GCP—which was only evaluated *in vivo*—remained intact but was surrounded by a fibrotic capsule, suggesting a distinct host response possibly indicative of foreign body reaction.

These findings highlight the influence of hydrogel composition on degradation kinetics and host tissue response. NAC incorporation was associated with increased degradability, while the combination of NAC and PAMP in GCNP further enhanced this effect. In contrast, GCP exhibited structural stability *in vivo* but triggered encapsulation, which may limit integration depending on the application.

This tunable degradation behavior is particularly relevant in bone regeneration, where scaffold degradation must occur in coordination with the cellular processes of osteogenesis and extracellular matrix deposition. A degradation profile that provides initial mechanical support and space maintenance during early phases—such as inflammatory response, progenitor cell recruitment, and early differentiation—but clears intime to avoid interference with tissue ingrowth, is considered optimal

(Hollister, 2005). In this context, the faster degradation of GCNP may support early remodeling events while minimizing long-term scaffold persistence that could hinder new bone formation.

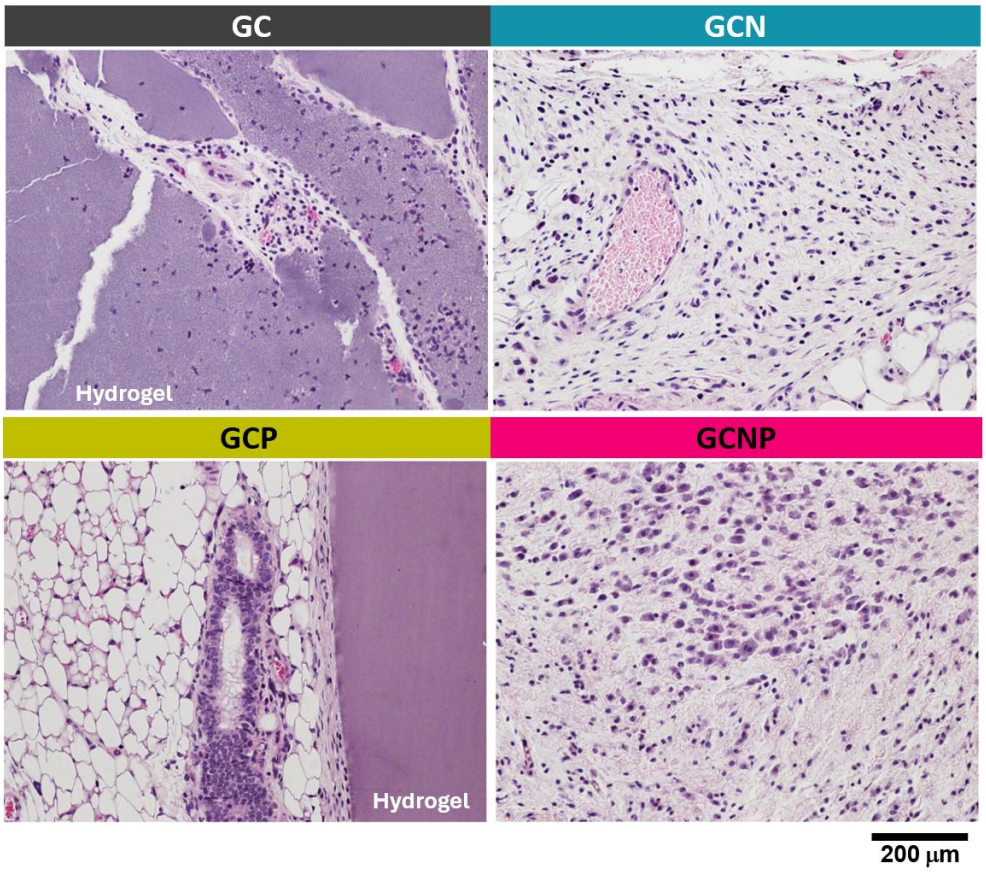

Figure 16. Representative images of *in vivo* degradation following subcutaneous implantation of hydrogels in C57BL/6 mice, retrieved after 11 days. H&E-stained histological images show increased cellular infiltration and hydrogel disintegration in GCN and especially GCNP, compared to GC, which retained its structure. GCP induced the formation of a fibrotic capsule encapsulating the hydrogel. Scale bar: 200 µm.

3.1.4 Cumulative Release of NAC and PAMP

To evaluate the delivery profile of NAC and PAMP from the GC-based hydrogel formulations, we performed cumulative release studies over 14 days. The results revealed distinct release behaviors depending on the incorporated bioactive compounds (Figure 17).

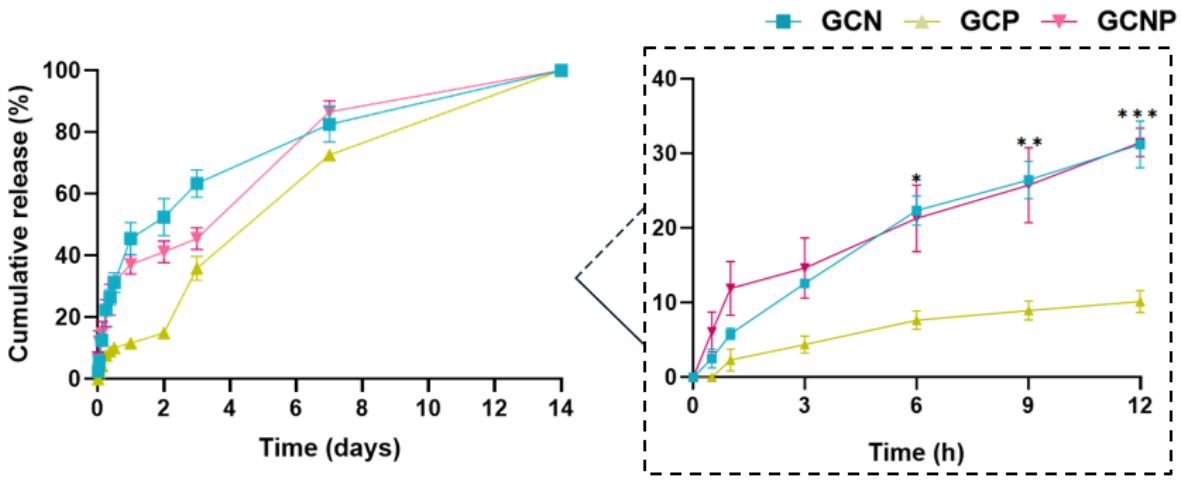

Figure 17. Cumulative release of bioactive compounds from GC hydrogels. Release profiles of N-acetylcysteine (GCN), pro-adrenomedullin (GCP), and their combination (GCNP) from methacrylated gelatin and chitosan (GC) hydrogels over 14 days in PBS 1X at 37 °C. The inset graph highlights the initial 12 hours, showing that GCN and GCNP exhibit significantly higher early release compared to GCP. GCNP achieved a balanced release profile, combining an initial burst with sustained delivery. Data are presented as mean ± SEM (n = 3). Statistical differences were analyzed using two-way ANOVA followed by Tukey's post hoc test. At 6 h, NAC hydrogels released significantly more than GCP (*, $p = 0.03$), which increased at 9 h (**, $p = 0.002$). By 12 h, GCN remained significantly higher than GCP (***, $p < 0.001$).

GCN hydrogels, which contain NAC alone, exhibited a pronounced burst release, with over 30% of the total NAC released within the first 12 hours. This corresponds to ~6 mM of NAC, assuming a loading concentration of 20 mM, which is consistent with the absolute quantification performed using a standard curve method (Appendix C, Figure C2B). This rapid initial phase was followed by a gradual release extending through day 14. This profile suggests that NAC interacts weakly with the hydrogel matrix or is predominantly located near the surface, facilitating its diffusion once the hydrogel is hydrated. A similar burst release has been reported in gelatin-based hydrogels, where the compound's high solubility and limited crosslinking interactions contribute to rapid diffusion from the surface (Leena et al., 2017; Ning et al., 2019)

In contrast, GCP hydrogels showed a slower and more gradual release, with less than 20% released within the first 48 hours and a sustained release thereafter. This behavior is likely due to electrostatic and hydrogen bonding interactions between PAMP and the polymeric network, which help retain the peptide within the matrix. Although these interactions were not directly characterized, sustained delivery of peptides from hydrogels has been previously associated with such molecular interactions that slow diffusion (Ghosh et al., 2019; B. Liu et al., 2023).

GCNP hydrogels, which incorporated both NAC and PAMP, exhibited an intermediate release profile. Approximately 25% of the loaded compounds were released within the first 24 hours, followed by a sustained release like that observed in GCP. This behavior implies that the presence of both compounds modulates the network's structure and porosity in a way that balances rapid and extended release. The synergistic interaction between NAC and PAMP may influence their spatial distribution and binding within the matrix, allowing for a dual-phase release advantageous for sequential biological responses.

These findings underscore the importance of hydrogel composition in tailoring the release kinetics of therapeutic molecules and suggest that GCNP provides an optimal profile for applications requiring both immediate and long-term bioactivity. Future studies should consider quantifying individual compound release in dual-loaded systems and evaluating whether the observed release profile correlates with functional outcomes such as cell recruitment, angiogenesis, or matrix remodeling.

3.2 Morphological Characterization of the Hydrogels

Porosity is a critical parameter in tissue engineering applications, as it influences cell infiltration, nutrient transport, matrix deposition, and vascularization. We evaluated the morphology of the hydrogels by scanning electron microscopy (SEM), which revealed formulation-dependent differences in microarchitecture (Figure 18).

The base GC hydrogel exhibited a dense and compact microstructure with small, irregularly distributed pores. **T**his suggests a tightly cross-linked network, which aligns with the limited swelling and high stability observed in previous sections. In contrast, hydrogels functionalized with NAC (GCN) and both NAC and PAMP (GCNP) displayed a more open and porous architecture, with well-defined pore walls and larger interconnected voids. The GCP hydrogel, containing only PAMP, presented a compact structure like GC.

Quantitative analysis of pore size confirmed these differences (Figure **1**9). GCN and GCNP showed significantly larger average pore sizes than GC and GCP ($p < 0.001$), with GCN exhibiting the highest variability. This result suggests that NAC alters the gelation process, possibly by interfering with chain packing or crosslinking, leading to a more heterogeneous and less dense network. While the exact mechanism was not determined in this study, previous reports indicate that thiol-containing compounds can disrupt physical entanglement or delay crosslinking kinetics, resulting in larger pores (Gomez-Aparicio et al., 2020).

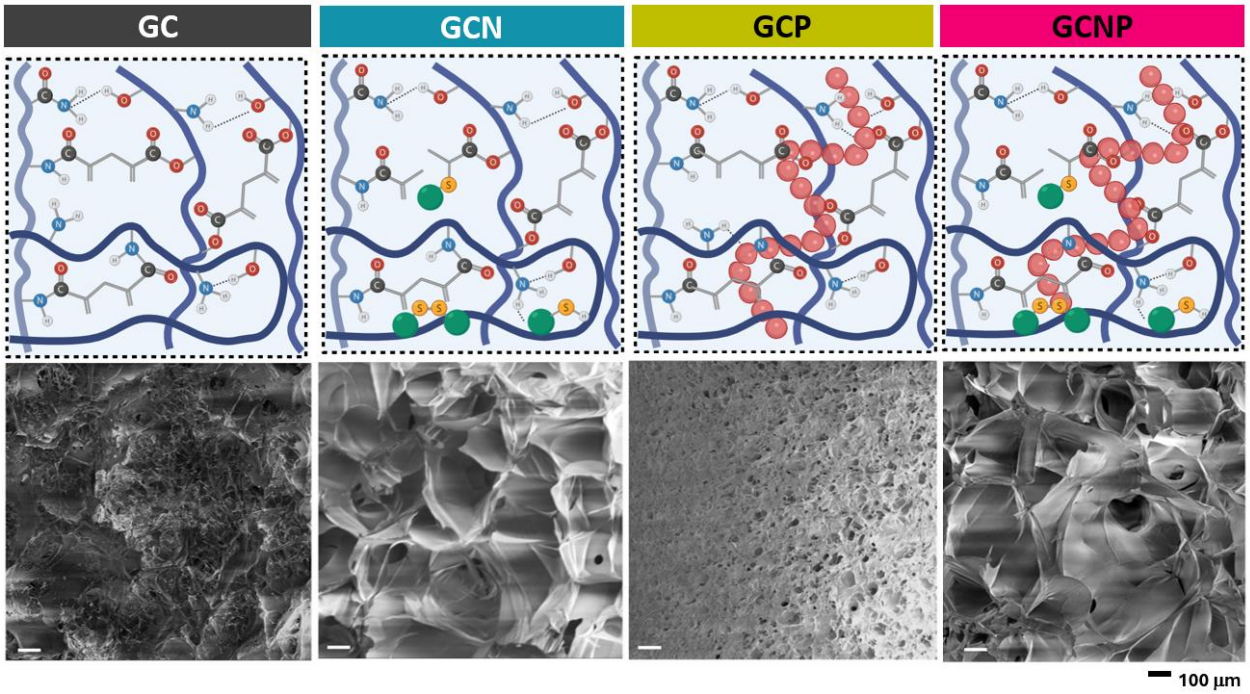

Figure 18. Schematic and morphological characterization of dual-crosslinked hydrogels with different bioactive treatments. Representative diagrams (top), SEM micrographs (middle), and pore size distribution (bottom) of methacrylated gelatin and chitosan (GC) hydrogels, with or without N-acetylcysteine (GCN), pro-adrenomedullin (GCP), or both (GCNP). SEM images show morphological differences associated with compound incorporation, with more porous structure observed in NAC-containing hydrogels. Pore size quantification revealed a higher frequency of large pores in GCN and GCNP compared to GC and GCP. Scale bar: 100 µm.

It is important to note that porosity was inferred from SEM images of lyophilized samples, which may differ from the hydrated state relevant to *in vivo* conditions. Complementary techniques such as confocal microscopy or mercury porosimetry would help validate these findings under physiological conditions.

The increase in pore size in GCN and GCNP may enhance the diffusion of nutrients and bioactive compounds, as well as facilitate cellular migration, making these systems more suitable for regenerative applications where cell infiltration is critical (Lien et al., 2009). In contrast, the compact structure observed in GC and GCP may limit such processes but could provide mechanical robustness where slower degradation and low permeability are desired.

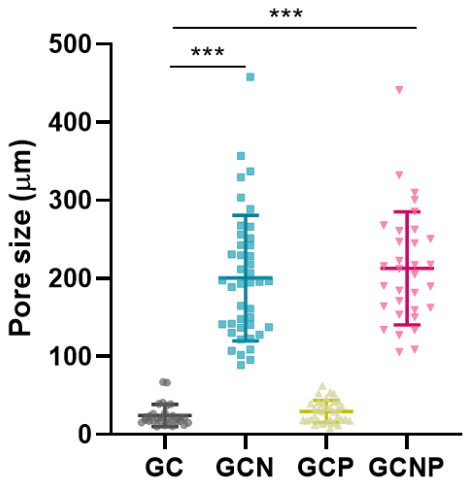

Figure 19. Pore size comparison in GC hydrogels functionalized with NAC and/or PAMP. Pore size measured in GC, GCN, GCP, and GCNP hydrogels from SEM images. A significant increase in pore size was observed in NAC-containing groups (GCN and GCNP) compared to GC, suggesting a NAC-induced effect on hydrogel porous architecture. Data are presented as mean ± SD, with *n* corresponding to the number of pores measured per group (GC: 30 pores, GCN: 42 pores, GCP: 34 pores, GCNP: 32 pores). Statistical differences were analyzed using one-way ANOVA followed by Tukey's post hoc test. Results showed that GCN and GCNP were significantly higher than GC (***, $p < 0.001$), and GCN also significantly higher than GCP (***, $p < 0.001$).

When compared to other systems, the pore sizes obtained for GCN (200.49 ± 80.42 µm) and GCNP (intermediate values) are substantially larger than those reported for the 1:2 ChMA:GelMA hydrogel described by Saraiva et al. (2015), which exhibited an average pore size of ~2 µm and a compact, irregular structure. According to Saraiva et al., this morphology limits nutrient diffusion and cell infiltration, making such a network less favorable for regenerative applications requiring rapid vascularization and cell colonization. In contrast, the more open and interconnected structures observed in our NAC-containing formulations, particularly GCN, fall within the 100–350 µm range that identified as optimal for supporting bone tissue growth, vascularization, and efficient nutrient and waste transport.

This suggests that the structural differences between the two systems could have a major impact on their biological performance: while the compact, low-porosity network of the 1:2 ChMA:GelMA hydrogel may provide higher mechanical stability, it likely hinders cell infiltration; conversely, the larger pores of GCN and GCNP could facilitate early angiogenesis and osteogenic cell colonization, albeit potentially at the cost of reduced stiffness.

3.3 Mechanical Properties of the Hydrogels

We evaluated the mechanical performance of the hydrogels through uniaxial compression testing to obtain stress–strain curves and calculate Young's modulus (E), compressive strength (σF), and toughness (UT) (Figure 20). These properties are critical for determining the hydrogel's ability to withstand mechanical load and recover from deformation, which are essential features in tissue engineering applications involving structural support (Feng et al., 2016).

GC and GCP hydrogels exhibited low compressive strength and toughness, consistent with their dense and less porous morphology. This suggests that their compact architecture limits stress dissipation and elastic deformation.

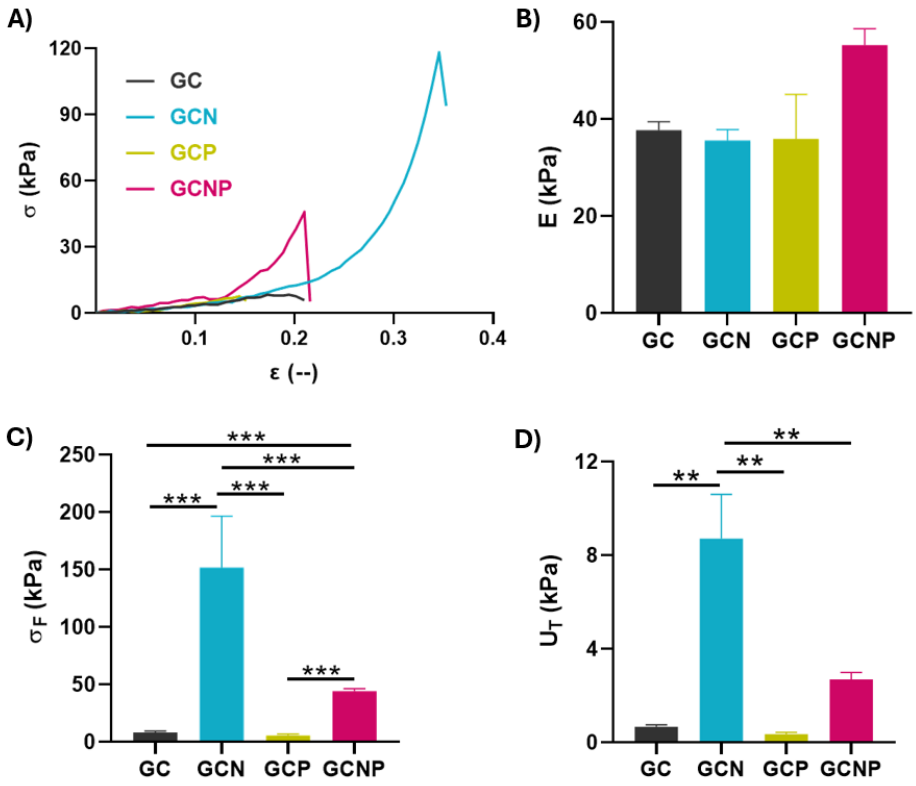

Figure 20. Mechanical properties of GC hydrogels functionalized with NAC and/or PAMP. (A) Representative stress–strain curves obtained from uniaxial compression of methacrylated gelatin and chitosan (GC) hydrogels, either unloaded (GC), or functionalized with N-acetylcysteine (GCN), pro-adrenomedullin (GCP), or both (GCNP). (B) Young's modulus (E) from the initial linear region. (C) Compressive strength at failure (σF). (D) Toughness (U_T), measured as energy absorbed before mechanical failure. GCN exhibited the highest σF and U_T, while GCNP showed the highest E value, suggesting distinct mechanical advantages depending on the formulation. Data are presented as mean ± SEM (n = 3). Statistical differences were analyzed using one-way ANOVA followed by Tukey's post hoc test. No significant differences were detected among groups in E ($p > 0.05$). In σF, GCN was significantly higher than GC, *GCP*, and GCNP (***, $p < 0.001$). GCNP was also significantly higher than GC and GCP (***, $p < 0.001$). In U_T, GCN was significantly higher than GC (**, $p = 0.002$), GCP (**, $p = 0.001$), and GCNP (**, $p = 0.009$).

GCNP hydrogels displayed the highest Young's modulus (55.26 ± 5.79 kPa), indicating increased stiffness and resistance to elastic deformation. This result may be associated with a more interconnected or reinforced matrix structure, potentially influenced by the simultaneous presence of both NAC and PAMP, although the precise structural basis was not directly measured. In contrast, GCN hydrogels exhibited the highest compressive strength and toughness values (44.31 kPa), meaning they could withstand greater forces before failure and absorb more energy during compression. This suggests that NAC incorporation enhances mechanical resilience.

Interestingly, while GCNP showed lower compressive strength than GCN, its higher stiffness may indicate a trade-off between rigidity and energy absorption. These differences likely reflect distinct internal architectures rather than compositional effects alone**.** Similar findings have been reported in other dual-network or functionalized hydrogels, where additive effects produce complex mechanical profiles (Luo et al., 2020).

The mechanical behavior observed correlates with the microstructural differences described in the previous section. Hydrogels with higher porosity and interconnected pore networks, such as GCN and GCNP, allow for better stress distribution and deformation resistance. These mechanical attributes are critical for bone tissue engineering applications, where mechanical loading and structural integrity are required.

When compared to the mechanical properties of native bone, GCNP hydrogels fall well below the values of trabecular bone (10–3000 MPa Young's modulus; 0.1–30 MPa compressive strength) and cortical bone (17–20 GPa Young's modulus; 115–205 MPa compressive strength) (Morgan et al., 2018). However, their stiffness and strength are consistent with hydrogel scaffolds designed for non-load-bearing bone defects, where compressive strengths of 10–1000 kPa are generally sufficient to maintain scaffold integrity and support tissue infiltration and regeneration (Yue et al., 2016; Chai et al., 2022). This suggests that, although GCNP and GCN are mechanically much softer than bone, they fall within the optimal mechanical range for scaffolds intended for craniofacial, calvarial, and other non-load-bearing bone defects.

A limitation of the current analysis is that crosslinking density and network homogeneity were not directly quantified. As such, interpretations about matrix organization remain inferential based on macroscopic mechanical outcomes and SEM observations.

From an application standpoint, the mechanical behavior of GCN and GCNP makes them promising candidates for bone tissue engineering, where resistance to compressive stress and moderate elasticity are essential. However, the low mechanical integrity of GC and GCP may restrict their use to non-load-bearing or softer tissue environments.

3.4 Biocompatibility of Hydrogels

We evaluated the biocompatibility of the hydrogel formulations using MC3T3-E1 preosteoblastic cells cultured for 1, 3, and 5 days (Figure 21). We assessed cell viability through MTT assay and further validated the results *ex vivo* using a critical-sized calvarial defect model. To examine the presence of viable tissue and cells surrounding the implanted hydrogels, we performed Live/Dead staining using a commercial viability kit (Figure 22).

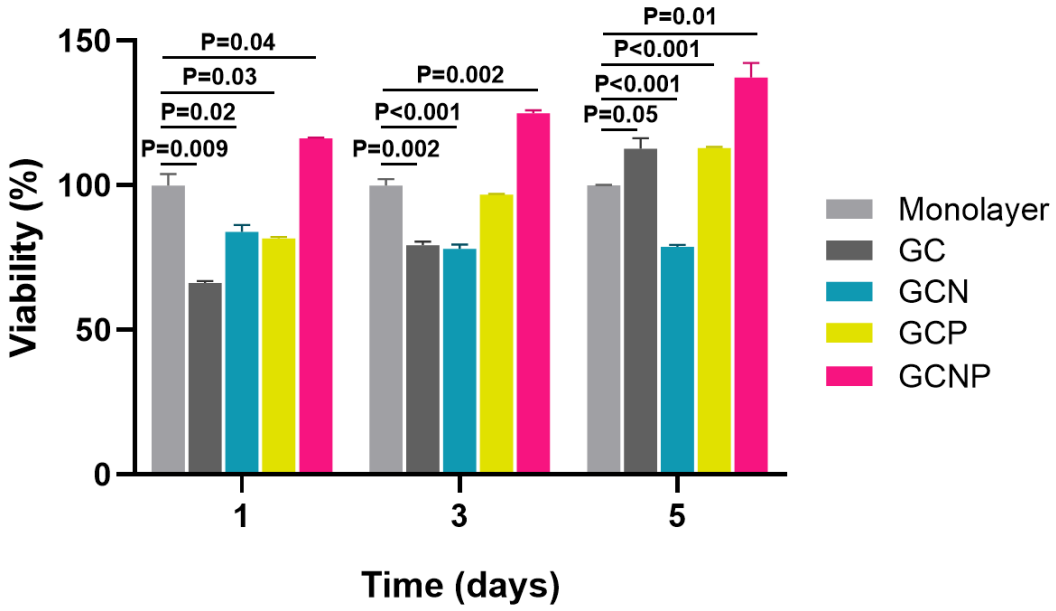

Figure 21. Viability of MC3T3-E1 cells in indirect culture with functionalized GC hydrogels. MTT assay results for preosteoblastic MC3T3-E1 cells cultured on the bottom of transwell systems exposed to unloaded (GC), NAC-loaded (GCN), PAMP-loaded (GCP), or dual-loaded (GCNP) methacrylated gelatin and chitosan hydrogels for 1, 3, and 5 days. The GCNP group showed significantly higher cell viability at all time points, exceeding the monolayer control group without hydrogel. In contrast, GC and GCN exhibited variable responses, while GCP showed a more stable but moderate effect. Data are presented as mean ± SD (n = 3). Statistical analysis was performed using two-way ANOVA with Dunnett's post hoc test, comparing all hydrogel conditions to the control at each time point. GCNP showed the most pronounced enhancement in viability, particularly in days 3 and 5. Exact *p* values are shown above bars and correspond to the following significance levels: $p < 0.05$ (*), $p < 0.01$ (**), and $p < 0.001$ (***).

At day 1, GCN and GCP hydrogels exhibited a slight decrease in metabolic activity compared to the monolayer control. This may reflect an early, transient cellular response to the chemical composition or mechanical properties of the hydrogel matrix. However, by day 3, the viability of cells in GCP had recovered to control levels, while GCN remained slightly lower. In contrast, GCNP hydrogels demonstrated a significant increase in metabolic activity across all time points, surpassing even the control condition.

These results suggest a synergistic effect between NAC and PAMP in supporting cell viability and potentially stimulating mitochondrial activity, although no direct mechanism was tested. This is consistent with previous reports where thiol antioxidants and peptide factors enhance preosteoblastic survival and proliferation (Lin et al.,2016).

It is important to note that the MTT assay reflects mitochondrial activity, which does not distinguish between increased cell number and increased metabolic rate per cell. Further cell counting or DNA quantification would help confirm proliferation.

To evaluate tissue integration and cellular viability in a more complex environment, an *ex vivo* assay was performed using mouse critical-sized calvarial defect model with injected hydrogels and stained with calcein-AM and Ethidium homodimer-1. All hydrogel groups demonstrated viable cells at the interface, with minimal red fluorescence, indicating low cytotoxicity (Figure 22). This supports the conclusion that none of the hydrogel formulations had a detrimental effect on cell survival in a tissue context.

Notably, the GCNP group exhibited a high cell density and strong green fluorescence signal, both at the interface and within the adjacent tissue. This suggests that GCNP promotes better cellular infiltration and matrix integration, which is essential for bone regeneration. This finding aligns with literature showing that pore interconnectivity and sustained bioactive release can facilitate cell migration into scaffolds and improve integration with host tissue (Karageorgiou and Kaplan, 2005).

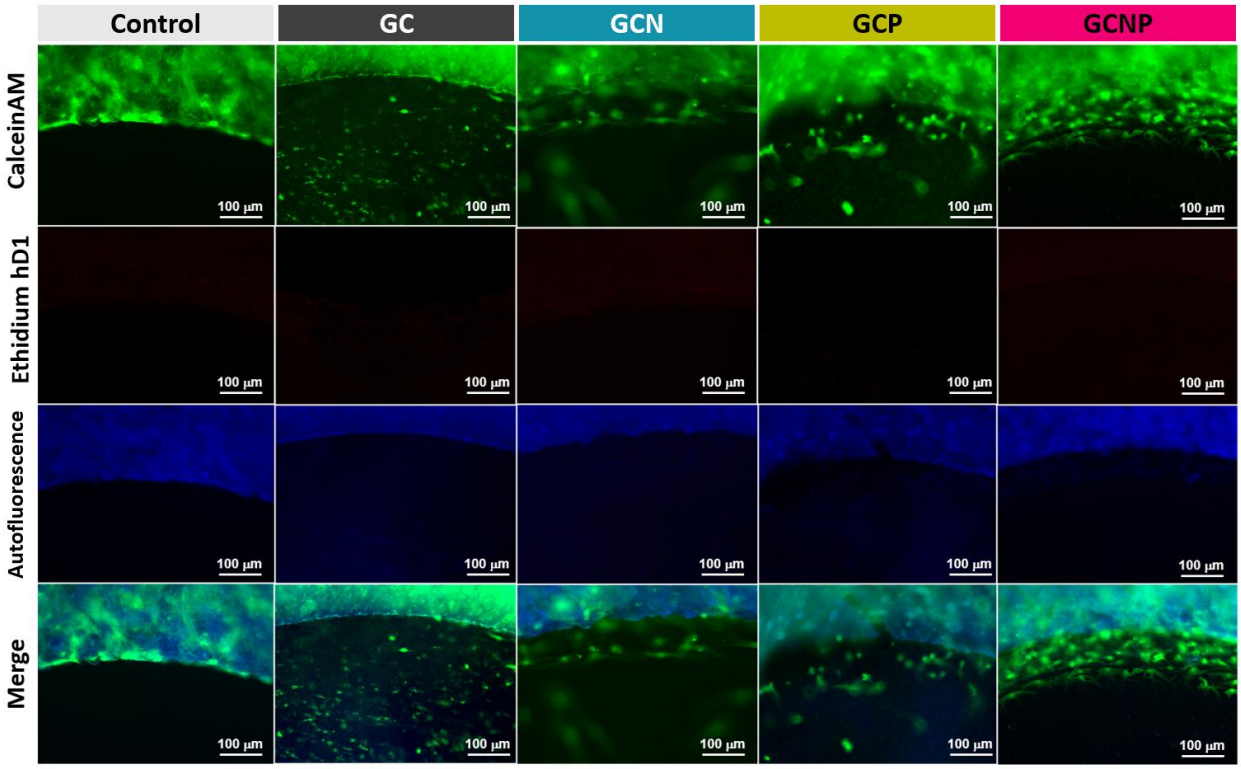

Figure 22. Evaluation of cell viability in *ex vivo* calvarial cultures with GC hydrogels. Fluorescence images after 14 days of *ex vivo* culture of mouse calvariae with unloaded (GC), NAC-loaded (GCN), PAMP-loaded (GCP), or dual-loaded (GCNP) hydrogels using the Live/Dead® assay. Calcein AM (green) indicates live cells, EthD-1 (red) marks membrane-compromised cells, and natural bone autofluorescence appears in blue. The GCNP condition showed higher densities of viable cells at the periphery of the defect compared to other groups, suggesting a more favorable environment for cell survival. Scale bar: 100 µm.

Additionally, the hydrogels have demonstrated biocompatibility with other cell types, including RAW 264.7 pre-osteoclasts (Appendix F, Figures 1F and 2F) and HMEC microvascular endothelial cells (Appendix G, Figure 1G), as well as in isolated aortic tissues, which remained viable after 11 days of culture (Appendix G, Figure 2G). The high viability observed in HMEC is particularly relevant for bone regeneration, as endothelial cells are key mediators of angiogenesis and vascular integration. Similar results have been reported in other hydrogel systems, such as starch-based matrices, where endothelial and osteoblast-like cells maintained high viability (>80%) over several days in culture (Flores-Arriaga et al., 2017). Sustaining endothelial viability within the scaffold microenvironment is crucial for initiating neovascularization, ensuring nutrient and oxygen delivery, and promoting long-term graft survival.

A limitation of the current study is that the *ex vivo* model does not fully capture immune or vascular responses that may occur *in vivo*. Additionally, functional outcomes such as osteogenic differentiation, vascular sprouting, or extracellular matrix deposition were not evaluated here and should be addressed in

future work. Nevertheless, the strong biocompatibility and cell-supportive behavior of GCNP highlights its potential as a scaffold for bone tissue engineering applications. Future studies should explore osteogenic differentiation and vascular integration *in vivo* to further validate these findings.

3.5 Osteogenic Potential: *In Vitro* and *Ex Vivo* Mineralization

We assessed the osteogenic activity of the GC-based hydrogels using both *in vitro* and *ex vivo* models over a 14-day period. *In vitro* assay aimed to evaluate mineral deposition and early osteogenic differentiation of MC3T3-E1 preosteoblastic cells cultured on the hydrogels. The *ex vivo* model, based on a critical-sized calvarial defect, was used to explore the osteoinductive potential of the materials within a more complex tissue environment. We employed Alizarin Red S (ARS) staining to assess calcium deposition and alkaline phosphatase (ALP) staining to examine early osteoblastic differentiation

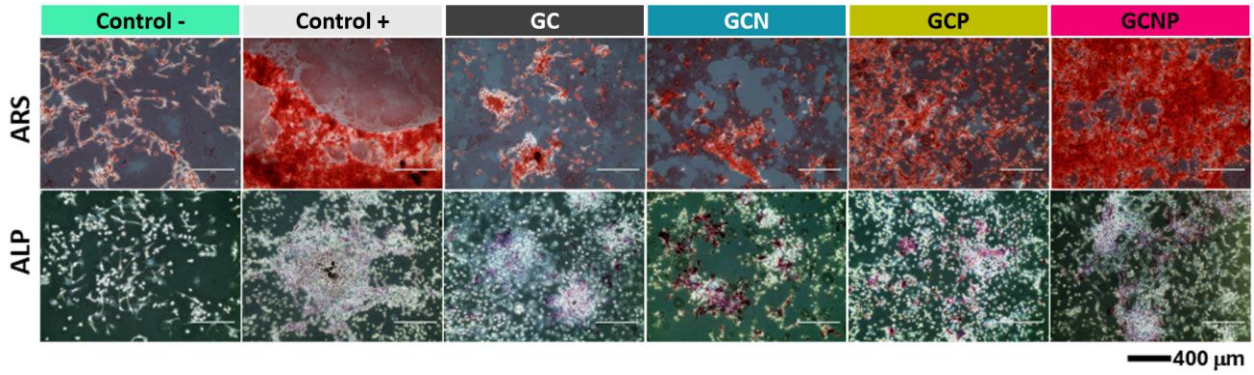

Figure 23. Osteogenic activity induced by GC hydrogels. Representative images of extracellular matrix mineralization by bone marrow-derived cells indirectly cultured with unloaded (GC), NAC-loaded (GCN), PAMP-loaded (GCP), or dual-loaded (GCNP) hydrogels. ARS staining (top row) marks calcium deposits (red), and ALP staining (bottom row) indicates enzymatic activity (purple). A positive osteogenic control and a negative control (growth medium only) were included. GCNP hydrogels showed staining intensity comparable to the positive control, suggesting a synergistic effect of NAC and PAMP in promoting osteoblastic differentiation. Scale bar: 400 µm.

In the *in vitro* model, bone marrow-derived cells cultured with GCNP hydrogels exhibited the most intense ARS and ALP staining (Figure 23). While ALP could not be quantified, ARS analysis revealed a significantly increased mineralized area ($1.75 \times 10^6 \pm 0.20 \times 10^6$ µm²) in the GCNP group, suggesting enhanced mineralization and osteogenic differentiation. GCN ($0.58 \times 10^6 \pm 0.11 \times 10^6$ µm²) and GCP ($0.89 \times 10^6 \pm 0.23 \times 10^6$ µm²) also induced mineral deposition, though to a lesser extent than GCNP. GC hydrogels showed limited mineralization ($0.18 \times 10^6 \pm 0.04 \times 10^6$ µm²), while the negative control ($0.47 \times 10^6 \pm$

0.14×10^6 µm²) displayed minimal staining. In contrast, the positive control ($0.89 \times 10^6 \pm 0.15 \times 10^6$ µm²) confirmed expected mineralization levels. Quantification of the ARS-stained area (Figure 24) supported these observations: GCNP-treated cells presented a significantly greater mineralized area than all other groups, including GCN and GCP.

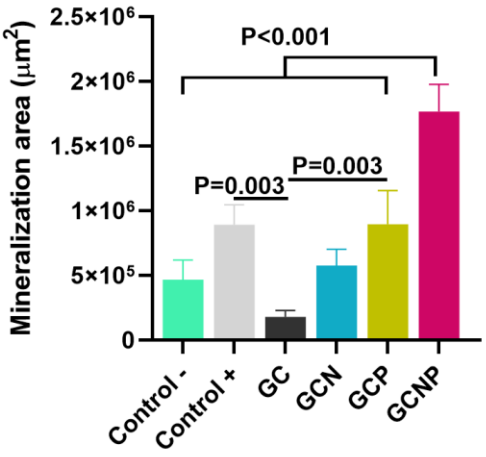

Figure 24. Quantification of mineralized area induced by GC hydrogels. ARS quantification of bone marrow-derived cells cultured with unloaded (GC), NAC-loaded (GCN), PAMP-loaded (GCP), or dual-loaded (GCNP) hydrogels, compared to positive and negative controls. GCNP induced the largest mineralized area, with statistically significant differences compared to all other groups (***, $p < 0.001$), highlighting the synergistic action of NAC and PAMP on osteogenic differentiation. In addition, GC also differed significantly from the positive control and GCP (**, $p = 0.003$). Data are presented as mean ± SD ($n = 3$). Statistical differences were analyzed using one-way ANOVA followed by Tukey's post hoc test.

When compared to previous reports, the mineralization area observed for GCNP in our *in vitro* model exceeds values typically reported for unmodified GelMA hydrogels, which often show limited ARS staining after 14 days of MC3T3-E1 culture (Liu et al., 2023). In that study, a GelMA/HAMA dual-network hydrogel without bioactive factors reached only ~0.45 absorbance units at 562 nm, whereas functionalization with osteogenic growth peptide (OGP) increased mineralization to ~0.65 absorbance units. Similarly, Ning et al. (2019) reported that GelMA hydrogels loaded with 100 ng/mL abaloparatide induced strong ARS staining after 14 days, comparable to our GCNP *in vitro* results and aligned with the pronounced staining seen in our *ex vivo* calvarial defect model. These comparisons suggest that the dual functionalization with NAC and PAMP in GCNP achieves mineralization outcomes comparable to or exceeding those of other peptide-functionalized GelMA systems, while preserving injectability and tunable degradation profiles advantageous for clinical translation.

To evaluate the osteogenic potential of hydrogels an *ex vivo* model of calvarial defect was used. After 14 days of culture with hydrogels placed in the defect site, ARS staining revealed strong calcium deposition in calvariae treated with GCNP (Figure 25), as well as notable ALP staining (Figure 26), comparable to the osteogenic control. GCN and GC induced moderate mineralization, while the negative control remained unstained. However, due to the lack of quantitative analysis and differences in the visible tissue area among images, these results should be interpreted qualitatively. The images were acquired under identical magnification, but the heterogeneity of tissue coverage limited direct comparison.

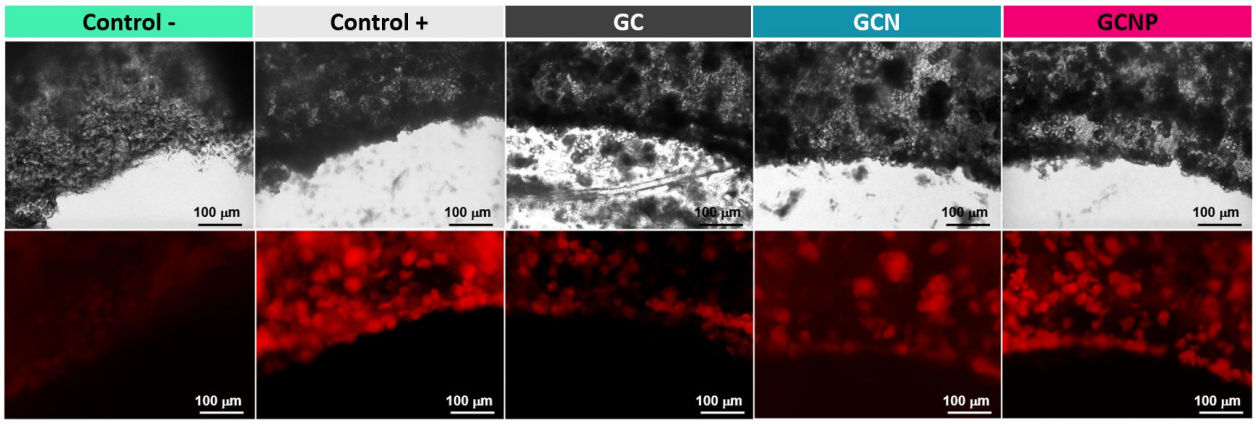

Figure 25. *Ex vivo* mineralization in a critical-sized calvarial defect model. Brightfield (top) and fluorescence (bottom) images of mouse calvariae cultured *ex vivo* for 14 days in osteogenic medium with GC, GCN, or GCNP hydrogels placed within the defect. Alizarin Red S staining reveals red fluorescent signal indicating calcium deposition. GCNP showed the most intense and widespread signal, indicating superior mineralized matrix formation. Osteogenic control also showed strong mineralization, while the negative control and GC displayed minimal signals. Scale bar: 100 µm.

The pronounced ALP activity in GCNP-treated samples is particularly relevant, as ALP is a key early marker of osteoblastic differentiation and is linked to the initiation of matrix mineralization. This observation aligns with previous studies in GelMA–ChMA composite hydrogels where increased ALP correlated with higher mineral deposition and expression of osteogenic genes When compared to previous reports, the mineralization area observed for GCNP in our *in vitro* model exceeds values typically reported for unmodified GelMA hydrogels, which often show limited ARS staining after 14 days of MC3T3-E1 culture (Liu et al., 2023). In that study, a GelMA/HAMA dual-network hydrogel without bioactive factors reached only ~0.45 absorbance units at 562 nm, whereas functionalization with osteogenic growth peptide (OGP) increased mineralization to ~0.65 absorbance units. Similarly, Ning et al. (2019) reported that GelMA hydrogels loaded with 100 ng/mL abaloparatide induced strong ARS staining after 14 days, comparable to our GCNP *in vitro* results and aligned with the pronounced staining seen in our *ex vivo* calvarial defect model. These comparisons suggest that the dual functionalization with NAC and PAMP in GCNP achieves

mineralization outcomes comparable to or exceeding those of other peptide-functionalized GelMA systems, while preserving injectability and tunable degradation profiles advantageous for clinical translation.

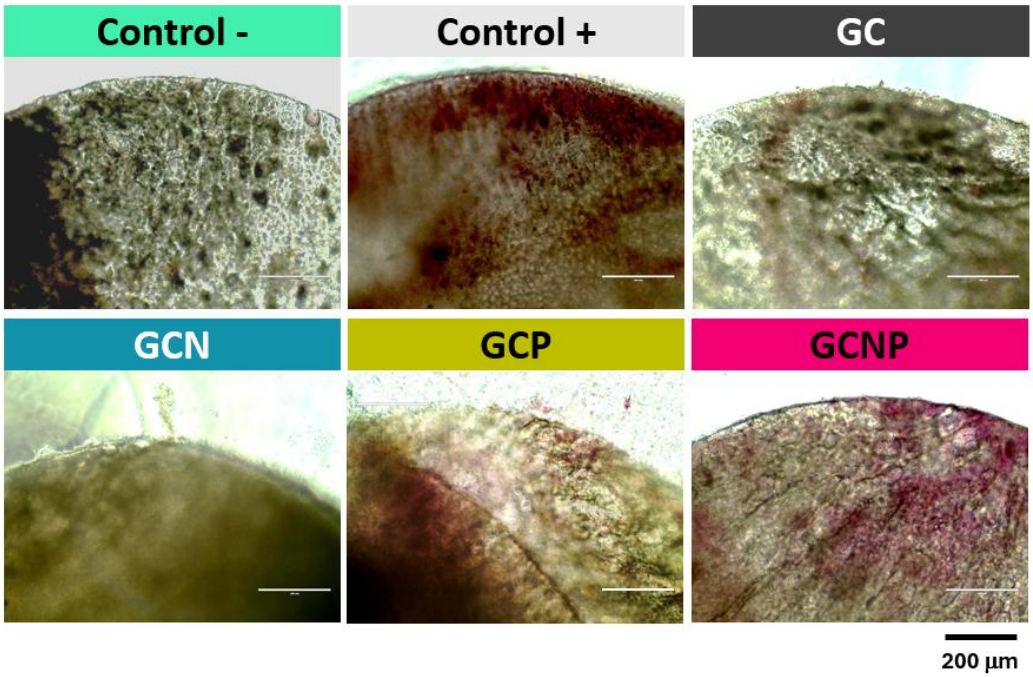

Figure 26. Alkaline phosphatase (ALP) activity in *ex vivo* calvarial cultures. Representative images of mouse calvariae after 14 days of *ex vivo* culture in direct contact with unloaded (GC), NAC-loaded (GCN), PAMP-loaded (GCP), or dual-loaded (GCNP) hydrogels. Tissues were stained to detect ALP, an early marker of osteoblastic differentiation. Controls included growth medium (negative) and osteogenic medium (positive). GCNP displayed the most intense ALP staining, similar to the positive control, indicating strong osteogenic activation in the bone tissue in contact with this hydrogel. Scale bar: 200 µm.

Nonetheless, the combined evidence of increased cell viability and enhanced mineralization supports the potential of GCNP hydrogels to promote osteogenic responses. Future studies should confirm early-stage differentiation through quantitative ALP assays, osteogenic gene expression, and signaling pathway activation, as well as assess long-term bone formation *in vivo* using micro-CT and histological analysis. This will allow a complete characterization of the mechanisms and therapeutic potential of this system.

3.6 Integrated Discussion of Findings

The development of biomaterials for bone tissue engineering must balance structural, mechanical, and biological properties to effectively mimic the bone environment and promote regeneration. In this study,

a dual-crosslinked hydrogel system composed of methacrylated gelatin and chitosan (GC) was functionalized with N-acetylcysteine (NAC) and pro-adrenomedullin peptide (PAMP) to assess its potential to support bone remodeling.

Pore size significantly influences cell infiltration, nutrient diffusion, and tissue integration. Our SEM analysis showed a mean pore diameter of 24.49 ± 14.19 µm for GC, which increased significantly in GCN (200.49 ± 80.42 µm) and GCNP (212.84 ± 72.33 µm), likely due to the hydrophilic properties of NAC. These values fall within the favorable range of 100–350 µm known to promote bone and vascular tissue ingrowth (Mukasheva et al., 2024). For comparison, Zhao et al. (2025) reported a pore size of ~74.6 ± 4.1 µm in GelMA hydrogels loaded with adrenomedullin (ADM), and Osi et al. (2021) achieved similar increases using hydroxyapatite in ChMAGelMA blends. This suggests that our GCNP formulation not only supports structural openness but also exceeds the minimal threshold required for effective osteogenesis.

Swelling behavior also impacts nutrient transport and drug diffusion. GCNP reached a plateau swelling ratio of 1.24 ± 0.03 after 24 h, indicating a 24% increase in mass. While lower than values reported in highly hydrophilic systems such as ADM@GelMA (18.5, Zhao et al., 2025), this modest swelling suggests structural stability and lower risk of volumetric changes in vivo. Notably, our swelling ratio is also lower than chitosan–GelMA systems with mineral additives (Osi et al., 2021; Wang et al., 2024), supporting its use in confined defects. Xu et al. (2021) reported similar swelling values (~1.25) in thiolated hyaluronic acid hydrogels. These differences may result from the higher hydrophilicity of hyaluronic acid and GelMA compared to chitosan, which in our system likely limits water retention but maintains structural integrity.

Degradation kinetics are critical to match the timeline of tissue formation. GCNP exhibited rapid degradation—87.14 ± 4.29% in macrophage-conditioned medium and 97.53 ± 4.23% with lysozyme over 14 days. This timeframe overlaps with the peak bioactive release (86.60 ± 6.00% NAC release in 7 days), suggesting a synchronized degradation-release profile. Compared to other systems (Zhao et al., ~65% degradation; Wang et al., ~55%), GCNP degrades faster, which may be suitable for non-load-bearing applications where scaffold clearance is desirable to allow tissue replacement (Yue et al., 2016).

The GCNP hydrogel released 86.60 ± 6.00% of NAC within 7 days under physiological conditions. This release is comparable to the study by Shen et al. (2024), where 86% of NAC was released from GelMA scaffolds within 8 days. The similarity in release kinetics, despite differences in matrix composition, underscores the reproducibility of sustained NAC delivery in hydrogel systems.

In terms of mechanical performance, GCNP reached a compressive strength of 206.63 ± 11.52 kPa and a Young's modulus of 55.26 ± 5.79 kPa, which is consistent with values reported for other composite hydrogels. For example, Osi et al. (2021) reported a compressive strength of approximately 200 kPa and Young's modulus near 50 kPa for chitosan–GelMA–HAp hydrogels, while Wang et al. (2024) showed values ranging from ~150 to 250 kPa in PDA-coated HAp-reinforced systems. In contrast, Zhao et al. (2025) reported a much lower compressive strength of 23.9 ± 1.2 kPa for ADM@GelMA, reflecting the absence of inorganic reinforcement. These results position GCNP within the desirable mechanical range for non-load-bearing craniofacial bone defects, where compressive strengths between 10–1000 kPa are generally sufficient to preserve scaffold integrity and allow tissue infiltration (Yue et al., 2016; Chai et al., 2022).

Regarding cell viability, GCNP significantly enhanced MC3T3-E1 survival compared to both the 2D monoculture and other hydrogel groups (GC, GCN, GCP), with $p < 0.001$ at all timepoints. In a comparable system, Lin et al. (2016) observed a ~20–25% increase in MG63 cell viability when NAC was incorporated into GelMA hydrogels. Zhao et al. (2025) also reported enhanced viability in DPSCs and MC3T3 cells cultured with ADM@GelMA, though fold values were not explicitly provided. While these studies used different cell types and formulations, the consistent trend underscores the cytoprotective effect of NAC and ADM. Our results suggest that their combination within a dual-crosslinked matrix may synergistically enhance cell survival.

Mineralization assays further demonstrated that GCNP induced a two-fold increase in mineralized area compared to the positive control, as assessed by ARS staining. This performance is comparable to that of ADM@GelMA hydrogels, which achieved a 2.67-fold increase over untreated controls (Zhao et al., 2025). Wang et al. (2024) reported a ~2–3× increase in osteogenic mineralization with ceramic-PDA composites. Despite lacking inorganic components, GCNP elicited mineralization levels like or exceeding those of ceramic-containing scaffolds, highlighting the potency of sustained dual-drug delivery in promoting osteogenic differentiation.

Table 3. Comparative performance of GCNP versus reported hydrogel systems for bone regeneration

Parameter	GCNP (This Work)	ChMA-GelMA-HAp (Osi et al., 2021)	PDA-HAp/GelMA (Wang et al., 2024)	ADM@GelMA (Zhao et al., 2025)
Pore Size (μm)	212.84 ± 72.33	~170	Not reported	74.6 ± 4.1
Swelling Ratio (24h)	1.24 ± 0.03	~2.1–2.4	~2.5–2.8	~18.5
% Degradation (14d)	97.5% (lysozyme) / 87.1% (macrophages)	~30–60% (collagenase)	~55%	~65% (collagenase)
Compressive Strength (kPa)	206.6 ± 11.5	~150–200 (with HAp)	~150–250	~23.9 ± 1.2
Young's Modulus (kPa)	55.3 ± 5.8	~50	Not reported	Not reported
Drug Release (% NAC)	86.6% in 7 days	Not reported	Not applicable	85% (ADM, 14d)
Cell Viability	↑ MC3T3 vs. control ($p<0.001$)	↑ in MC3T3 and MG63	↑ MC3T3 and RAW264.7	↑ DPSCs, MC3T3
Mineralization	~2× vs. control	↑ (qualitative)	~2–3× vs. control	2.67× vs. control

Overall, GCNP demonstrates performance that is competitive with current hydrogel systems, with its main advantages lying in the simplicity of composition, dual bioactive loading, and favorable balance between degradation rate, mechanical properties, and bioactivity. Limitations include the absence of inorganic reinforcements and gene-level validation of osteogenic markers, which should be addressed in future studies. Nonetheless, these results support the continued development of GCNP for non-load-bearing bone repair applications where injectable delivery, rapid bioactive release, and early-stage matrix mineralization are desired.

Chapter 4. Conclusions

This research aimed to evaluate the osteogenic potential of injectable hydrogels composed of methacrylated gelatin and chitosan, incorporating N-acetylcysteine (NAC) and pro-adrenomedullin peptide (PAMP). The hypothesis proposed that this dual-loaded system would support bone mineralization by improving both the physicochemical properties and biological performance of the hydrogels.

The results confirmed this hypothesis. GCNP hydrogels—loaded with both NAC and PAMP—exhibited favorable physicochemical properties, including high swelling capacity, tunable degradation, and improved porosity and mechanical strength. These characteristics were largely driven by NAC network-modifying effects and PAMP stabilizing contribution. In the presence of lysozyme, GCNP lost 97.53 ± 4.23 % of its mass after 14 days, and under co-culture with RAW 264.7 macrophages, degradation reached 87.14 ± 4.29 % after 7 days. The release profile showed a biphasic behavior, with 86.60 ± 6.00 % of total compound released by day 7. SEM analysis confirmed that NAC incorporation significantly increased pore size, from 24.49 ± 14.19 µm (GC) to 200.49 ± 80.42 µm (GCN). Mechanically, GCN showed the highest compressive strength (151.79 ± 44.81 kPa), while GCNP exhibited the highest Young's modulus (55.26 ± 5.79 kPa), indicating improved mechanical performance.

In terms of biological performance, GCNP hydrogels demonstrated the highest cell viability *in vitro* as determined by MTT assay at days 1, 3, and 7. *Ex vivo* analysis using a critical-sized calvarial defect model further confirmed enhanced cellular infiltration and proliferation in the surrounding tissue after 14 days, as shown by Live/Dead staining. Alizarin Red S staining revealed that GCNP doubled the mineralized area compared to the control group *in vitro*, and mineral deposition was also evident *ex vivo* through fluorescence analysis. These findings fulfill the objectives of this study by demonstrating that the hydrogels were successfully synthesized, characterized, and exhibited superior bioactivity in both *in vitro* and *ex vivo* models.

One key contribution of this work is the demonstration that simple co-loading of NAC and PAMP, without complex chemical conjugation, can achieve synergistic effects on bone cell behavior and matrix mineralization. This makes GCNP hydrogels a promising scaffold candidate for bone tissue engineering.

However, limitations must be acknowledged. The signaling pathways and molecular mechanisms by which NAC and PAMP exert their effects were not examined, and immune or vascular responses could not be

assessed using the *in vitro* and *ex vivo* models employed. Moreover, long-term performance and integration under dynamic physiological conditions remain to be explored.

Future studies should include *in vivo* assessments in orthotopic bone defects, evaluation of osteogenic signaling pathways, and investigation of vascularization and immune modulation. Optimizing release kinetics and long-term degradation may further enhance scaffold performance.

In summary, this study demonstrates that injectable GCNP hydrogels provide a potential structurally and biologically functional platform for bone regeneration. Their dual bioactivity, ease of synthesis, and favorable interaction with bone-forming cells support their continued development for regenerative applications.

Bibliography

Alizadeh-Osgouei, M., Li, Y., & Wen, C. (2019). A comprehensive review of biodegradable synthetic polymer-ceramic composites and their manufacture for biomedical applications. *Bioactive Materials*, *4*(1), 22–36. doi: 10.1016/j.bioactmat.2018.11.003

Amend, S. R., Valkenburg, K. C., & Pienta, K. J. (2016). Murine Hind Limb Long Bone Dissection and Bone Marrow Isolation. *Journal of Visualized Experiments: JoVE. Journal of Visualized Experiments, 110*(e53936), 1-4. doi: 10.3791/53936

Anada, T., Pan, C. C., Stahl, A. M., Mori, S., Fukuda, J., Suzuki, O., & Yang, Y. (2019). Vascularized bone-mimetic hydrogel constructs by 3D bioprinting to promote osteogenesis and angiogenesis. *International Journal of Molecular Sciences, 20*(1096), 1-14. doi: 10.3390/ijms20051096

Andrade, D. B., Soares, L. L. S., Cardoso, F. L. A., Lima, I. S., Silva, J. G. V., Carvalho, M. A. M., Fonseca, M. G., Brito, G. de C., Santos, F. E. P., Osajima, J. A., Lobo, A. O., & Silva-Filho, E. C. (2023). Hydrogel Based on Nanoclay and Gelatin Methacrylate Polymeric Matrix as a Potential Osteogenic Application. *Journal of Functional Biomaterials, 14*(74), 1-14. doi: 10.3390/jfb14020074

Araiza-Verduzco, F., Rodríguez-Velázquez, E., Cruz, H., Rivero, I. A., Acosta-Martínez, D. R., Pina-Luis, G., & Alatorre-Meda, M. (2020). Photocrosslinked Alginate-Methacrylate Hydrogels with Modulable Mechanical Properties: Effect of the Molecular Conformation and Electron Density of the Methacrylate Reactive Group. *Materials*, *13*(534), 1-14. doi: 10.3390/ma13030534

Barros, J., Ferraz, M. P., Azeredo, J., Fernandes, M. H., Gomes, P. S., & Monteiro, F. J. (2019). Alginate-nanohydroxyapatite hydrogel system: Optimizing the formulation for enhanced bone regeneration. *Materials Science and Engineering C*, *105*(109985), 1–14. doi.org/10.1016/j.msec.2019.109985

Barry Carter, C. & Grant Norton, M. (2007). Ceramic materials: Science and engineering. *Springer*. doi: 10.1007/978-0-387-46271-4

Céspedes-Valenzuela, D. N., Sánchez-Rentería, S., Cifuentes, J., Gantiva-diaz, M., Serna, J. A., Reyes, L. H., Ostos, C., Cifuentes-De la Portilla, Christian Muñoz-Camargo, C., & Cruz, J. C. (2021). Preparation and Characterization of an Injectable and Photo-Responsive Chitosan Methacrylate/Graphene Oxide Hydrogel: Potential Applications in Bone Tissue Adhesion and Repair. *Polymers*, *14*(126), 1-24. doi.org/10.3390/polym14010126

Chai, S., Huang, J., Mahmut, A., Wang, B., & Yao, Y. (2022). Injectable Photo-Crosslinked Bioactive BMSCs-BMP2-GelMA Scaffolds for Bone Defect Repair. *Frontiers in Bioengineering and Biotechnology*, *10*(875363), 1-13. doi: 10.3389/fbioe.2022.875363

Chaudhuri, O., Gu, L., Darnell, M., Klumpers, D., Bencherif, S. A., Weaver, J. C., Huebsch, N., & Mooney, D. J. (2015). Substrate stress relaxation regulates cell spreading. Nature Communications. *Nature Publishing Group*, *6*(6364), 1–7. doi: 10.1038/ncomms7365

Chichiricco, P. M., Matricardi, P., Colaço, B., Gomes, P., Jérôme, C., Lesoeur, J., Veziers, J., Réthoré, G., Weiss, P., Struillou, X., & Le Visage, C. (2023). Injectable Hydrogel Membrane for Guided Bone Regeneration. *Bioengineering*, *10*(1), 1–23. doi: 10.3390/bioengineering10010094

Cornish, J., Callon, K. E., Bava, U., Coy, D. H., Mulvey, T. B., Murray, M. A. F., Cooper, G. J. S., & Reid, I. R. (2001). Systemic administration of adrenomedullin(27-52) increases bone volume and strength in male mice. *Journal of Endocrinology*, *170*(1), 251–257. doi: 10.1677/joe.0.1700251

Cornish, J., Callon, K. E., Coy, D. H., Jiang, N. Y., Xiao, L., Cooper, G. J. S., & Reid, I. R. (1997). Adrenomedullin is a potent stimulator of osteoblastic activity in vitro and in vivo. *American Journal of Physiology - Endocrinology and Metabolism*, *273*, 1113–1120. doi: 10.1152/ajpendo.1997.273.6.e1113

Cota Quintero, J. L., Ramos-Payán, R., Romero-Quintana, J. G., Ayala-Ham, A., Bermúdez, M., & Aguilar-Medina, E. M. (2025). Hydrogel-Based Scaffolds: Advancing Bone Regeneration Through Tissue Engineering. *Gels*, *11*(3), 1–38. doi: 10.3390/gels11030175

Dec, P., Modrzejewski, A., & Pawlik, A. (2023). Existing and Novel Biomaterials for Bone Tissue Engineering. *International Journal of Molecular Sciences*, *24*(529), 1-14. doi: 10.3390/ijms24010529

Domazetovic, V., Marcucci, G., Iantomasi, T., Brandi, M. L., & Vincenzini, M. T. (2017). Oxidative stress in bone remodeling: Role of antioxidants. *Clinical Cases in Mineral and Bone Metabolism*, *14*(2), 209–216. doi:10.11138/ccmbm/2017.14.1.209

Einhorn, T. A. & Gerstenfeld, L. C. (2015). Fracture healing: Mechanisms and interventions. *Nature Reviews Rheumatology*, *11*(1), 45–54. doi: 10.1038/nrrheum.2014.164

Feher, B., Ali, K., Alccayhuaman, A., Strauss, F. J., Lee, J., Tangl, S., Kuchler, U., & Gruber, R. (2021). Osteoconductive properties of upside- down bilayer collagen membranes in rat calvarial defects. *International Journal of Implant Dentistry*, *7*(50), 1-10. doi: 10.1186/s40729-021-00333-y

Feng, Q., Wei, K., Lin, S., Xu, Z., Sun, Y., Shi, P., Li, G., & Bian, L. (2016). Mechanically resilient, injectable, and bioadhesive supramolecular gelatin hydrogels crosslinked by weak host-guest interactions assist cell infiltration and in situ tissue regeneration. *Biomaterials*, *101*, 217–228. doi: 10.1016/j.biomaterials.2016.05.043

Feng, Q., Xu, J., Zhang, K., Yao, H., Zheng, N., Zheng, L., Wang, J., Wei, K., Xiao, X., Qin, L., & Bian, L. (2019a). Dynamic and Cell-Infiltratable Hydrogels as Injectable Carrier of Therapeutic Cells and Drugs for Treating Challenging Bone Defects. *ACS Central Science*, *5*(3), 440–450. doi: 10.1021/acscentsci.8b00764

Fillingham, Y. & Jacobs, J. (2016). Bone grafts and bone substitutes. *The Bone & Joint Journal*, *98-B*(1 Suppl A), 6–9. doi: 10.1302/0301-620X.98B.36350

Fonseca, D. F. S., Costa, P. C., Almeida, I. F., Dias-Pereira, P., Correia-Sá, I., Bastos, V., Oliveira, H., Vilela, C., Silvestre, A. J. D., & Freire, C. S. R. (2020). Swellable Gelatin Methacryloyl Microneedles for Extraction of Interstitial Skin Fluid toward Minimally Invasive Monitoring of Urea. *Macromolecular Bioscience*, *20*(2000195), 1-11. doi: 10.1002/mabi.202000195

Fontani, F., Marcucci, G., Iantomasi, T., Brandi, M. L., & Vincenzini, M. T. (2015). Glutathione, N-acetylcysteine and Lipoic Acid Down-Regulate Starvation-Induced Apoptosis, RANKL/OPG Ratio and Sclerostin in Osteocytes: Involvement of JNK and ERK1/2 Signalling. *Calcified Tissue International*, *96*, 335-346. doi: 10.1007/s00223-015-9961-0

Friedman, M. (2004). Applications of the Ninhydrin Reaction for Analysis of Amino Acids, Peptides, and Proteins to Agricultural and Biomedical Sciences. *Journal of Agricultural and Food Chemistry*, *52*(3), 385–406. doi: 10.1021/jf030490p

Fuchs, R. K., Warden, S. J., & Turner, C. H. (2009). Bone anatomy, physiology and adaptation to mechanical loading. In Bone Repair Biomaterials. *Bone Repair Bioomaterials*, *2*, 25-68. doi: 10.1533/9781845696610.1.25

García-García, P., Reyes, R., Segredo-Morales, E., Pérez-Herrero, E., Delgado, A., & Évora, C. (2019). PLGA-BMP-2 and PLA-17β-estradiol microspheres reinforcing a composite hydrogel for bone regeneration in osteoporosis. *Pharmaceutics*, *11*(12), 1–19. doi: 10.3390/pharmaceutics11120648

García-Honduvilla, N., Cifuentes, A., Bellón, J. M., Buján, J., & Martínez, A. (2013). The angiogenesis promoter, proadrenomedullin nterminal 20 peptide (PAMP), improves healing in both normoxic and ischemic wounds either alone or in combination with autologous stem/progenitor cells. *Histology and Histopathology*, *28*(1), 115–125. doi: 10.14670/HH-28.115

Ghandforoushan, P., Alehosseini, M., Golafshan, N., Castilho, M., Dolatshahi-Pirouz, A., Hanaee, J., Davaran, S., & Orive, G. (2023). Injectable hydrogels for cartilage and bone tissue regeneration: A review. *International Journal of Biological Macromolecules*, *246*(125674), 1-28. doi: 10.1016/j.ijbiomac.2023.125674

Ghosh, M., Halperin-Sternfeld, M., Grinberg, I., & Adler-Abramovich, L. (2019). Injectable alginate-peptide composite Hydrogel as a scaffold for bone tissue regeneration. *Nanomaterials*, *9*(497), 1-15. doi:10.3390/nano9040497

Gilarska, A., Hinz, A., Bzowska, M., Dyduch, G., Kamiński, K., Nowakowska, M., & Lewandowska-Łańcucka, J. (2021). Addressing the Osteoporosis Problem-Multifunctional Injectable Hybrid Materials for Controlling Local Bone Tissue Remodeling. *ACS Applied Materials and Interfaces*, *13*(42), 49762–49779. doi: 10.1021/acsami.1c17472

Gomez-Aparicio, L. S., Bernáldez-Sarabia, J., Camacho-Villegas, T. A., Lugo-Fabres, P. H., Díaz-Martínez, N. E., Padilla-Camberos, E., Licea-Navarro, A., & Castro-Ceseña, A. B. (2020). Improvement of the wound healing properties of hydrogels with N -acetylcysteine through their modification with methacrylate-containing polymers. *Biomaterials Science*, *9*, 726–744. doi: 10.1039/d0bm01479f

Gothard, D., Smith, E. L., Kanczler, J. M., Black, C. R., Wells, J. A., Roberts, C. A., White, L. J., Qutachi, O., Peto, H., Rashidi, H., Rojo, L., Stevens, M. M., El Haj, A. J., Rose, F. A. R. J., Shakesheff, K. M., & Oreffo, R. O. C. (2015). In vivo assessment of bone regeneration in alginate/bone ECM hydrogels with incorporated skeletal stem cells and single growth factors. *PLoS ONE*, *10*(12), 1–23. doi: 10.1371/journal.pone.0145080

Guindani, C., Candiotto, G., Araújo, P. H. H., Ferreira, S. R. S., de Oliveira, D., Wurm, F. R., & Landfester, K. (2020). Controlling the biodegradation rates of poly(globalide-co-ε-caprolactone) copolymers by post polymerization modification. *Polymer Degradation and Stability*, *179*(109287), 1-14. doi: 10.1016/J.POLYMDEGRADSTAB.2020.109287

Han, F., Yang, X., Zhao, J., Zhao, Y., & Yuan, X. (2015). Photocrosslinked layered gelatin-chitosan hydrogel with graded compositions for osteochondral defect repair. *Journal of Materials Science: Materials in Medicine*, *26*(4), 1-13. doi: 10.1007/s10856-015-5489-0

Hollister, S. J. (2005). Porous scaffold design for tissue engineering. *Nature Materials*, *4*(7), 518–524. doi: 10.1038/NMAT1421

Hutchings, G., Moncrieff, L., Dompe, C., Janowicz, K., Sibiak, R., Bryja, A., Jankowski, M., Mozdziak, P., Bukowska, D., Antosik, P., Shibli, J. A., Dyszkiewicz-Konwińska, M., Bruska, M., Kempisty, B., & Piotrowska-Kempisty, H. (2020). Bone Regeneration, Reconstruction and Use of Osteogenic Cells; from Basic Knowledge, Animal Models to Clinical Trials. *Journal of Clinical Medicine*, *9*(139), 1–27. doi:10.3390/jcm9010139

Jabbari, E. (2019). Challenges for natural hydrogels in tissue engineering. *Gels*, *5*(30), 1-9. doi: 10.3390/gels5020030

Jang, H. J. & Yoon, J. K. (2024). The Role of Vasculature and Angiogenic Strategies in Bone Regeneration. Biomimetics, 9(75), 1-19. doi: 10.3390/biomimetics9020075

Jasmine, S. & Krishnamoorthy, R. (2022). Biodegradable Materials for Bone Defect Repair. Biodegradable Materials and Their Applications. *Military Medical Research*, *7*(54), 457–470. doi: 10.1002/9781119905301.ch16

Ji, Y., Wang, L., Watts, D. C., Qiu, H., You, T., Deng, F., & Wu, X. (2014). Controlled-release naringin nanoscaffold for osteoporotic bone healing. Dental Materials. *The Academy of Dental Materials*, *30*(11), 1263–1273. doi: 10.1016/j.dental.2014.08.381

Joshi, P., Ahmed, M. S. U., Vig, K., Vega Erramuspe, I. B., & Auad, M. L. (2021). Synthesis and characterization of chemically crosslinked gelatin and chitosan to produce hydrogels for biomedical applications. *Polymers for Advanced Technologies*, *32*(5), 2229–2239. doi: 10.1002/pat.5257

Karageorgiou, V. & Kaplan, D. (2005). Porosity of 3D biomaterial scaffolds and osteogenesis. *Biomaterials*, *26*(27), 5474–5491. doi: 10.1016/j.biomaterials.2005.02.002

Kashirina, A., Yao, Y., Liu, Y., & Leng, J. (2019). Biopolymers as bone substitutes: A review. *Biomaterials Science*, *7*(10), 3961–3983. doi: 10.1039/c9bm00664h

Kim, H., Kim, K., Kim, B., Lee, K., & Lee, S. (2019). N-acetyl-l-cysteine controls osteoclastogenesis through regulating Th17 differentiation and RANKL in rheumatoid arthritis. *Korean Journal Intern Medicine*, *34*, 210–219. doi: 10.3904/kjim.2016.329

Kim, M. H., Kim, B. S., Park, H., Lee, J., & Park, W. H. (2018). Injectable methylcellulose hydrogel containing calcium phosphate nanoparticles for bone regeneration. *International Journal of Biological Macromolecules*, *109*, 57–64. doi: 10.1016/j.ijbiomac.2017.12.068

Kocak, F. Z., Talari, A. C. S., Yar, M., & Rehman, I. U. (2020). In-Situ Forming pH and Thermosensitive Injectable Hydrogels to Stimulate Angiogenesis: Potential Candidates for Fast Bone Regeneration Applications. *International Journal of Molecular Sciences*, *21*(1633), 1–26. doi:10.3390/ijms21051633

Kukita, T., Hiura, H., Gu, J. Y., Zhang, J. Q., Kyumoto-Nakamura, Y., Uehara, N., Murata, S., Sonoda, S., Yamaza, T., Takahashi, I., & Kukita, A. (2021). Modulation of osteoclastogenesis through adrenomedullin receptors on osteoclast precursors: initiation of differentiation by asymmetric cell division. *Laboratory Investigation*, *101*(11), 1449–1457. doi: 10.1038/s41374-021-00633-2

Kumar, P., Nagarajan, A., & Uchil, P. D. (2018). Analysis of cell viability by the MTT assay. *Cold Spring Harbor Protocols*, *2018*(6), 469–471. doi: 10.1101/pdb.prot095505

Kwon, W. & Jeong, E. (2020). Detoxification properties of guanidinylated chitosan against chemical warfare agents and its application to military protective clothing. *Polymers*, *12*(1461), 1-12. doi: 10.3390/polym12071461

Lavanya, K., Chandran, S. V., Balagangadharan, K., & Selvamurugan, N. (2020). Temperature- and pH-responsive chitosan-based injectable hydrogels for bone tissue engineering. *Materials Science and Engineering C*, *111*(110862), 1-12. doi: 10.1016/j.msec.2020.110862

Leena, R. S., Vairamani, M., & Selvamurugan, N. (2017). Alginate/Gelatin scaffolds incorporated with Silibinin-loaded Chitosan nanoparticles for bone formation in vitro. *Colloids and Surfaces B: Biointerfaces*, *158*, 308–318. doi: 10.1016/j.colsurfb.2017.06.048

Li, X., Xiong, F., Wang, S., Zhang, Z., Dai, J., Chen, H., Wang, J., Wang, Q., & Yuan, H. (2021). N-Acetyl-Cysteine-Loaded Biomimetic Nanofibrous Scaffold for Osteogenesis of Induced-Pluripotent-Stem-Cell-Derived Mesenchymal Stem Cells and Bone Regeneration. *Frontiers in Bioengineering and Biotechnology*, *9*, 1–11. doi: 10.3389/fbioe.2021.767641

Li, Y., Liu, C., Liu, W., Cheng, X., Zhang, A., Zhang, S., Liu, C., Li, N., & Jian, X. (2021). Apatite Formation Induced by Chitosan/Gelatin Hydrogel Coating Anchored on Poly(aryl ether nitrile ketone) Substrates to Promote Osteoblastic Differentiation. *Macromolecular Bioscience*, *21*(11), e2100262, 1-10. doi: 10.1002/mabi.202100262

Lien, S. M., Ko, L. Y., & Huang, T. J. (2009). Effect of pore size on ECM secretion and cell growth in gelatin scaffold for articular cartilage tissue engineering. *Acta Biomaterialia*, *5*(2), 670–679. doi: 10.1016/j.actbio.2008.09.020

Lin, C. H., Lin, K. F., Mar, K., Lee, S. Y., & Lin, Y. M. (2016). Antioxidant N-Acetylcysteine and Glutathione Increase the Viability and Proliferation of MG63 Cells Encapsulated in the Gelatin Methacrylate/VA-086/Blue Light Hydrogel System. *Tissue Engineering - Part C: Methods*, *22*(8), 792–800. doi: 10.1089/ten.tec.2016.0025

Lin, X., Patil, S., Gao, Y. G., & Qian, A. (2020). The Bone Extracellular Matrix in Bone Formation and Regeneration. *Frontiers in Pharmacology*, *11*(May), 1–15. doi: 10.3389/fphar.2020.00757

Liu, B., Wu, J., Sun, X., Meng, Q., & Zhang, J. (2023). Sustained delivery of osteogenic growth peptide through injectable photoinitiated composite hydrogel for osteogenesis. *Frontiers in Bioengineering and Biotechnology*, *11*(August), 1–12. doi: 10.3389/fbioe.2023.1228250

Liu, M., Zeng, X., Ma, C., Yi, H., Ali, Z., Mou, X., Li, S., Deng, Y., & He, N. (2017). Injectable hydrogels for cartilage and bone tissue engineering. *Bone Research*, *5*(17014), 1–20. doi: 10.1038/boneres.2017.14

Liu, X., Hou, Y., Yang, M., Xin, X., Deng, Y., Fu, R., Xiang, X., Cao, N., Liu, X., Yu, W., Yang, B., & Zhou, Y. (2023). N-Acetyl-l-cysteine-Derived Carbonized Polymer Dots with ROS Scavenging via Keap1-Nrf2 Pathway Regulate Alveolar Bone Homeostasis in Periodontitis. *Advanced Healthcare Materials*, 12(2300890), 1-15. doi: 10.1002/adhm.202300890

Liu, X., Sun, S., Wang, N., Kang, R., Xie, L., & Liu, X. (2022). Therapeutic application of hydrogels for bone-related diseases. *Frontiers in Bioengineering and Biotechnology*, *10*(September), 1–20. doi: 10.3389/fbioe.2022.998988

Luo, X., Liu, Y., Pang, J., Bi, S., Zhou, Z., Lu, Z., Feng, C., Chen, X., & Kong, M. (2020). Thermo/photo dual-crosslinking chitosan-gelatin methacrylate hydrogel with controlled shrinking property for contraction fabrication. *Carbohydrate Polymers*, *236*(116067), 1-10. doi: 10.1016/j.carbpol.2020.116067

Mandal, A., Clegg, J. R., Anselmo, A. C., & Mitragotri, S. (2020). Hydrogels in the clinic. *Bioengineering and Translational Medicine*, *5*(2), 1–12. doi: 10.1002/btm2.10158

Marsell, R. and Einhorn, T. A. (2011). The biology of fracture healing. *Injury*, *42*(6), pp. 551–555. doi: 10.1016/j.injury.2011.03.031

Martínez, A., Zudaire, E., Portal-Núñez, S., Guédez, L., Libutti, S. K., Stetler-Stevenson, W. G., & Cuttitta, F. (2004). Proadrenomedullin NH2-terminal 20 peptide is a potent angiogenic factor, and its inhibition results in reduction of tumor growth. *Cancer Research*, *64*(18), 6489–6494. doi: 10.1158/0008-5472.CAN-04-0103

Martínez-Herrero, S., Larrayoz, I. M., Ochoa-Callejero, L., Fernández, L. J., Allueva, A., Ochoa, I., & Martínez, A. (2016). Prevention of bone loss in a model of postmenopausal osteoporosis through adrenomedullin inhibition. *Frontiers in Physiology*, *7*(280), 1-11. doi: 10.3389/fphys.2016.00280

Mathew, A. P., Uthaman, S., Cho, K. H., Cho, C. S., & Park, I. K. (2018). Injectable hydrogels for delivering biotherapeutic molecules. *International Journal of Biological Macromolecules*, *110*, 17–29. doi: 10.1016/j.ijbiomac.2017.11.113

Meng, Z., Liu, J., Feng, Z., Guo, S., Wang, M., Wang, Z., Li, Z., Li, H., & Sui, L. (2022). N-acetylcysteine regulates dental follicle stem cell osteogenesis and alveolar bone repair via ROS scavenging. *Stem Cell Research and Therapy*, *13*(466), 1-13. doi: 10.1186/s13287-022-03161-y

Mndlovu, H., Kumar, P., du Toit, L. C., & Choonara, Y. E. (2024). A review of biomaterial degradation assessment approaches employed in the biomedical field. *Npj Materials Degradation*, *8*(66), 1-19. doi: 10.1038/s41529-024-00487-1

Mountziaris, P. M. & Mikos, A. G. (2008). Modulation of the inflammatory response for enhanced bone tissue regeneration. *Tissue Engineering - Part B: Reviews*, *14*(2), 179–186. doi: 10.1089/ten.teb.2008.0038

Naot, D., Callon, K. E., Grey, A., Cooper, G. J. S., Reid, I. R., & Cornish, J. (2001). A potential role for adrenomedullin as a local regulator of bone growth. *Endocrinology*, *142*(5), 1849–1857. doi: 10.1210/endo.142.5.8152

Naot, D., Musson, D. S., & Cornish, J. (2019). The activity of peptides of the calcitonin family in bone. *Physiological Reviews*, *99*(1), 781–805. doi: 10.1152/physrev.00066.2017

Ning, Z., Tan, B., Chen, B., Lau, D. S. A., Wong, T. M., Sun, T., Peng, S., Li, Z., & Lu, W. W. (2019). Precisely Controlled Delivery of Abaloparatide through Injectable Hydrogel to Promote Bone Regeneration. *Macromolecular Bioscience*, *19*(6), 1–9. doi: 10.1002/mabi.201900020

Osi, A. R., Zhang, H., Chen, J., Zhou, Y., Wang, R., Fu, J., Müller-Buschbaum, P., & Zhong, Q. (2021). Three-Dimensional-Printable Thermo/Photo-Cross-Linked Methacrylated Chitosan-Gelatin Hydrogel Composites for Tissue Engineering. *ACS Applied Materials and Interfaces*, *13*(19), 22902–22913. doi: 10.1021/acsami.1c01321

Priya, M. V., Sivshanmugam, A., Boccaccini, A. R., Goudouri, O. M., Sun, W., Hwang, N., Deepthi, S., Nair, S. V., & Jayakumar, R. (2016). Injectable osteogenic and angiogenic nanocomposite hydrogels for irregular bone defects. *Biomedical Materials*, *11*(035017), 1-16. doi:10.1088/1748-6041/11/3/035017

Riester, O., Borgolte, M., Csuk, R., & Deigner, H.-P. (2021). Challenges in Bone Tissue Regeneration: Stem Cell Therapy, Biofunctionality and Antimicrobial Properties of Novel Materials and Its Evolution. *Internationa Journal of Molecular Sciences*, *22*(192), 1-25. doi:10.3390/ijms22010192

Ruggieri, I. N. C., Cícero, A. M., Issa, P. J. M., & Feldman, S. (2021). Bone fracture healing: perspectives according to molecular basis. *Journal of Bone and Mineral Metabolism*, *39*, 311–331. doi: 10.1007/s00774-020-01168-0

Saraiva, S. M., Miguel, S. P., Ribeiro, M. P., Coutinho, P., & Correia, I. J. (2015). Synthesis and characterization of a photocrosslinkable chitosan-gelatin hydrogel aimed for tissue regeneration. *RSC Advances*, *5*(78), 63478–63488. doi: 10.1039/c5ra10638a

Saul, D. & Khosla, S. (2022). Fracture Healing in the Setting of Endocrine Diseases, Aging, and Cellular Senescence. *Endocrine Reviews*, *43*(6), 984–1002. doi: 10.1210/endrev/bnac008

Shayesteh Moghaddam, N., Taheri Andani, M., Amerinatanzi, A., Haberland, C., Huff, S., Miller, M., Elahinia, M., & Dean, D. (2016). Metals for bone implants: safety, design, and efficacy. *Biomanufacturing Reviews*. Springer International Publishing, *1*(1), 1–16. doi: 10.1007/s40898-016-0001-2

Sheppard, A. J., Barfield, A. M., Barton, S., & Dong, Y. (2022). Understanding Reactive Oxygen Species in Bone Regeneration: A Glance at Potential Therapeutics and Bioengineering Applications. *Frontiers in Bioengineering and Biotechnology*, *10*(February), 1–19. doi: 10.3389/fbioe.2022.836764

Shi, H., Zhou, K., Wang, M., Wang, N., Song, Y., Xiong, W., Guo, S., Yi, Z., Wang, Q., & Yang, S. (2023). Integrating physicomechanical and biological strategies for BTE: Biomaterials-induced osteogenic differentiation of MSCs. *Theranostics*, *13*(10), 3245–3275. doi: 10.7150/thno.84759

Shirahama, H., Lee, B. H., Tan, L. P., & Cho, N. J. (2016). Precise tuning of facile one-pot gelatin methacryloyl (GelMA) synthesis. *Scientific Reports*, *6*(31036), 1-11. doi: 10.1038/srep31036

Sordi, M. B., Cruz, A., Fredel, M. C., Magini, R., & Sharpe, P. T. (2021). Three-dimensional bioactive hydrogel-based scaffolds for bone regeneration in implant dentistry. *Materials Science and Engineering C*, *124*(112055), 1-16. doi: 10.1016/J.MSEC.2021.112055

Sun, H., Xu, J., Wang, Y., Shen, S., Xu, X., Zhang, L., & Jiang, Q. (2023). Bone microenvironment regulative hydrogels with ROS scavenging and prolonged oxygen-generating for enhancing bone repair. *Bioactive Materials*, *24*(December), 477–496. doi: 10.1016/j.bioactmat.2022.12.021

Tao, H., Ge, G., Liang, X., Zhang, W., Sun, H., Li, M., & Geng, D. (2020). Review ROS signaling cascades : dual regulations for osteoclast and osteoblast. *Acta Biochimica et Biophysica Sinica***,** 52(10), 1-8. doi: 10.1093/abbs/gmaa098

Tu, Y., Chen, N., Li, C., Liu, H., Zhu, R., Chen, S., Xiao, Q., Liu, J., Ramakrishna, S., & He, L. (2019). Advances in injectable self-healing biomedical hydrogels. *Acta Biomaterialia*, *90*, 1–20. doi: 10.1016/j.actbio.2019.03.057

Vert, M. (2009). Degradable and bioresorbable polymers in surgery and in pharmacology: Beliefs and facts. *Journal of Materials Science: Materials in Medicine*, *20*(2), 437–446. doi: 10.1007/s10856-008-3581-4

Vidović, B. B., Milašinović, N. Z., Kotur-Stevuljević, J. M., Dilber, S. P., Kalagasidis Krušić, M. T., Đorđević, B. I., & Knežević-Jugović, Z. D. (2016). Encapsulation of α-lipoic acid into chitosan and alginate/gelatin hydrogel microparticles and its in vitro antioxidant activity. *Hemijska Industrija*, *70*(1), 49–58. doi: 10.2298/HEMIND141119010V

Wang, F., Wang, W., Kong, L., Shi, L., Wang, M., Chai, Y., Xu, J., & Kang, Q. (2021). Accelerated Bone Regeneration by Adrenomedullin 2 Through Improving the Coupling of Osteogenesis and Angiogenesis via β-Catenin Signaling. *Frontiers in Cell and Developmental Biology*, *9*(649277), 1-16. doi: 10.3389/fcell.2021.649277

Wang, W. & Yeung, K. W. K. (2017). Bone grafts and biomaterials substitutes for bone defect repair: A review. *Bioactive Materials*, *2*(4), 224–247. doi: 10.1016/j.bioactmat.2017.05.007

Wang, Y., Cao, X., Ma, M., Lu, W., Zhang, B., & Guo, Y. 2020. A GelMA-PEGDA-nHA composite hydrogel for bone tissue engineering. *Materials*, *13*(17), 1–12. doi: 10.3390/MA13173735

Wu, A.-M., Bisignano, C., James, S. L., Abady, G. G., Abedi, A., Abu-Gharbieh, E., Alhassan, R. K., Alipour, V., Arabloo, J., Asaad, M., Asmare, W. N., Awedew, A. F., Banach, M., Banerjee, S. K., Riera, L. S., Schwebel, D. C., Shahabi, S., Shaikh, M. A., Soheili, A., Tabarés-Seisdedos, R., Tovani-Palone, M. R., Tran, B. X., Travillian, R. S., Valdez, P. R., Vasankari, T. J., Velazquez, D. Z., Venketasubramanian, N., Vu, G. T., Zhang, Z.-J., & Vos, T. (2021). Global, regional, and national burden of bone fractures in 204 countries and territories, 1990-2019: a systematic analysis from the Global Burden of Disease Study 2019. *Lancet Healthy Longevity*, *2*, e580-e592. doi: 10.1016/ S2666-7568(21)00172-0

Wu, X., Wang, L. U., Deng, F., & Watts, D. C. (2014). Mouse Calvarial Defect Model: An Approach for the Micro-Tomographic Evaluation of Polymer Scaffolds. *Microscopy Research and Technique*, *1043*(September), 1037–1043. doi: 10.1002/jemt.22433

Xu, K., Yao, H., Fan, D., Zhou, L., & Wei, S. (2021). Hyaluronic acid thiol modified injectable hydrogel: Synthesis, characterization, drug release, cellular drug uptake and anticancer activity. *Carbohydrate Polymers*, *254*(117286), 1-8. doi: 10.1016/j.carbpol.2020.117286

Xue, B., Xu, Z., Li, L., Guo, K., Mi, J., Wu, H., Li, Y., Xie, C., Jin, J., Xu, J., Jiang, C., Gu, X., Qin, M., Jiang, Q., Cao, Y., & Wang, W. (2025). Hydrogels with programmed spatiotemporal mechanical cues for stem cell-assisted bone regeneration. *Nature Communications*, *16*(3633), 1-18. doi: 10.1038/s41467-025-59016-6

Yahyouche, A., Zhidao, X., Czernuszka, J. T., & Clover, A. J. P. (2011). Macrophage-mediated degradation of crosslinked collagen scaffolds. *Acta Biomaterialia*, *7*(1), 278–286. doi: 10.1016/J.ACTBIO.2010.08.005

Yamamoto, M., Ikada, Y., & Tabata, Y. (2001). Controlled release of growth factors based on biodegradation of gelatin hydrogel. *Journal of Biomaterials Science, Polymer Edition 12*(1), 77-88. doi: 10.1163/156856201744461

Yan, X., An, N., Zhang, Z., Qiu, Q., Yang, D., Wei, P., Zhang, X., Qiu, L., & Guo, J. (2024). Graphene Oxide Quantum Dots-Preactivated Dental Pulp Stem Cells/GelMA Facilitates. International Journal of *Nanomedicine*, *19*, 10107–10128. doi: 10.2147/IJN.S480979

Yue, K., Santiago, G. T., Tamayol, A., Annabi, N., Khademhosseini, A., Hospital, W., Arabia, S., Trujillo-de Santiago, G., Alvarez, M. M., Tamayol, A., Annabi, N., & Khademhosseini, A. (2016). Synthesis, properties, and biomedical applications of gelatin methacryloyl (GelMA) hydrogels. *Biomaterials*, *73*(3), 254–271. doi: 10.1016/j.biomaterials.2015.08.045.Synthesis

Zanon, M., Chiappone, A., Garino, N., Canta, M., Frascella, F., Hakkarainen, M., Pirri, C. F., & Sangermano, M. (2022). Microwave-assisted methacrylation of chitosan for 3D printable hydrogels in tissue engineering. *Materials Advances*, *3*(1), 514–525. doi: 10.1039/D1MA00765C

Zeugolis, D. I., Marie Saunders, M., Tatullo, M., Srl, T., Hajime Sasaki, I., Shi, Q., Goodman, S. B., Pajarinen, J., Yao, Z., & Lin, T. (2019). Inflammation and Bone Repair: From Particle Disease to Tissue Regeneration. *Frontiers in Bioengineering and Biotechnology*, 7(230), 1-11. doi: 10.3389/fbioe.2019.00230

Zhao, L., Zhou, Y., Zhang, J., Liang, H., Chen, X., & Tan, H. (2023). Natural Polymer-Based Hydrogels: From Polymer to Biomedical Applications. *Pharmaceutics*, *15*(2514), 1-30. doi: 10.3390/ pharmaceutics15102514

Zhao, Y., Zhang, Q., Zhang, S., Chen, J., Kong, L., Gao, J., & Zhu, Q. (2025). Adrenomedullin-loaded Gelatin Methacryloyl Hydrogel Promotes Endogenous Dental Pulp Regeneration: An In Vitro and In Vivo Study. *Journal of Endodontics*, *51*(2), 172–184. doi: 10.1016/j.joen.2024.11.011

Zheng, H., Liu, J., Sun, L., & Meng, Z. (2024). The role of N-acetylcysteine in osteogenic microenvironment for bone tissue engineering. *Frontiers in Cell and Developmental Biology*, *12*(July), 1–17. doi: 10.3389/fcell.2024.1435125

Appendix A – Determination of NAC Loading Conditions

A.1 Antioxidant Activity of NAC and ALA

The antioxidant activity of the compounds was evaluated using the DPPH colorimetric assay, which measures the ability of molecules to neutralize the DPPH radical . When comparing soluble N-acetylcysteine (NAC) to α-lipoic acid (ALA) in two formulations (emulsified and ethanol-dissolved), only NAC showed detectable antioxidant activity within the tested concentration range (Figure A1).

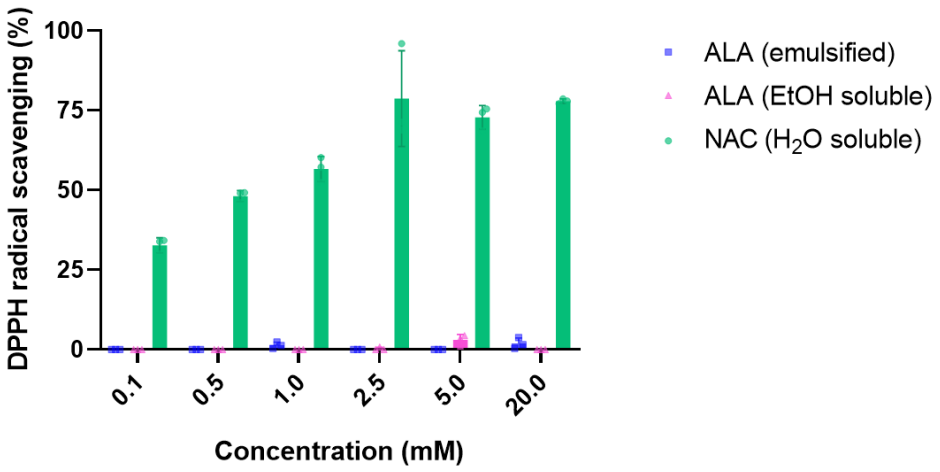

Figure 27. Antioxidant activity of ALA and NAC evaluated using the DPPH method. The percentage of antioxidant activity of α-lipoic acid (ALA) in both its emulsified and ethanol-dissolved forms, and soluble NAC, was assessed at concentrations ranging from 0.1 to 20 mM using the DPPH radical scavenging assay. NAC demonstrated significantly higher antioxidant activity at all concentrations tested, reaching up to 75% inhibition. In contrast, ALA showed very limited activity in both formulations, remaining below 10% in all cases, which would hinder its detection in release studies.

A.2 Cytocompatibility of NAC in L929 Cells

The cytocompatibility of soluble NAC was evaluated using the MTT assay on L929 fibroblast cells after 24 hours of exposure to a range of concentrations (Figure 28). No concentration tested reduced cell viability; in fact, low concentrations of NAC (0.1 mM) resulted in a significant increase in metabolic activity compared to the untreated control (0 mM). Higher concentrations (≥5 mM) did not have a significant effect on viability. Based on these results, two concentrations—2.5 mM (low) and 20 mM (high)—were selected for incorporation into the hydrogels and subsequent release studies via antioxidant assays.

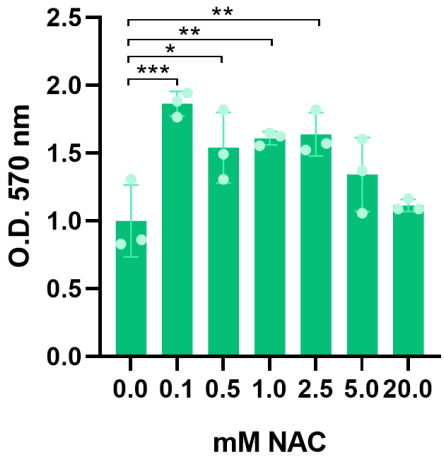

Figure 28. Viability of L929 fibroblasts exposed to soluble NAC. MTT assay results after 24 hours of treatment with soluble NAC at concentrations ranging from 0.1 to 20 mM. Cell viability was measured by absorbance at 570 nm. A significant increase in viability was observed at 0.1 mM NAC, while no cytotoxic effect was detected at higher concentrations.

Appendix B – Evaluation of Hydrogel Precursor Manipulability

Combinations of gelatin methacrylate (GelMA) and chitosan methacrylate (ChMA) were evaluated based on their manipulability, determined by the viscosity of the precursor solutions and their ability to be pipetted. Table 4 indicates with a ✓ the formulations considered to be easily handled, and with an ✗ those that were too viscous and therefore not suitable for injection or extrusion-based applications.

From this evaluation, two formulations were selected that represented the highest concentrations of each polymer within the manipulable range: GelMA at 4% combined with ChMA at 3.5% (referred to as G4C3), and GelMA at 7.5% combined with ChMA at 1% (referred to as G7C1).

Table 4. GelMA and ChMA combinations evaluated for the preparation of injectable hydrogels.

%	Chitosan MA				
Gelatin MA		1	1.5	2	3
	4	✓	✓	✓	✓
	5	✓	✓	✓	X
	7.5	✓	X	X	X

Appendix C – Antioxidant Activity of NAC-Releasing Hydrogels

Hydrogels were prepared using the selected formulations (G7C1 and G4C3), incorporating the previously defined low (2 mM) and high (20 mM) concentrations of NAC. The antioxidant activity of the released NAC was evaluated by incubating the hydrogels in 1X PBS and measuring their radical scavenging capacity using the DPPH assay (Figure 29).

After 15 minutes, the G4C3 hydrogel with 2 mM NAC reached 23.46% antioxidant activity, while G7C1 with the same concentration reached only 7.67%. For hydrogels containing 20 mM NAC, G7C1 exhibited a peak in release at 60 minutes followed by a progressive decline. In contrast, the G4C3 20 mM hydrogel demonstrated a more sustained release, maintaining relatively constant antioxidant activity throughout the evaluation period.

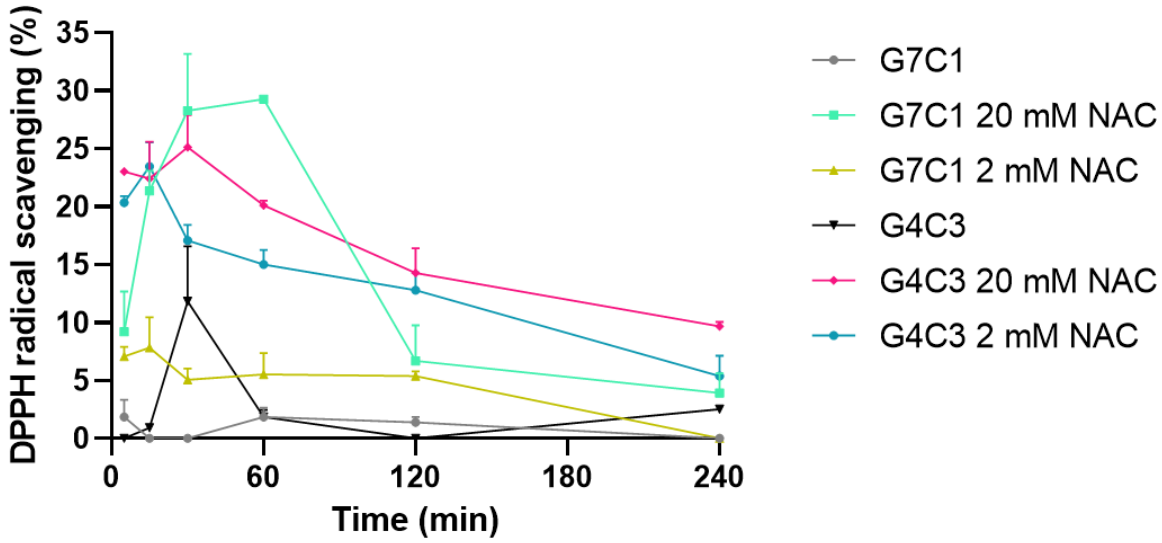

Figure 29. Antioxidant activity released from GC hydrogels with different NAC concentrations. Antioxidant release profiles were assessed using the DPPH assay for hydrogels composed of 4% or 7% gelatin methacrylate (GelMA) and 1% or 3% chitosan methacrylate (ChMA), incubated in 1X PBS at 37 °C for up to 240 minutes. Control formulations without NAC (G7C1 and G4C3) were compared to those loaded with either 2 mM or 20 mM NAC. A rapid release was observed during the first 60 minutes, especially for the G7C1 20 mM and G4C3 20 mM groups, followed by a gradual decrease in antioxidant activity. Formulations without NAC showed minimal activity throughout the test.

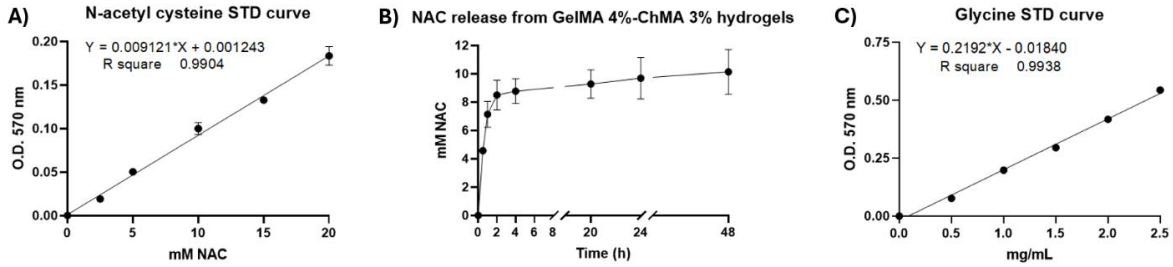

Figure 30. NAC release quantification. (A) NAC standard curve used to quantify NAC release. (B) NAC release profile from GelMA 4%–ChMA 3% hydrogels over 48 hours. (C) Glycine standard curve used to determine the cumulative release of NAC and PAMP from the hydrogels. Data are presented as mean ± standard deviation (n = 3).

Appendix D – Mechanical Characterization of NAC-Loaded Hydrogels

To compare the mechanical properties of the G7C1 and G4C3 formulations loaded with 20 mM NAC, uniaxial compression tests were performed. Stress–strain curves were obtained (Figure 31-A), from which the Young's modulus (Figure 31-B) and toughness (Figure 31-C) were calculated. The G4C3 formulation exhibited superior mechanical performance across all evaluated parameters compared to G7C1. However, due to the limited sample size (n = 2), statistical analysis was not performed.

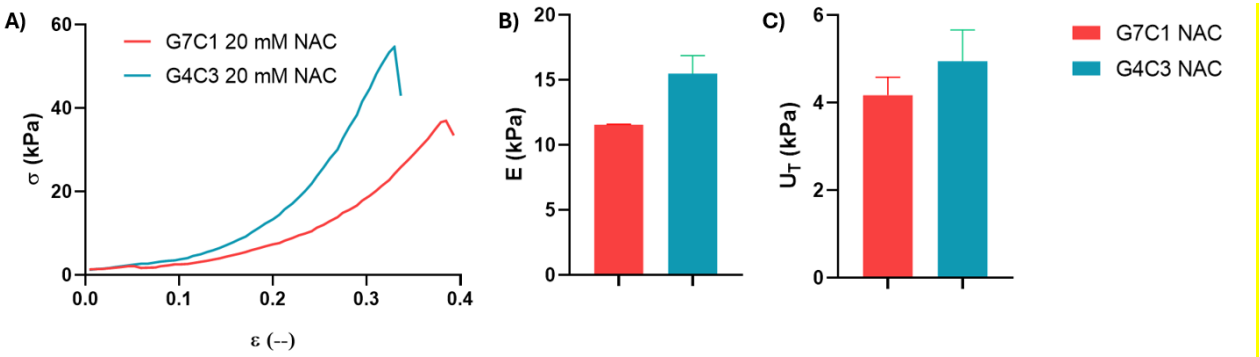

Figure 31. Mechanical characterization of GC hydrogels loaded with 20 mM NAC. (A) Stress–strain curves from uniaxial compression tests for hydrogels composed of 4% or 7% gelatin methacrylate (GelMA) and 3% or 1% chitosan methacrylate (ChMA), corresponding to G4C3 and G7C1, respectively, both loaded with 20 mM N-acetylcysteine (NAC). (B) Young's modulus (E), calculated from the linear region of the stress–strain curves. (C) Toughness (UT), determined as the area under the curve up to the point of failure. G4C3 hydrogels displayed greater mechanical strength and stiffness than G7C1, likely due to a higher crosslinking density resulting from the increased ChMA content.

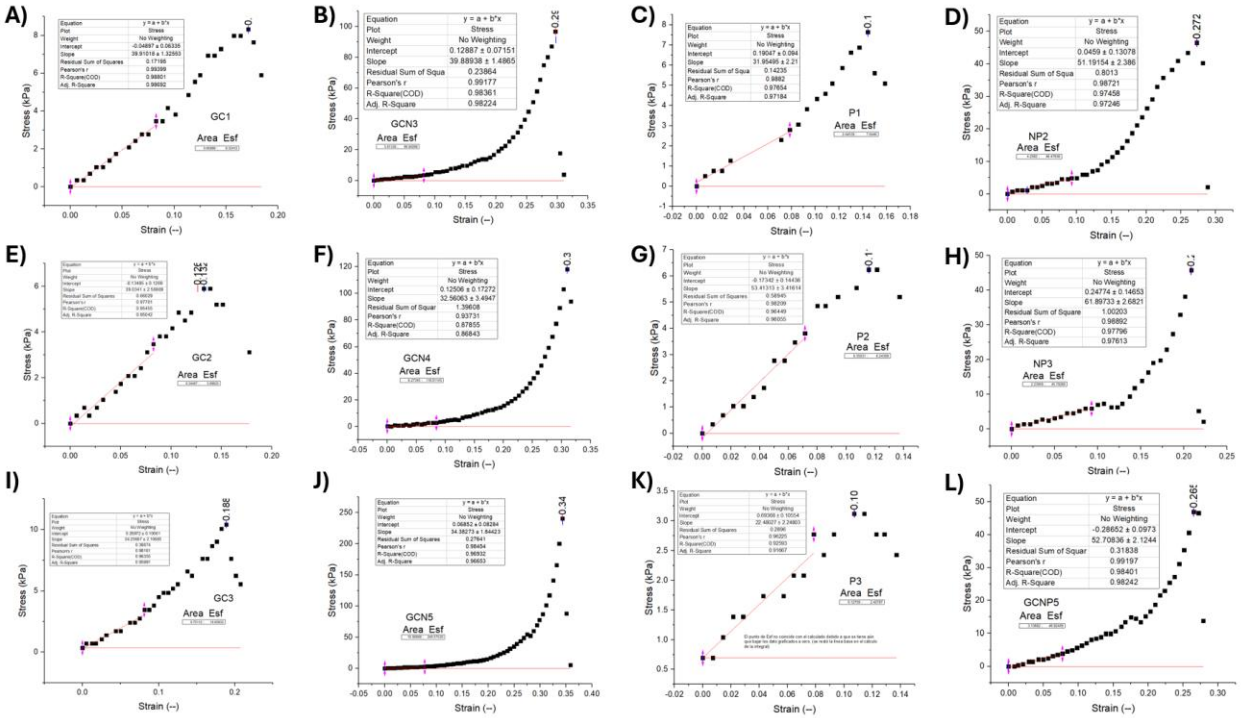

Figure 32.. Mechanical characterization of GC hydrogels. Compression stress-strain curves obtained from texture analysis (n=3). Each dataset corresponds to (A, E, I) GC, (B, F, J) GCN, (C, G, K) GCP, and (D, H, L) GCNP.

Appendix F – Hemocompatibility Assays

To assess the hemocompatibility of NAC-loaded hydrogels, two complementary assays were conducted: a hemolysis assay to evaluate red blood cell (RBC) membrane integrity, and a blood clotting assay to estimate hemostatic capacity.

Hemolytic activity was evaluated by measuring hemoglobin release from lysed erythrocytes. The test was performed following the ISO 10993-4 guidelines, where a hemolysis percentage below 5% is considered acceptable for blood-contacting biomaterials.

Blood samples were collected from healthy male volunteers via venipuncture under aseptic conditions. Each hydrogel sample was hydrated in 1 mL of phosphate-buffered saline (PBS 1X) at 37 °C for 30 minutes (Figure 33). Subsequently, 40 µL of fresh blood was added to the PBS-hydrogel mixture, gently mixed by inversion, and incubated at 37 °C for 1 hour. PBS 1X and distilled water served as negative and positive controls, respectively. After incubation, samples were centrifuged at 700 g for 10 minutes, and 200 µL of the supernatant was transferred to a 96-well plate for absorbance measurement at 540 nm (Epoch, BioTek Instruments) to quantify hemoglobin release (Ooi et al., 2019).

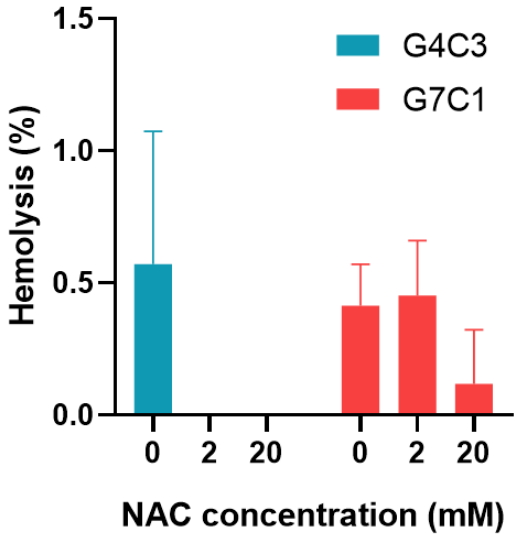

Figure 33. Hemolysis percentages of G4C3 and G7C1 hydrogels at 0, 2, and 20 mM NAC concentrations. All values are below 5%, demonstrating hemocompatibility (n=3).

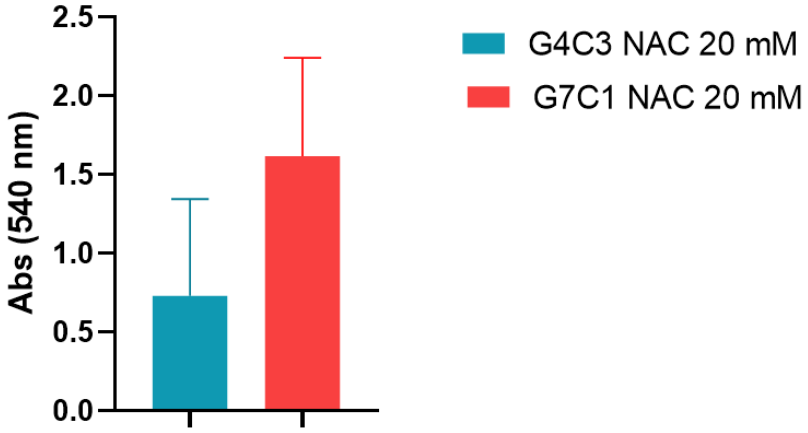

Figure 34. Blood clotting assay of G4C3 and G7C1 hydrogels. Lower absorbance indicates higher clotting efficiency (n=3).

The hemostatic activity of the hydrogels was evaluated by measuring the amount of free (unclotted) red blood cells, which lyse and release hemoglobin in the presence of water (Figure 34). A lower absorbance value correlates with greater hemostatic efficiency.

Briefly, 100 µL of anticoagulated whole blood was infiltrated through each hydrogel sample. Clotting was initiated by adding 10 µL of 0.02 M $CaCl_2$ and incubating at 37 °C for 15 minutes. After incubation, 2 mL of distilled water was added to each sample and left for 5 minutes at room temperature. The red blood cells not incorporated into clots were lysed, releasing hemoglobin. The mixtures were centrifuged at 300 g for 10 minutes, and 200 µL of the supernatant was transferred to a 96-well plate. Absorbance was read at 540 nm (Epoch, BioTek). The absorbance values were inversely proportional to the clotting efficiency of each hydrogel formulation.

Appendix G – Viability of NAC-loaded hydrogels

To assess the cytocompatibility of NAC-loaded GC hydrogels (G4C3 and G7C1) in RAW 264.7 macrophage-derived osteoclast precursors using metabolic and membrane integrity assays.

Hydrogel formulations maintained cell viability above 95% after 24 hours of indirect exposure, as shown by MTT assay (Figure 35). Additionally, fluorescence-based live/dead staining confirmed high cell viability with strong calcein-AM (live cell) signal and minimal ethidium homodimer (dead cell) staining in both formulations, comparable to the monolayer control (Figure 36). These results demonstrate that NAC-loaded hydrogels do not exert cytotoxic effects on osteoclast precursors.

RAW 264.7 cells were seeded on the bottom of 24-well plates and cultured in the presence of hydrogels placed in transwells for 24 h. MTT assay was used to determine mitochondrial activity, and viability was expressed as a percentage relative to the monolayer control. For live/dead staining, cells were incubated with calcein-AM and ethidium homodimer-1 following manufacturer instructions, and fluorescence was observed using an inverted fluorescence microscope.

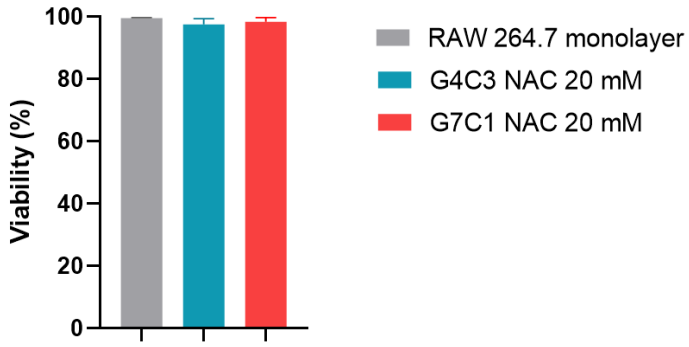

Figure 35. Cell viability of RAW 264.7 cells after 24 h exposure to GC hydrogels loaded with 20 mM NAC (G4C3 and G7C1) assessed by Live/dead assay. Data are shown as mean ± SD, normalized to monolayer control.

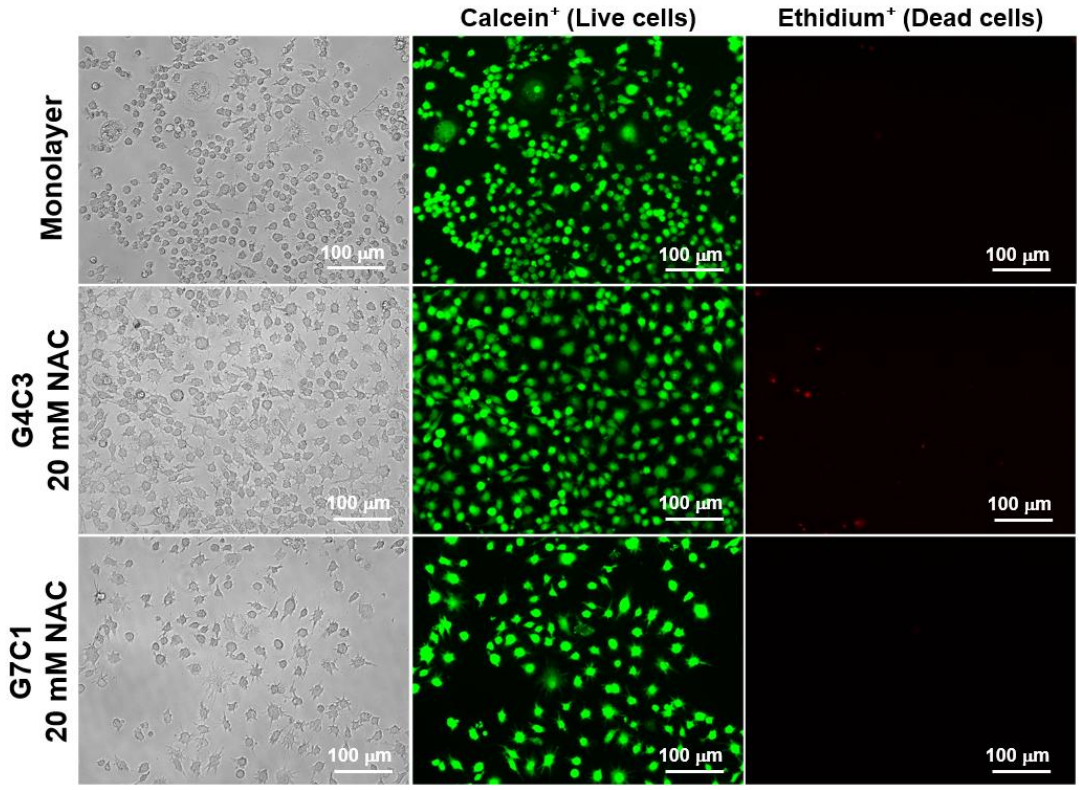

Figure 36. Live/dead assay of RAW 264.7 cells exposed to GC hydrogels loaded with 20 mM NAC (G4C3 and G7C1). Images show phase contrast (left), calcein-AM (middle), and ethidium homodimer-1 (right) fluorescence. Scale bar = 100 µm.

Appendix G – Viability of NAC and PAMP-loaded hydrogels in HMEC cells and aorta rings

To evaluate the viability of endothelial cells (HMEC) and the tissue compatibility of hydrogels in a vascularized *ex vivo* model, aortic rings were cultured within hydrogels for 11 days and stained with calcein-AM to assess cell viability and sprouting.

To simulate an indirect exposure environment, hydrogels were placed on Transwell inserts and cultured with HMEC monolayers for 24 and 48 h. Cell viability was assessed via MTT assay.

At 24 h, GCN exhibited the highest viability among hydrogel-treated groups, showing comparable values to the monolayer control. GCNP and GCP treatments resulted in moderate viability (~75–80%), while GC showed a slight but statistically significant decrease (**$p < 0.05$**). After 48 h, GCN maintained high viability (>90%), whereas GC, GCP, and GCNP showed reduced values, with GCNP presenting the lowest viability (~73%). These results suggest that GCN may offer a more cytocompatible environment in early time points, while GCNP may induce a delayed stress response. However, all values remained above the viability threshold, confirming general compatibility (Figure 37).

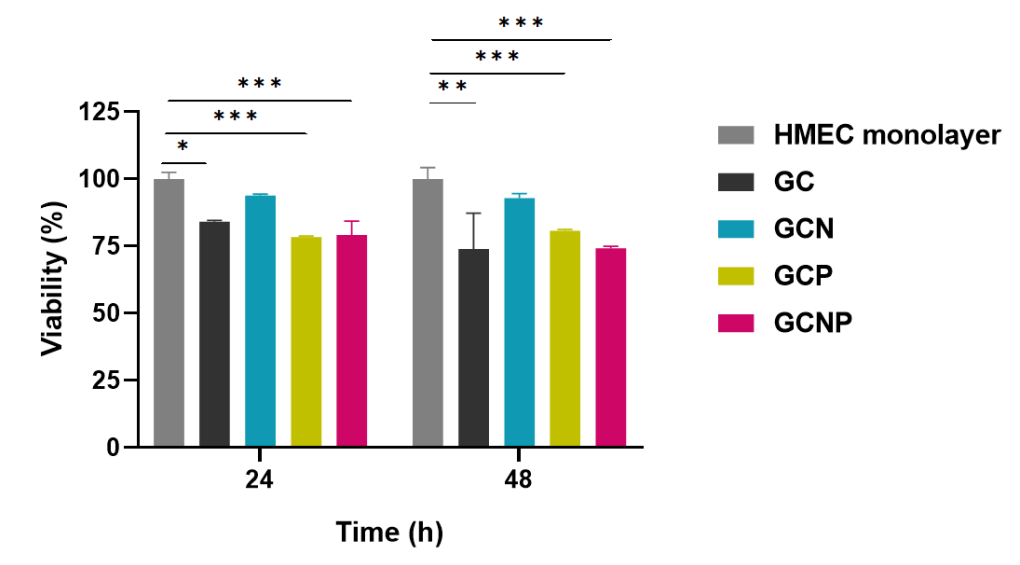

Figure 37. Viability of HMEC cultured for 24 and 48 h in the presence of hydrogel formulations placed in Transwell inserts. Viability was measured by MTT assay and normalized to the untreated monolayer control. Data are presented as mean ± SD (n=3). Asterisks indicate statistical significance between groups (*p<0.05, **p<0.01, ***p<0.001).*

Aortic rings from adult mice were embedded within the hydrogels and cultured for 11 days to evaluate viability and tissue interaction (Figure 38). Samples were stained with calcein-AM and imaged under fluorescence and bright-field microscopy. Bright-field and fluorescent images of aortic rings embedded in hydrogels revealed differences in tissue interaction and viability. All hydrogel groups allowed ring encapsulation, but qualitative differences were observed in sprouting and fluorescent intensity. GC and GCN samples showed viable green fluorescence along the edge of the tissue, although the density and distribution were limited. GCP samples exhibited localized sprouting with intense calcein staining, suggesting focal cell activity. GCNP hydrogels supported broad and diffuse green fluorescence across the surrounding matrix, indicating widespread cell viability and possible migration or integration into the hydrogel.

These findings suggest that GCNP hydrogels may provide a more favorable microenvironment for vascular tissue interaction, likely due to the combined effects of NAC and PAMP. However, aortic sprouting was not quantitatively analyzed in this study.

While fluorescence confirms cell viability, functional assessments such as endothelial tube formation, angiogenic marker expression, or perfusion capacity were not performed. Future work should incorporate quantitative metrics and molecular analyses to better define the angiogenic potential of these hydrogels.

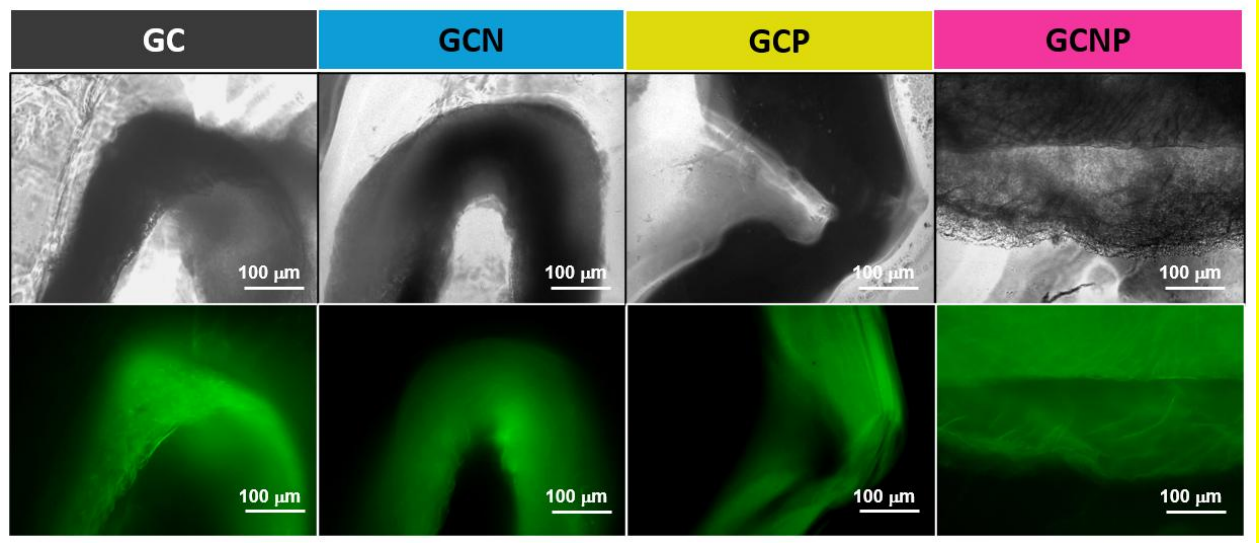

Figure 38. Viability of aortic rings cultured within hydrogel matrices after 11 days. Bright-field (top row) and calcein-AM fluorescence (bottom row) images show the interaction between the aortic tissue and the hydrogel. GCNP hydrogels exhibited more diffuse green fluorescence, suggesting enhanced viability and potential tissue integration compared to other groups. Scale bars: 100 µm.